5-2017

Changes in Floodplain Inundation under Non-Stationary Hydrology for an Adjustable, Alluvial River Channel

Bruce C. Call
Utah State University

CHANGES IN FLOODPLAIN INUNDATION UNDER NON-STATIONARY

HYDROLOGY FOR AN ADJUSTABLE, ALLUVIAL RIVER CHANNEL

by

Bruce C. Call

A thesis submitted in partial fulfillment
of the requirements for the degree

of

MASTER OF SCIENCE

in

Watershed Science

Approved:

_____   _____
Patrick Belmont, Ph.D.   Philip Bailey, Ph.D.
Major Professor   Committee Member

_____   _____
John Schmidt, Ph.D.   Peter Wilcock, Ph.D.
Committee Member   Committee Member

_____
Mark McLellan, Ph.D.
Vice President for Research and
Dean of the School of Graduate Studies

UTAH STATE UNIVERSITY
Logan, Utah

2017

ABSTRACT

Changes in Floodplain Inundation under Non-Stationary Hydrology

for an Adjustable, Alluvial River Channel

by

Bruce C. Call, Master of Science

Utah State University, 2017

Major Professor: Dr. Patrick Belmont
Department: Watershed Science

Predicting the frequency and aerial extent of flooding in river valleys is essential

for infrastructure design, environmental management, and risk assessment. Conventional

flood prediction relies on assumptions of stationary flow distributions and static channel

geometries. However, nonstationary flow regimes are increasingly observed and changes

in flow or sediment supply are known to alter the geometry of alluvial channels.

Therefore, systematic changes in flow regimes and channel geometry may amplify or

attenuate the frequency and magnitude of flood inundation in unexpected ways. We

present a stochastic, reduced complexity model to investigate such dynamics. The model

routes an annual peak discharge series through a simplified reach-average channel-

floodplain cross-section. Channel width, depth and slope are allowed to adjust based on

the discharge and sediment supply from the most recent flood. Model predictions are

compared to empirical observations in two rivers that have experienced multiple large

floods over the past six years. The model is then run using six hypothetical flow scenarios

and five sediment supply scenarios. Results demonstrate that systematic shifts in peak

flows cannot be translated directly to changes in the frequency or extent of floodplain

inundation. Rather, the frequency of floodplain inundation is primarily dependent on the

relative rate and trajectory of channel adjustment towards an equilibrium geometry

dictated by the mean and standard deviation of peak flows. Model results further suggest

that the most significant control on the mean horizontal width of floodplain inundation is

the flood distribution's coefficient of variation.

(152 pages)

PUBLIC ABSTRACT

Changes in Floodplain Inundation under Non-Stationary Hydrology

for an Adjustable, Alluvial River Channel

Bruce C. Call

Predicting the frequency and aerial extent of flooding in river valleys is essential for infrastructure design, environmental management, and risk assessment. Such flooding occurs when the discharge of water within a river channel exceeds its maximum capacity and the extra water submerges the adjoining floodplain surface. The maximum capacity of a channel is controlled by its geometry, gradient, and frictional resistance. Conventional flood prediction methods rely on assumptions of unchanging flood probabilities and channel capacities. However, changes in climate, land cover, and water management have been shown to systematically shift the magnitude and variability of flood flows in many systems. Additionally, alluvial river channels continually adjust their geometries according to characteristics of flow and sediment regimes. For example, channels can expand their geometry during high-energy flows through erosion, then contract their geometry through sediment deposition during low-energy flows. This means that changes in flow magnitudes, frequencies, or durations can cause changes in a channel's maximum capacity due to adjustments in river channel geometry. Therefore, future changes in river flow regimes and channel geometry may amplify or attenuate the frequency and magnitude of flood inundation in unexpected ways.

The focus of this thesis is the development of a novel simulation model to

investigate potential changes in the frequency and aerial extent of floodplain inundation due to systematic changes in peak flows and subsequent adjustments in channel geometry and capacity. The model was run using six hypothetical flow scenarios to explore how changes in the mean and variance of an annual peak flow series influences the frequency and magnitude of floodplain inundation. In order to qualitatively simulate the various mechanisms controlling channel adjustment across a continuum of different river environments, each scenario was run multiple times while gradually varying model parameters controlling the amount of permissible adjustment in channel geometry. Results suggest that systematic shifts in peak flows cannot be translated directly to changes in the frequency or magnitude of floodplain inundation due to the non-linear factors controlling the rate and trajectory of channel adjustment. Insights gained from these results demonstrate the need to account for potential changes in both peak flows and channel capacities in the prediction and mitigation of flood hazards.

ACKNOWLEDGMENTS

I would like to thank my advisor Dr. Patrick Belmont for his willingness to take me on as a graduate student and the excellent support and guidance he has given me. I am grateful for the help and insights of my committee members Phillip Bailey, Jack Schmidt, and Peter Wilcock. I'd also like to acknowledge the support and companionship of my family, friends, and colleagues over the past two and a half years. Finally, I couldn't have reached this point without the incredible love and support of my parents and grandparents who have continually encouraged me to follow my bliss.

I would also like to acknowledge support from the John Wesley Powell Center for Analysis and Synthesis as well as the National Science Foundation (NSF ENG 1209445).

<div align="right">Bruce C. Call</div>

CONTENTS

LIST OF TABLES

LIST OF FIGURES

CHAPTER 1

INTRODUCTION

Within the context of river systems, flood inundation occurs when a given discharge exceeds channel capacity and water submerges the adjoining floodplain surface. Floods can be critically important for the maintenance of channel-floodplain ecosystems [*Junk et al.*, 1989; *Tockner et al.*, 2000], but can also pose significant hazards to human life, infrastructure, and economic activity [*Kundzewicz et al.*, 2014]. While great effort is made to analyze flood records as a means to predict and mitigate potential threats from such events [*IACWD*, 1982], our continued ability to predict the frequency and extent of floods can be impeded by systematic changes in flow and channel conveyance.

Prediction of a river's flood inundation regime is often aided by inundation modeling using a combination of flow frequency analysis and hydraulic modeling. Traditional methods for modeling flood hydrology typically rely on an assumption of stationary hydrologic conditions, the notion that the temporal behavior of a flood regime is constrained within an unchanging envelope of variability and modeled as a probability density function (PDF) based on historic peak discharge measurements [*Milly et al.*, 2008]. Stationarity is a standard assumption in engineering and risk assessment projects such as the National Flood Insurance Program, where estimating the magnitude and extent of the 1-in-100-yr flood from discharge records stands as a critical metric for design and planning considerations [*Olsen*, 2006].

However, the predictive capabilities of such models can be compromised by systematic changes in atmospheric and surface hydrology. Over the next century, the

characteristic behavior of flow regimes may be heavily influenced by human-induced

climate change, which is expected to increase the magnitude and variability of extreme

hydrologic events [*Charlson and Shwartz*, 1992; *Cox et al.*, 2000; *Collins et al.*, 2013].

Additionally, some have suggested that the collective effects of human modifications to

water systems globally may exceed that of climate change [*Vörösmarty et al.*, 2004]. For

example, construction of dams and other flow regulation infrastructure during the past

century has disrupted the natural flow regimes for a significant number of rivers

worldwide [*Nilsson et al.*, 2005]. Human-induced land-use and/or land cover changes,

such as agriculture and urbanization, have altered flows at relatively short timescales (10^{-1} to 10^3 years) by altering unit runoff rates [*James and Leece*, 2013; *Schottler et al.*, 2014;

Foufoula-Georgiou et al., 2015]. These systematic changes can alter the magnitude and

variability of a river's flood regime, thereby rendering flood-frequency estimates based

on historic discharge measurements less reliable. Such circumstances are commonly

referred to as "non-stationary conditions" [*Milly et al.*, 2008].

In addition to potential complications stemming from non-stationary flood

hydrology, the efficacy of traditional floodplain inundation models can be further

compromised due to a commonly invoked assumption that channel capacity remains

static over the temporal length of model runs. Channel capacity in this context refers to

the maximum discharge that can be conveyed within a channel before overflowing its

banks and is ultimately determined by channel geometry (i.e., width, depth), gradient

(i.e., bed slope, energy gradient), and roughness (i.e., frictional resistance). Contrary to

this prevailing assumption, alluvial channels are inherently dynamic and continually

adjust their geometries and gradients in response to changes in flow and sediment fluxes [*Lane*, 1955; *Wolman and Gerson*, 1978; *Wolman and Miller*, 1960; *Yu and Wolman*, 1987]. Because such changes can alter channel capacity, they should also be considered in predictions of flood inundation.

Changes in flood inundation due to changes in channel capacity can be difficult to detect due to limited empirical data documenting changes in channel geometry and few empirical observations linking flow magnitudes with extent of floodplain inundation over time. However, a few studies have noted such changes. For example, the construction of upstream water storage and diversion projects on the Rio Grande River of the Southwestern United States resulted in systematic reductions in peak flows, leading to a 50% decrease in channel width by the end of the twentieth century [*Dean and Schmidt*, 2011]. This reduction in channel capacity resulted in record flood stages following Tropical Storm Lowell in 2008 at a flow with an estimated recurrence interval of 1-in-15-yr [*Dean and Schmidt*, 2013]. *Slater et al.* [2015] further suggest that such changes in inundation dynamics due to altered channel capacities may be common. This was found by developing a method to differentiate changes in flood hazard due to changes in flows versus changes in channel capacity using discharge records from selected United States Geological Survey (USGS) gaging stations and channel cross-section field measurements. Of the sites that exhibited statistically significant trends, they found that the largest changes in flood hazard were due to shifting flow frequencies (71 sites), but that changes due to altered channel capacities were three times more common (190 sites). However, it is noteworthy that their findings may have underestimated the importance of

channel change due to the fact that USGS often locates gages in locations with relatively stable channel geometries.

This thesis explores the relationship between non-stationary flood hydrology, channel adjustment, and subsequent impacts on the spatial and temporal variability of flood inundation using a stochastic, reduced complexity model developed to simulate channel geometry adjustment as a function of hypothetical non-stationary flow regimes. The central questions guiding this work are: How do changes in the magnitude and/or variability of peak flows alter the frequency and magnitude of floodplain inundation? How might adjustments in channel geometry attenuate or exacerbate these changes?

CHAPTER 2

MODEL

River channels are formed by the movement of water and sediment through drainage basins, and can be generally classified into two categories: alluvial channels and bedrock channels. Alluvial channels are defined by erodible beds and banks formed within a floodplain through the erosion and deposition of unconsolidated sediments. Bedrock channels are defined by a thin or discontinuous alluvial cover over bedrock channels, which are deformed through physical and chemical weathering processes that usually occur over much longer time scales than those of alluvial processes. While channels can be characterized by some combination of alluvial and bedrock features, we will solely consider fully alluvial channels throughout the remainder of this paper.

The last century of research in fluvial geomorphology has advanced our understanding of alluvial channel dynamics through the formulation of several generalized conceptual models describing the various mechanisms and forces by which channels self-adjust their width, depth, and slope in response to the magnitude and frequency of geomorphically effective flows, changes in sediment supply and caliber relative to sediment transport capacity, and the efficiency of riparian vegetation to stabilize channel banks and floodplains within different climatic settings [*Lane*, 1955; *Wolman and Gerson*, 1978; *Wolman and Miller*, 1960; *Yu and Wolman*, 1987]. The fundamental mechanisms of channel adjustment include widening through bank erosion, deepening via bed incision, or narrowing and vertical aggradation through sediment deposition and vegetation encroachment. The typical range of variability in channel

geometry under a stationary flow regime is often referred to as dynamic equilibrium, a state of continuous adjustment around a mean state [*Hack*, 1960; *Schumm and Lichty*, 1965]. This mean condition is often described with empirical downstream hydraulic geometry relations that show correlations between a characteristic discharge value and other parameters (e.g., grain-size, transport capacity) with the channel's width, depth, and slope [*Gleason*, 2015].

Significant changes in flows, however, can result in significant adjustments to channel geometry and behavior that are no-longer characteristic of the system's previous equilibrium state. The most common observation of such changes is that trends of increasing flow magnitudes tend to result in wider channels [*Schumm and Lichty*, 1963; *Burkham*, 1972; *Pizzuto*, 1994], while trends of decreasing flow magnitudes tend to result in overall narrower channels [*Everrit*, 1993; *Friedman et al.*, 1998; *Allred and Schmidt*, 1999]. Channel adjustments can also be induced through changes in the mass balance of sediment supplied from upstream to a given reach relative to the channel's transport capacity. Conditions in which sediment supply is proportionally larger than transport capacity (i.e., transport limited conditions) can induce channel aggradation while conditions in which transport capacity is proportionally larger than sediment supply (i.e., supply limited conditions) can induce channel degradation [*Lane*, 1955]. While non-linear changes in sediment yield can result from non-stationary hydrology [*Belmont et al.*, 2011; *Schottler et al.*, 2014], it can also be significantly altered through the upstream closure of dams and changes from both natural and anthropogenic changes to land-cover [*Schmidt and Wilcock*, 2008; *James and Leece*, 2013].

Beyond these classic observations, the frontiers of active research in fluvial geomorphology are focused on further untangling the complexity and non-linear nature of fluvial systems, often with practical prediction and forecasting applications in mind. The complexity of channel geometry stems ultimately from it being the emergence of myriad processes occurring over a continuum of spatial and temporal scales characterized by non-linear thresholds and feedback mechanisms [*Schumm*, 1973]. Further, the future trajectory of channel adjustment can be strongly influenced by initial conditions and historical contingencies. Therefore, the magnitude and trajectory of channel adjustment in response to a given flow event depends on the state of the system at a given time, which itself is the product of past geomorphic events [*Yu and Wolman*, 1987].

These complex dynamics make purely deterministic prediction of future channel adjustment beyond the current reach of our knowledge at timescales ranging from a single flood event up to a few decades, depending on the system in question. The accuracy of such predictions ultimately depends on precise measurements of initial conditions along with knowledge of all subsequent forcing and flux conditions (e.g., shear stress, sediment supply rate), high-resolution physical modeling of hydraulic and geomorphic processes, and accurate identifications of threshold values (e.g., the value of shear stress needed to initiate bank erosion or bedload transport). Furthermore, high-resolution morphodynamic models have formidable computational limitations and theoretical shortcomings extending from our incomplete knowledge of system thresholds and feedback mechanisms, the spatial and temporal scales over which they are relevant, and an understanding of how they evolve relative to the state of the system [*Kasprak*,

2015; *Lane*, 2013; *Lotsari et al.*, 2015].

A simpler and potentially more useful method to explore the implications of non-stationary hydrology for flood prediction is to take a stochastic approach by identifying a set of potential trajectories of adjustment based on a possible range of channel and flux boundary conditions. This approach can be further simplified in a meaningful way by abstracting the system into a reduced complexity model with both quantitative and qualitative features derived from empirical observations. As the aim of this work is to examine broad relationships and trends between hypothetical non-stationary flood regimes, channel adjustment, and flood inundation, we have chosen to take this latter approach. Therefore, we have chosen to model adjustments in channel geometry using a set of physically-based, quasi-universal, empirical downstream hydraulic geometry relations rather than a purely process-based morphodynamic model. This allows us to develop a simple model that remains appropriately targeted to address our particular set of questions while also remaining appropriately reasonable by resting on both empirical and physical foundations.

2.1. Quasi-Universal Hydraulic Geometry

Downstream hydraulic geometry was first discovered and described by *Leopold and Maddock* [1953] who showed that strong power law trends emerge from empirical data sets correlating an index discharge (e.g., mean annual discharge, 1-in-2-year discharge) with channel width, depth, and velocity. Subsequent research has focused on explaining the physical basis of such occurrences and the underlying parameters influencing observed variabilities within empirical data sets [*Gleason*, 2015]. Beginning

with the work of *Parker* [1978a, 1978b], a particular line of research has focused on deriving a set of physics-based relations describing the equilibrium bankfull width, depth, and slope of a channel as a function of its bankfull discharge, characteristic bed material grain-size, and other parameters (e.g., bankfull transport capacity) by combining relations for flow continuity, flow resistance, and sediment transport into a system of equations. In order to close the system, a value or relation for the Shields number at bankfull flow is derived from a dataset of bankfull channel cross-section measurements across a wide range of different river types.

Such an approach necessarily requires invoking assumptions about the underlying physical mechanisms that confine their limits of applicability to certain classes of systems. For example, *Parker et al.* [2007] presented relations describing the equilibrium geometry of single-thread gravel-bed rivers while *Wilkerson and Parker* [2011] presented similar relations describing the equilibrium geometry of single-thread sand-bed rivers. Both sets of relations calculate bankfull width, depth, and slope as functions of specified bankfull discharge and grain-size.

The hydraulic geometry relations chosen for our modeling framework (presented in section 2.2) were formulated by *Li et al.* [2015], who extended this methodology further by incorporating a novel relation for calculating bankfull Shields number as a function of dimensionless grain-size and slope derived from a dataset of 230 bankfull cross-section measurements. The authors demonstrated that closing the system of equations with this novel relation yields significantly improvements over the relations of *Wilkerson and Parker* [2011] in predicting channel geometry for coarse sand-bed rivers

(0.062 mm to 0.5 mm).

2.2. Model Structure

The model routes a synthetically generated series of annual peak-discharges through a single, geometrically simplified cross-section of channel-floodplain topography at each time-step and calculates flood stage and the horizontal width of floodplain inundation whenever channel capacity is exceeded. At the end of each time-step, channel capacity is modified by adjusting channel dimensions to reflect changes from the annual peak flow event (e.g., widening and/or deepening in response to a large overbank flood, narrowing and bed aggradation in response to a low flow year). When all flows have been routed, the frequency of floodplain inundation is calculated as the fraction of years in which peak flows exceeded channel capacity. A flow chart of the model's algorithm is presented in Figure 1, and a detailed schematic of the model's structure is available in Figure A1.
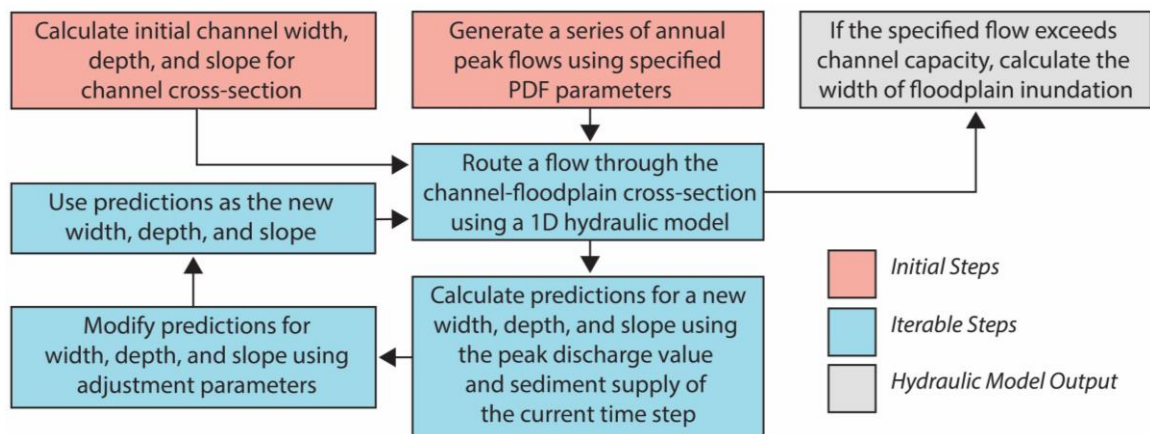
Figure 1. Flow chart of model algorithm.

The model consists of five modular components: 1) a synthetically generated series of annual peak-discharges, derived as random values from a specified probability density function, 2) a simplified cross-section representing channel-floodplain topography, 3) a one-dimensional hydraulic model to compute the stage of a given discharge for the channel-floodplain cross-section at each time-step, 4) a relation between peak discharge and a corresponding sediment supply rate, and 5), a scheme to adjust the channel's width, depth, and slope annually as a function of flow and sediment inputs.

2.2.1. Synthetic Flood Series

Values for a series of annual peak discharge, Q_p (m³/s), are randomly sampled from a Generalized Extreme Value (GEV) PDF defined by location μ, scale σ, and shape ξ parameters, which control the mean, standard deviation, and skew of the distribution, respectively [*Rao and Hamed*, 1999]:

$$f(x:\mu,\sigma,\xi) = \frac{1}{\sigma}\left[1 + \xi\left(\frac{x-\mu}{\sigma}\right)\right]^{(-1/\xi)-1} \exp\left\{-\left[1 + \xi\left(\frac{x-\mu}{\sigma}\right)\right]^{-1/\xi}\right\} \qquad (1)$$

Non-stationary conditions are simulated by systematically modifying the parameters of the GEV distribution during the model run. For example, Figure 2 shows the location parameter shifting from 250 to 400 m³/s at model year 500, while the scale and shape parameters are kept constant at 75 and 0.2. The shift is depicted visually as a change from the red to blue PDF in the top panel of Figure 2 and the shift in the annual maximum series is depicted in the bottom panel.
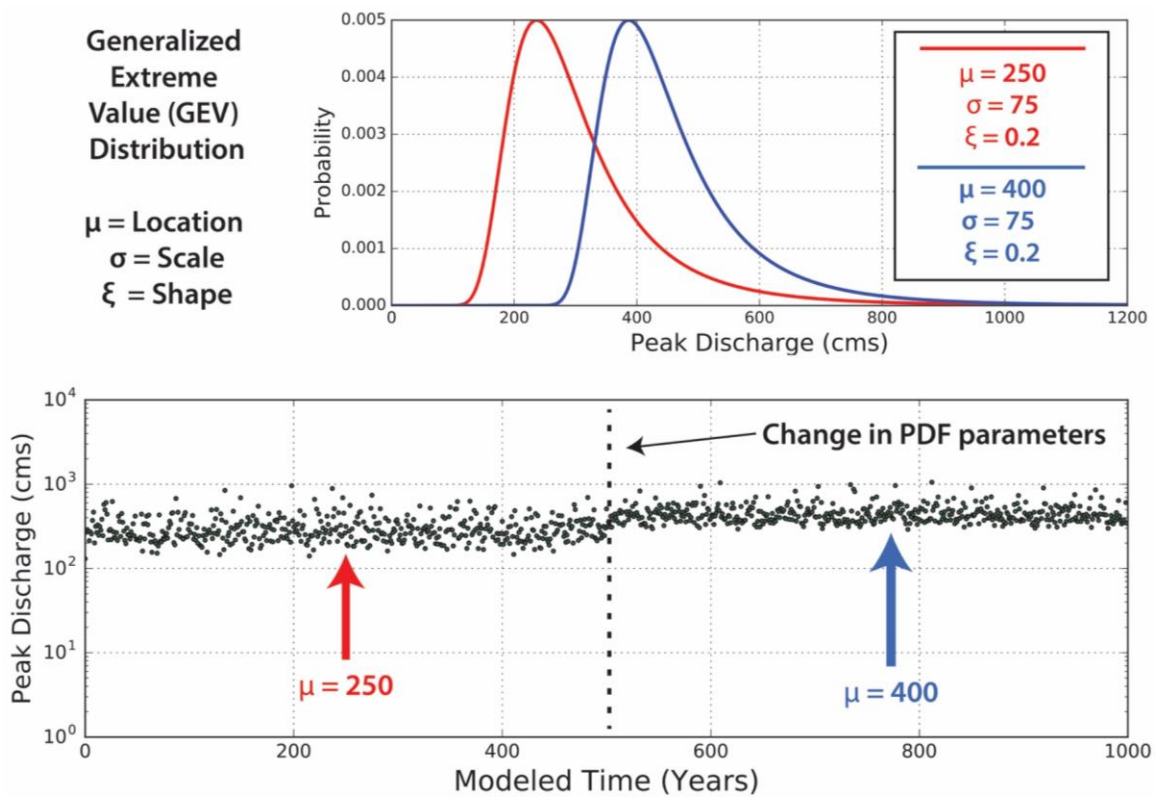
Figure 2. Example synthetic flood series derived from two stationary series (bottom), and the corresponding PDFs from which they were derived (top).

2.2.2. Channel-Floodplain Cross-Section

Reach-averaged channel-floodplain topography is modeled as a compound cross-section with geometrically simplified features (Figure 3). The channel is assumed to be rectangular and prismatic with dimensions defined by bankfull width, B_{bf} (m), depth, H_{bf} (m), and slope, S (dimensionless), which are calculated using empirically-based downstream hydraulic geometry relations proposed by *Li et al.* [2015]. These relations predict equilibrium width, depth, and slope values as a function of specified input

parameters for bankfull discharge, Q_{bf} (m³/s), bankfull sediment transport capacity,

Q_{tbf} (m³/s), and characteristic bed material grain-size, D (m; 0.062 mm and 0.5 mm):

$$\frac{B_{pred}}{D} = \frac{(D^*)^{2.5}}{\alpha_{EH}{\alpha_R}^2\sqrt{R}\beta^{2.5}\left(\frac{RD^*}{\alpha_{EH}\alpha_R\beta}\right)^{\frac{2.5m-2n_R}{1+m-n_R}}}\left(\frac{Q_{tbf}}{Q_{bf}}\right)^{\frac{2.5m-2n_R}{1+m-n_R}}\frac{Q_{tbf}}{\sqrt{g\overline{D}}D^2} \quad (2)$$

$$\frac{H_{bf}}{D} = \frac{\alpha_{EH}\alpha_R\beta^2}{(D^*)^2}\left(\frac{RD^*}{\alpha_{EH}\alpha_R\beta}\right)^{\frac{2m-n_R}{1+m-n_R}}\left(\frac{Q_{tbf}}{Q_{bf}}\right)^{\frac{2m-n_R}{1+m-n_R}}\frac{Q_{bf}}{Q_{tbf}} \quad (3)$$

$$S = \left(\frac{RD^*}{\alpha_{EH}\alpha_R\beta}\right)^{\frac{1}{1+m-n_R}}\left(\frac{Q_{tbf}}{Q_{bf}}\right)^{\frac{1}{1+m-n_R}} \quad (4)$$

where D^* is dimensionless grain-size, g is acceleration due to gravity (9.81, m^2), R is

submerged specific gravity (1.6, dimensionless), and α_{EH}, α_R, β, m, and n_R are model

parameters (0.05, 2.53, 1220, 0.53, and 0.19, respectively). The initial channel geometry,

$B_{bf,init}$, $H_{bf,init}$, and S_{init}, is calculated from input parameters for initial bankfull

discharge ($Q_{bf,init}$) and initial transport capacity ($Q_{tbf,init}$). In the version of the model

used for this paper, the characteristic bed-material grain-size (D) is held constant at 0.3

mm for the duration of model runs, consistent with observations from several rivers in

southern Minnesota that provided the initial impetus for the model.

Floodplain topography is modeled as a surface adjoined to both channel banks

that diverges upwards and away from the channel at a user-specified angle, θ. *Belmont*

[2011] demonstrated that the floodplain can be reasonably represented on a reach-average

basis as a relatively uniform angle perpendicular to the channel. The modeled floodplain

topography is intended to represent an active alluvial floodplain formed and continually

reworked by vertical and lateral accretion of sediment. However, no attempt is made to

explicitly model changes in floodplain morphology such as floodplain aggradation in

response to sediment deposition or stripping of the floodplain surface in response to

large, high-energy flood events. More complex channel-floodplain geometries could be

implemented with the model, such as the commonly observed asymmetrical channel with

a lower, depositional 'geomorphic bank' and higher 'cut' bank on the opposing side.

However, as our representation is attempting to capture a reach-average channel-

floodplain geometry wherein the relative elevation of opposing banks is implicitly

represented in the angle of divergence, this added complication is not necessary and is

unlikely to influence our model results in any meaningful way.

2.2.3. Hydraulic Model

Annual floodplain inundation is calculated using a simple one-dimensional

hydraulic model of steady, uniform flow. A diagram of the hydraulic model is available

in Figure 4. At each modeled time-step, the hydraulic model first calculates flow depth in

the channel, H_{ch} (m), as a function of peak flow (Q_p):

$$H_{ch} = \left[\frac{(1/Cz_{ch})^2 Q_p^2}{B_{bf}^2 gS} \right]^{1/3} \tag{5}$$

where Cz_{ch} is the Chezy friction coefficient of the channel and is determined by a sub-

model of the Li et al. (2015) hydraulic geometry relations:

$$Cz_{ch} = \alpha_R S^{-n_R} \tag{6}$$

Chezy friction coefficients were chosen to simulate hydraulic resistance in order keep

stage calculations consistent with the scheme used to calculate bankfull flow depth in the

Channel-Floodplain Cross Section

$$\frac{B_{bf}}{D} = \frac{(D^*)^{2.5}}{\alpha_{EH}\alpha_R{}^2\sqrt{R}\beta^{2.5}\left(\frac{RD^*}{\alpha_{EH}\alpha_R\beta}\right)^{\frac{2.5m-2n_R}{1+m-n_R}}}\left(\frac{Q_{tbf}}{Q_{bf}}\right)^{\frac{2.5m-2n_R}{1+m-n_R}}\frac{Q_{tbf}}{\sqrt{gD}D^2}$$

$$\frac{H_{bf}}{D} = \frac{\alpha_{EH}\alpha_R\beta^2}{(D^*)^2}\left(\frac{RD^*}{\alpha_{EH}\alpha_R\beta}\right)^{\frac{2m-n_R}{1+m-n_R}}\left(\frac{Q_{tbf}}{Q_{bf}}\right)^{\frac{2m-n_R}{1+m-n_R}}\frac{Q_{bf}}{Q_{tbf}}$$

Channel Profile

Channel Slope = Δ in elevation / Δ in distance along channel bed

$$S = \left(\frac{RD^*}{\alpha_{EH}\alpha_R\beta}\right)^{\frac{1}{1+m-n_R}}\left(\frac{Q_{tbf}}{Q_{bf}}\right)^{\frac{1}{1+m-n_R}}$$
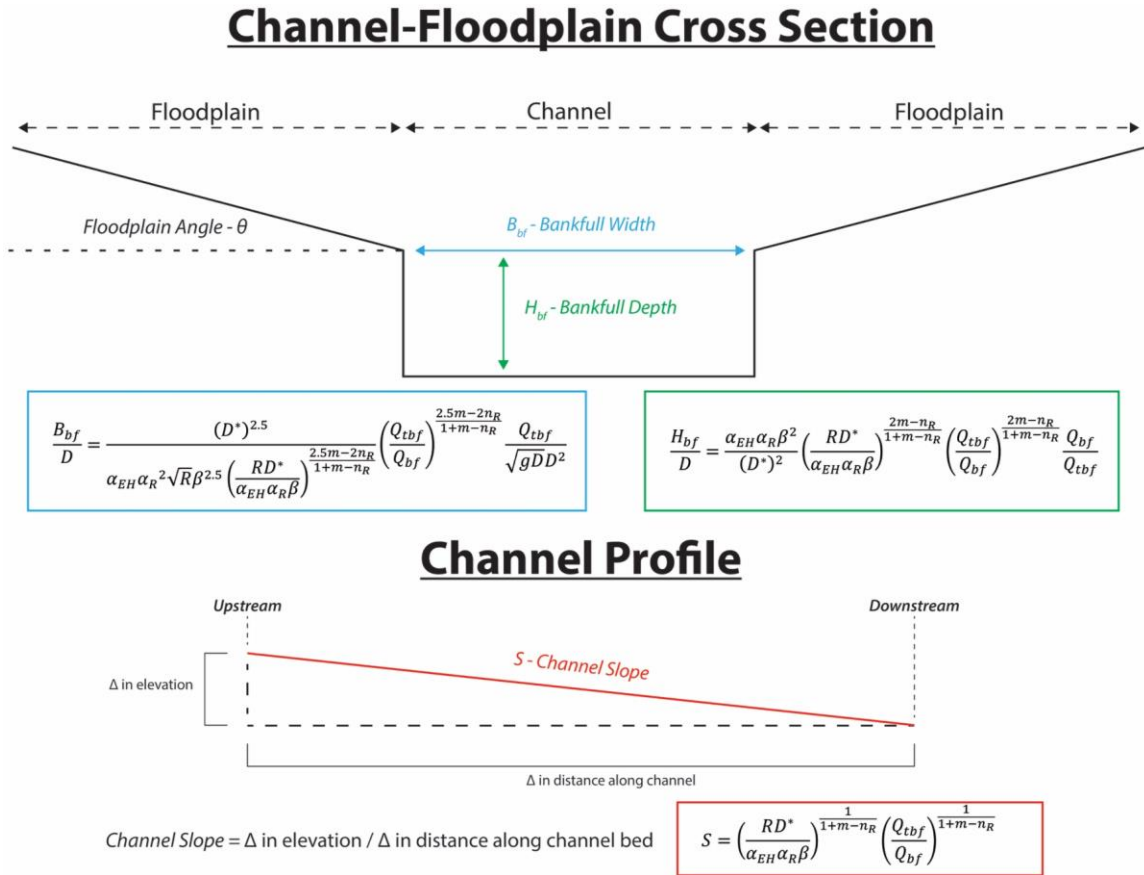
Figure 3. Illustration of simplified channel-floodplain cross-section (above), the channel profile (below), and the accompanying bankfull hydraulic geometry relations from *Li et al.* [2015].

Li et al. [2015] hydraulic geometry relations. If flow depth (H_{ch}) exceeds bankfull depth (H_{bf}), floodplain inundation occurs in that time-step and an iterative scheme is used to partition Q_p between discharge in the channel, Q_{ch} (m³/s), and discharge in the floodplain, Q_f (m³/s), until equal water surface elevations are calculated for flows within the channel (where $H_{ch} = H_{bf} + H_e$), and on the floodplain (H_f). In more formal terms, while $Q_p = Q_{ch} + Q_f$ and $H_e = H_{ch} - H_f$, iterative discharge partitioning is performed until $H_e = H_f$:

$$H_e = \left[\frac{(1/Cz_{ch})^2 Q_e^2}{B_{bf}^2 gS}\right]^{1/3} \tag{7}$$

$$H_f = \left[\frac{(1/Cz_f)^2 Q_f^2}{(\tan\theta - 90)^2 gS_f}\right]^{1/3} \tag{8}$$

where Q_e (m³/s) is the extra discharge partitioned within the domain of the channel above

bankfull discharge (Q_{bf}), Cz_f is the Chezy friction coefficient for the floodplain, and S_f

is the floodplain slope. As the version of the model used for this paper does not simulate

changes in the floodplain, we necessarily assume that the floodplain's slope and

hydraulic resistance also do not change. Thus, Cz_f and S_f are user-specified parameters

that are held constant for the duration of model runs. For model runs presented here, a

value for Cz_f of 2.01 is used to characterize the comparatively higher frictional resistance

of a vegetated floodplain relative to the channel, and a value for S_f of 0.0004 is used to

characterize the comparatively higher slope of a floodplain relative to a meandering

channel. These values are loosely based on the mainstem Minnesota River near Mankato,

Minnesota, which has an average channel slope (S) of 0.00022 and channel sinuosity (Ω)

of 2 [*Li*, 2014]. Using the equation $S_f = S \cdot \Omega$, we derived that $S_f \sim 0.0004$. The value

2.01 for Cz_f was chosen as representative of the low end of the range of values estimated

by *Li* [2014] for the Minnesota River gage near Jordan, Minnesota.

Finally, the width of inundated floodplain, B_f, is calculated as:

$$B_f = 2H_f(\tan\theta - 90) + B_{bf} \tag{9}$$

2.2.4. Sediment Supply Relation

The model's scheme for simulating channel adjustment (presented in detail below in section 2.4.5) requires that a sediment supply rate, Q_s (m³/s), is calculated for each time-step. Sediment supply influences the rate of channel adjustment on an annual basis

a) No Floodplain Inundation

Floodplain Angle θ

Q_{ch} H_{ch}

b) Floodplain Inundation

B_f

Q_f H_f H_f Q_f

Floodplain Angle θ

Q_{ch} H_{ch}

B_f

Q_f H_f Q_e H_e H_f Q_f

Floodplain Angle θ

Q_{bf} H_{bf}
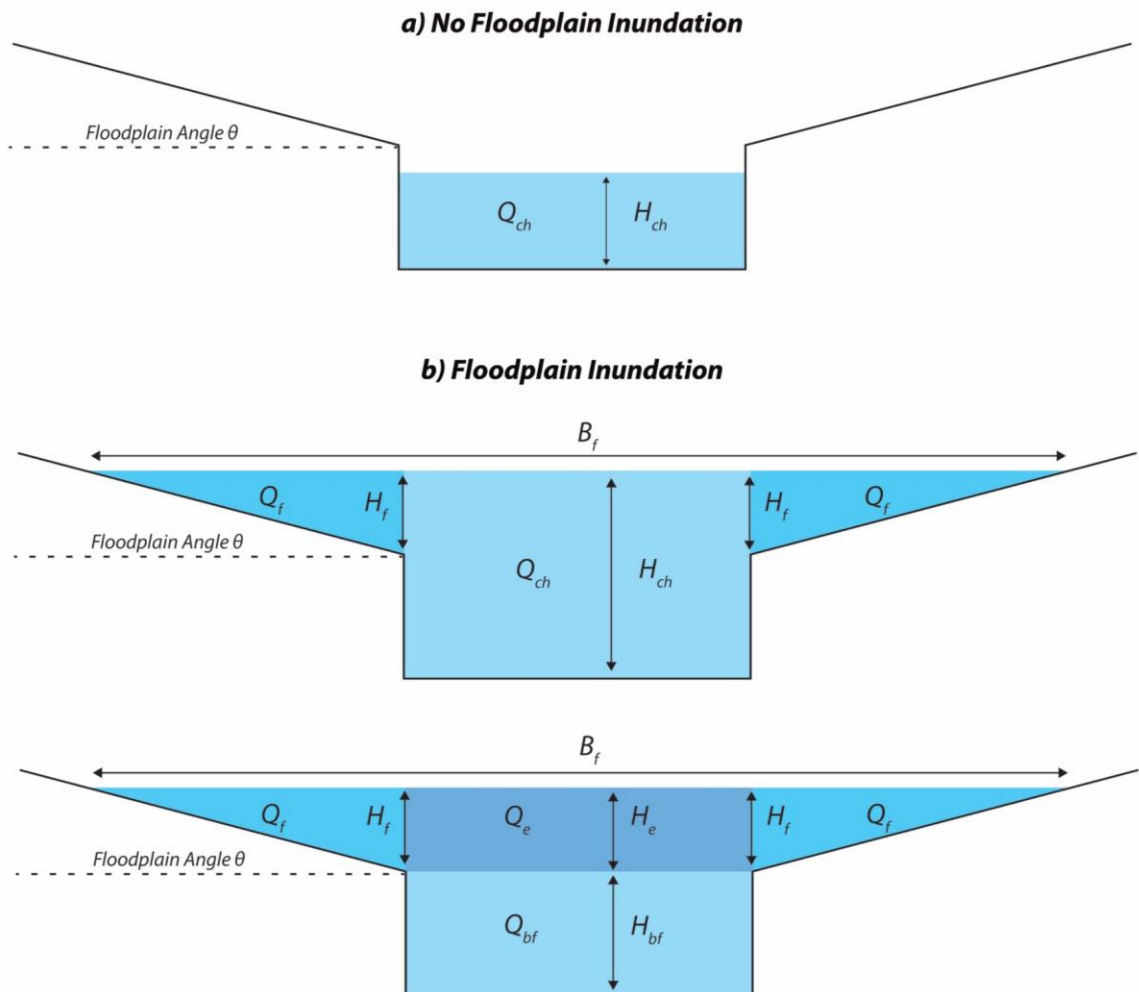
Figure 4. Illustration of simple 1-D hydraulic model: a) shows the scheme for determining channel depth when floodplain inundation does not occur, and b) shows the iterative scheme for determining channel depth and the width of floodplain inundation.

because the channel incrementally adjusts by some fraction towards an equilibrium

geometry determined by each year's peak discharge and corresponding sediment supply

rate.

Sediment supply is computed on an annual basis using a specified relationship

between peak discharge (Q_p) and sediment supply rate (Q_s). This relationship is

unchanging throughout the model run, consistent with the notion of a "supply reach", an

upstream reach-averaged channel-floodplain cross-section whose geometry is the same as

modeled cross-section at the initial time-step. The supply reach's geometry is held

constant over the entire duration of each model run. The hydraulic model presented in

section 2.4.3 is used to calculate the channel depth ($H_{ch,supply}$) of peak discharge (Q_p) in

the supply reach at each time-step:

$$H_{ch,supply} = \left[\frac{\left(1/Cz_{ch,supply}\right)^2 Q_p^2}{B_{supply}^2 g S_{supply}} \right]^{1/3} \tag{10}$$

Sediment supply to the modeled, adjustable channel-floodplain cross-section

downstream, Q_s (m³/s), is then calculated as the total transport capacity of the supply

reach where the unit transport capacity of the flow in the channel, q_s (m³/s) is calculated

as a function of the supply reach's Shields number (τ_{supply}^*):

$$\tau_{supply}^* = \frac{H_{ch,supply} S_{supply}}{RD} \tag{11}$$

$$q_s = \alpha_{EH} Cz_{ch,supply}^2 \sqrt{RgD} D \left(\tau_{supply}^*\right)^{5/2} \tag{12}$$

$$Q_s = q_s B_{supply} \tag{13}$$

Channel geometries can vary significantly between different sediment supply relations. For example, holding bankfull discharge constant and increasing bankfull transport capacity yields larger width-to-depth ratios and slopes while decreasing bankfull transport capacity yields smaller width-to-depth ratios and slopes. Therefore, care should be taken to determine that the initial transport capacity ($Q_{tbf,init}$), which ultimately sets the relation between discharge and sediment supply rate in the supply reach, yields reasonable channel geometries.

2.2.5. Channel Adjustment Scheme

Channel adjustment is simulated using a modified form of the empirically-based hydraulic geometry relations of *Li et al.* [2015] presented in section 2.2.2 to calculate predictions at each time-step for bankfull width, B_{pred} (m), bankfull depth, H_{pred} (m), and channel slope, S_{pred} (dimensionless). The relations are modified by replacing the input variables, bankfull discharge (Q_{bf}) and bankfull transport capacity (Q_{tbf}), with peak discharge (Q_p) and sediment supply rate (Q_s) respectively:

$$\frac{B_{pred}}{D} = \frac{(D^*)^{2.5}}{\alpha_{EH}\alpha_R{}^2\sqrt{R}\beta^{2.5}\left(\frac{RD^*}{\alpha_{EH}\alpha_R\beta}\right)^{\frac{2.5m-2n_R}{1+m-n_R}}}\left(\frac{Q_s}{Q_p}\right)^{\frac{2.5m-2n_R}{1+m-n_R}}\frac{Q_s}{\sqrt{gD}D^2} \qquad (14)$$

$$\frac{H_{pred}}{D} = \frac{\alpha_{EH}\alpha_R\beta^2}{(D^*)^2}\left(\frac{RD^*}{\alpha_{EH}\alpha_R\beta}\right)^{\frac{2m-n_R}{1+m-n_R}}\left(\frac{Q_s}{Q_p}\right)^{\frac{2m-n_R}{1+m-n_R}}\frac{Q_p}{Q_s} \qquad (15)$$

$$S_{pred} = \left(\frac{RD^*}{\alpha_{EH}\alpha_R\beta}\right)^{\frac{1}{1+m-n_R}}\left(\frac{Q_s}{Q_p}\right)^{\frac{1}{1+m-n_R}} \qquad (16)$$

The predicted channel geometry can be thought of as the equilibrium geometry to which the channel would adjust if peak discharge (Q_p) and the corresponding sediment supply rate (Q_s) were held constant for a sufficient length of time. It is unreasonable, however, to assume that a channel would be able to fully adjust towards its long-term, equilibrium predicted geometry in one time-step, due to factors such as bank cohesion/resistance or differential rates of aggradation and degradation controlled by the sediment supply relative to transport capacity. Therefore, we limit the fraction of adjustment towards the equilibrium (long-term) prediction that can be accomplished by the channel in any given year. This is accomplished by introducing user-specified adjustment-parameters that define the fractions of adjustment that the channel can actually make towards its predicted form each year. Below we describe three methods to implement this adjustment rate limitation using one or two parameters.

While some progress has been made in deterministic modeling of bank erosion, we are still far from a fully predictive model of channel width adjustment [*Simon and Thomas*, 2011]. Such a model would need to incorporate a robust physical basis for relating specific measures of bank cohesion and vegetative resistance to expected amounts of erosion for a given flow or shear stress coupled with a sub-model of bank deposition, vegetation encroachment, and the subsequent feedbacks between the two. To overcome this limitation, we devised a much simpler approach that represents different channel environments conceptually.

Three different methods are employed to simulate channel adjustments across a continuum of environments (a diagram illustrating the channel adjustment scheme and its

three different methods is available for reference in Figure 5). Method A is the simplest

of the three and simulates a channel environment where width, depth, and slope all adjust

at a uniform fraction of adjustment that is the same whether a channel geometry is

expanding or contracting (i.e., the fraction of adjustment is the same whether widening or

narrowing occurs). Method A utilizes a single, user-specified adjustment-parameter, β_a,

that can have any value between 0.0 and 1.0, and is used to calculate the next time-step's

channel geometry using the following equations:

$$B_{i+1} = B_i + \beta_a \left(B_{pred} - B_i \right) \tag{17}$$

$$H_{i+1} = H_i + \beta_a \left(H_{pred} - H_i \right) \tag{18}$$

$$S_{i+1} = S_i + \beta_a \left(S_{pred} - S_i \right) \tag{19}$$

where B_i, H_i, and S_i are the current width, depth, and slope, and B_{i+1}, H_{i+1}, and S_{i+1} are

the width, depth, and slope values that define the next time-step's bankfull channel

geometry.

However, adjustments in channel width are often constrained independently from

adjustments in depth and slope. The ability of a channel to widen is largely dependent on

the strength of its banks relative to shear stresses acting against them. On the other hand,

channel narrowing and adjustments in depth and slope are largely dependent on the

channel's sediment supply relative to sediment transport capacity and the ability of

riparian vegetation to colonize and stabilize banks. Thus, Method A allows for allometric

changes (expansion or contraction) in channel geometry, but does not allow for the

channel to accommodate preferential adjustment of width, depth or slope according to

given geomorphic conditions. Preferential adjustment of particular channel characteristics

are explored in methods B and C.

Method B assumes that the strength of the channel's banks differentiates the

channel's ability to widen from its ability to control narrowing and adjustments in depth

and slope. This is accomplished by introducing a second adjustment parameter, β_w, that

exclusively regulates channel widening and can have any value between 0.0 and 1.0. In

the event that B_{pred} is greater than B_i, the following equation for channel width is used

instead:

$$B_{i+1} = B_i + \beta_w(B_{pred} - B_i) \tag{20}$$

while narrowing and changes in depth and slope are predicted using equations 17-19.

Method C extends the notion of preferential adjustment to depth and slope as a

means to simulate differential responses between years with aggradation and degradation.

Both depth and slope are included together under the assumption that an adjustment in

depth will necessarily induce an adjustment in slope and vice versa. Specifically, Method

C assumes that the fractions of adjustments are uniform for width, depth, and slope, but

differ depending on whether or not an increase or decrease is predicted in each channel

geometry. This is accomplished by using two new adjustment parameters, β_e and β_c,

which control channel expansion (widening, deepening, steepening) and contraction

(narrowing, shallowing, flattening), respectively. Each can each have any value between

0.0 and 1.0. If B_{pred}, H_{pred}, or S_{pred}, is larger than B_i, H_i, and S_i respectively, then the
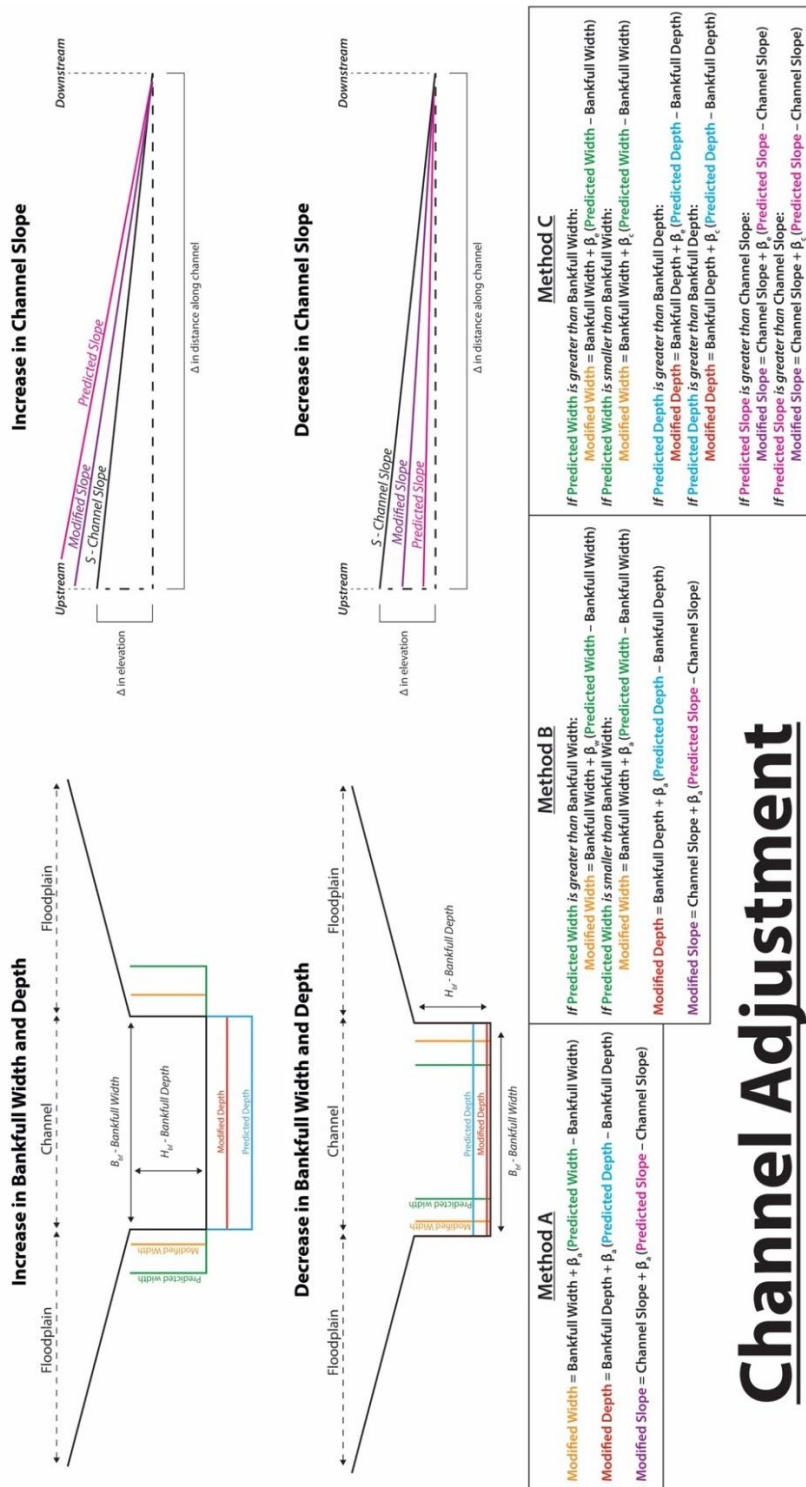
Figure 5. Illustration of channel adjustment scheme and the three different potential methods used to modify channel geometry predictions from hydraulic geometry relations using adjustment parameters.

corresponding channel dimension is calculated using the following equations:

$$B_{i+1} = B_i + \beta_e(B_{pred} - B_i) \tag{21}$$

$$H_{i+1} = H_i + \beta_e(H_{pred} - H_i) \tag{22}$$

$$S_{i+1} = S_i + \beta_e(S_{pred} - S_i) \tag{23}$$

If B_{pred}, H_{pred}, or S_{pred}, is smaller than B_i, H_i, and S_i respectively, then the

corresponding channel dimension is calculated using the following equations:

$$B_{i+1} = B_i + \beta_c(B_{pred} - B_i) \tag{24}$$

$$H_{i+1} = H_i + \beta_c(H_{pred} - H_i) \tag{25}$$

$$S_{i+1} = S_i + \beta_c(S_{pred} - S_i) \tag{26}$$

Examples of different channel environments classified by their qualitatively

characteristic ratios of bank cohesion relative to shear stress and sediment supply relative

to transport capacity are presented in Figure 6 along with potential adjustment parameter

values for methods B and C. It should be noted that these qualitative adjustment

parameter estimates have only been derived from visual inspection of their respective

photographs based on the characterization of their adjustment behavior within the

conceptual framework presented here. Figure 6a depicts a channel with a large sediment

supply and minimal bank cohesion, consistent with a lack of vegetation in the arid

environment depicted (β_a or β_c = high, β_w or β_e = high). Figure 6b depicts a channel

with comparatively similar capabilities of adjustments in width, depth, and slope (β_a or

β_c = moderate, β_w or β_e = moderate). Figure 6c depicts a channel with highly cohesive

banks and a limited sediment supply (β_a or β_c = moderate, β_w or β_e = low). Figure 6d

depicts a fully engineered channel with no ability to adjust width or depth due to

excessively high resistance to shear stress and negligible sediment supply (β_a or β_c =

0.0, β_w or β_e = 0.0).

All three methods are premised on the notion that a channel's geometries

incrementally adjust by some fraction towards a predicted equilibrium geometry every

year. This means that in a hypothetical experimental environment where discharge and

sediment supply remained constant, a channel out of equilibrium would eventually reach

its equilibrium form over a length of time determined by the value of the adjustment

parameter. To demonstrate this, an experiment using method A was run over a 1000-year

time length using a flood series consisting of a series of constant discharge values along

with a range of adjustment parameters. Results are displayed in Figure 7 for channel

width (a), depth (b), and slope (c).

Discharge (depicted by the black dashed line) is held constant for 200-year

increments before shifting to a new constant discharge for the next 200-year period.

Different values of β_a are used to show the relative differences in adjustment rate and are

colored by the adjustment parameter used. Relatively high adjustment parameters of β_a =

0.1 (yellow) and β_a = 0.025 (green) allow the channel to reach its equilibrium form

before discharge is shifted. However, adjustment parameters of β_a = 0.01 (red) and β_a =

0.005 (blue) result in a channel that never fully reaches its equilibrium form within the

200-year window, as a new target equilibrium is set by the new discharge and sediment

supply rate before full adjustment can occur. Extending this observation further to consider the variability of peak discharges and sediment supply rates in natural systems suggests that channels with limited adjustment capabilities may be perpetually out of equilibrium if the target equilibrium is continuously changing.
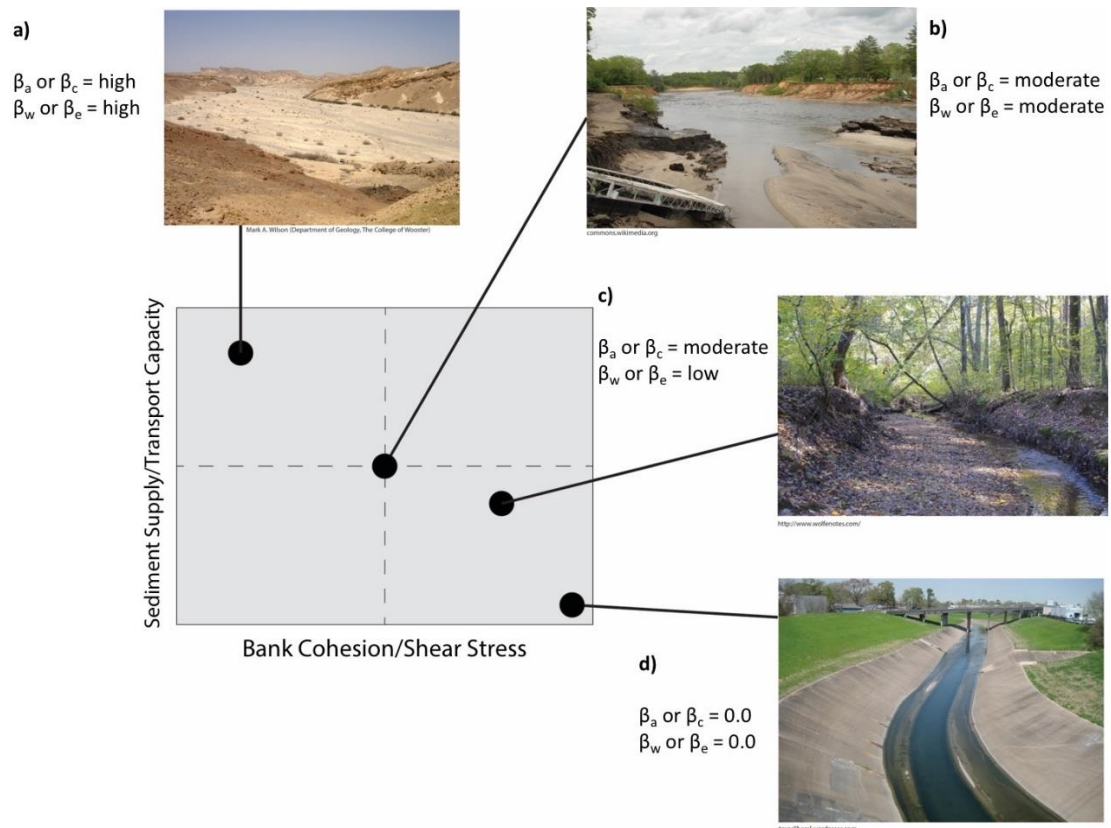
Figure 6. Different channel environments classified by their relative ratios of sediment supply to transport capacity and bank cohesion to shear stress, as well as potential parameters that may best characterize their adjustment dynamics for adjustment methods B and C.
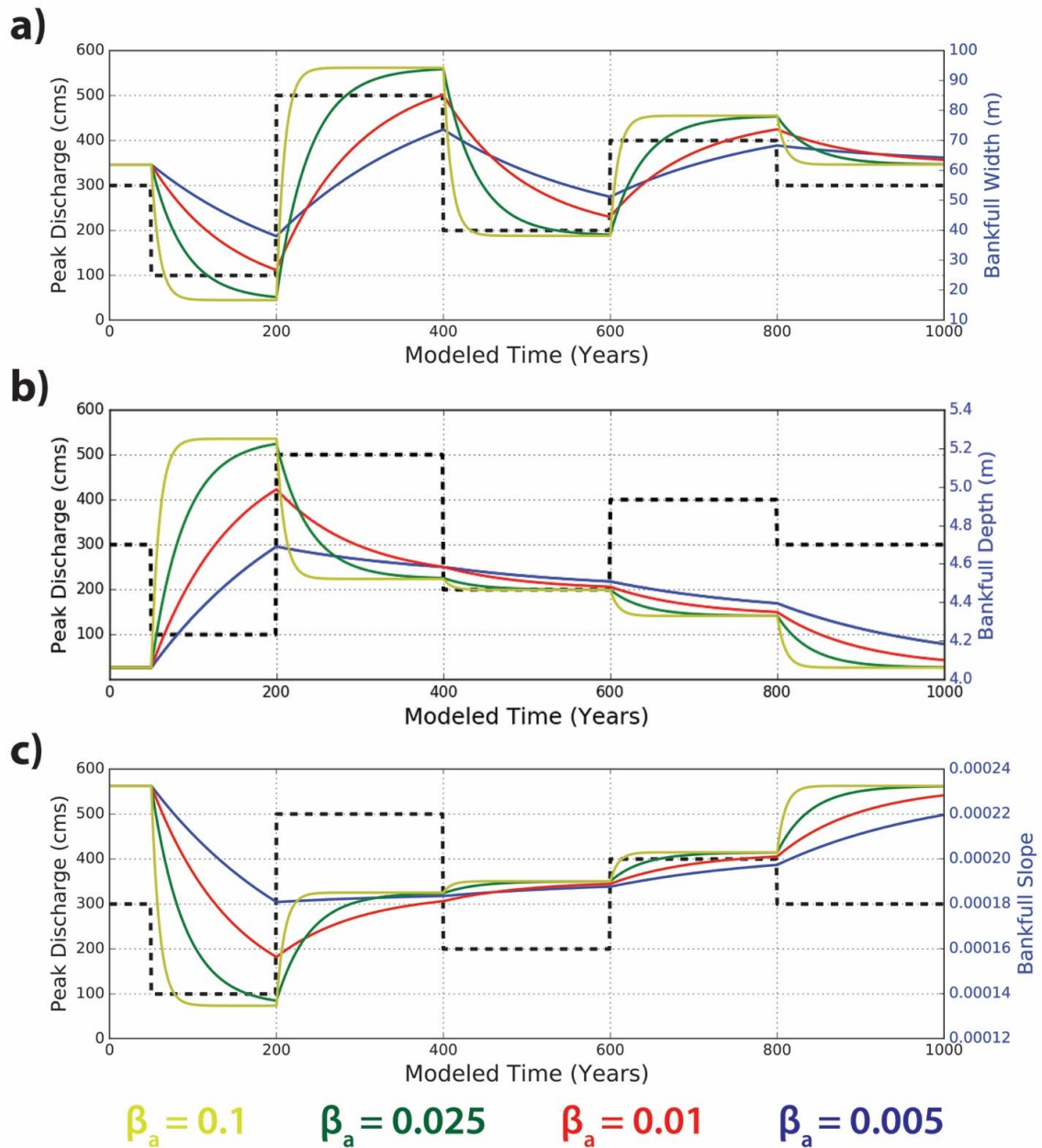
Figure 7. Results from experimental model runs where the peak discharge is constant (black dashed line) and changes every two-hundred years: a) bankfull width, b) bankfull depth, c) Slope. Adjustment method A is used with different values of the adjustment parameter, β_a, to show the relative differences in response time between them. Lines are colored by the corresponding adjustment parameter used in each model run: yellow = 0.1, green = 0.025, red = 0.01, and blue = 0.005.

2.3. Model Assumptions

Due to the many non-linear interactions in fluvial systems, the applicability of our reduced complexity model is necessarily targeted to a range of specified conditions and constrained by a number of approximations. While it is recognized that the duration of peak flows can influence the magnitude of channel response and that multiple geomorphically effective flows can happen in a year, channel predictions are calculated solely based on the magnitude of peak flows in a maximum annual series. This is consistent with a long line of empirical studies fitting hydraulic geometry relations to characteristic index discharges and it is not our intent to reformulate such methodologies within the scope of this study. We are simply interested in using existing methodologies to examine how flood inundation changes under non-stationary flow regimes with adjustable channels.

Furthermore, floodplain topography is assumed to remain static relative to channel changes as parameters for the floodplain slope, hydraulic roughness, and floodplain angle (slope of floodplain surface perpendicular to the channel) are held constant throughout the duration of model runs. Although vegetation type or density can change on the floodplain as a result of flood inundation frequency and/or magnitude, this feedback is beyond the scope of the current model. However, we doubt our results are systematically biased by its absence due to the variety of potential trajectories that the simulation of floodplain vegetation dynamics might take.

CHAPTER 3

EMPIRICAL DATA

Empirical analysis was performed in order to constrain model parameters and examine how well the model represents the basic dynamics of real river systems. First, we performed a basic flood frequency analysis to evaluate how the parameters characterizing flood probability density functions (PDFs) are changing in real systems. Specifically, we examined changes in annual peak flows for three river basins in Minnesota: The Minnesota River Basin (MRB), the Red River Basin (RRB), and the Upper Mississippi River Basin (UMR) between the confluence of the St. Croix River and the Mississippi River at Winona, Minnesota. This region was chosen due to the presence of significant systematic changes in atmospheric and surface hydrology during the latter half of the twentieth century reflect the type of non-stationary hydrologic conditions under consideration in this work. We additionally analyzed changes in channel geometry from repeat channel cross-section survey data for the Le Sueur and Maple rivers between 2008 and 2015, allowing us to test the hydraulic geometry relations of *Li et al.* [2015] with real data and gage how well the model is able to capture the measured changes. This timeframe is particularly helpful because it allows us to examine the impacts of two large flow events in 2010 and 2014 on both rivers.

The Le Sueur River and Maple rivers are two tributaries of the Blue Earth drainage basin in the MRB. The greater MRB is of interest as it has experienced an increased frequency of large magnitude flows as a result of land-use and climate changes during the mid-twentieth century [*Foufoula-Georgiou et al.*, 2015] that has resulted in

significant changes to channel geometry [*Schottler et al.*, 2014]. The Le Sueur River and Maple rivers are additionally of particular interest because of their unique geologic setting within two different geomorphic zones: 1) relatively stable flat upstream reaches, and 2) dynamic and rapidly incising downstream reaches within a knick zone created by a base level fall of the Minnesota River from the outburst of Lake Agassiz, an ancient glacial lake [*Belmont*, 2011; *Belmont et al.*, 2011; *Gran et al.*, 2011; *Gran et al.*, 2013]. Rapid erosion of stream banks and bluffs from channel adjustment within these two systems as a result of the recent shift in hydrology has led to an increase in fine-sediment supplied downstream, which in turn has resulted in significant channel adjustment, floodplain aggradation, and water quality impairment on the mainstem Minnesota River and further points downstream [*Belmont et al.*, 2011; *Markus*, 2011; *Lenhart et al.*, 2013].

3.1. Methods

We analyzed historic peak flow at 18 gages in the RRB, 13 gages in the MRB, and 10 gages in the UMR (41 gages in total). In order to examine if and how peak flows may change over time, GEV PDFs were fitted to subsets of the peak flow records split into two series for events before and after 1980 using the open-source *lmoments* package available for the Python programming language. This analysis allows us to specifically examine how the mean, standard deviation, and coefficient of variation (standard deviation divided by mean) of the peak flow change over time. The year 1980 was chosen by visual inspection of peak flow series as it appears to approximately delineate a regional systematic change in the magnitude and variability of the flood regime. This date

also roughly corresponds to the widespread expansion of agricultural tile-drainage

practices throughout the MRB that began in the mid-1970s [*Schottler et al.*, 2014],

though it is understood that conversion of land use and associated changes in agricultural

drainage occurred progressively in different areas over a period of a few decades

[*Foufoula-Georgiou et al.*, 2015; *Kelly et al.*, in prep].

Repeat cross-section surveys were made on the Le Sueur and Maple rivers in the

MRB during the years 2008 and 2015. A total of 19 repeat cross-section surveys were

collected on the Le Sueur River with another 24 surveys on the Maple River (Figure 8).

Measurements of width and depth were collected with a real time kinematic (rtk) GPS

system or with a level and stadia rod when overhanging vegetation and/or topographic

features prevented sufficient spatial precision for rtkGPS measurements. Because field

measurements were impractical, one set of reach-average slope values were calculated for

each cross section using a 3-meter Digital Elevation Model within ArcGIS.

Cross-section measurements were also compared with the hydraulic geometry

relations of *Li et al.* [2015] by using the measured bankfull width, bankfull depth, and

slope of each cross-section to back-calculate bankfull discharge (Q_{bf}) and bankfull

transport capacity (Q_{tbf}) using the same hydraulic and flow calculations as used in the *Li

et al.* relations:

$$Cz = \alpha_R S^{-n_R} \tag{27}$$

$$U_{bf} = Cz \sqrt{gH_{bf}S} \tag{28}$$

$$Q_{bf} = B_{bf}H_{bf}U_{bf} \qquad (29)$$

$$\tau^* = \frac{H_{bf}S}{RD} \qquad (30)$$

$$q_{tbf} = \alpha_{EH}Cz^2\sqrt{RgD}D(\tau^*)^{5/2} \qquad (31)$$

$$Q_{tbf} = q_{tbf}B_{bf} \qquad (32)$$

A range of values for characteristic bed material grain-size (D_{50}) between 0.062 mm and 0.5 mm (sand) have been observed in field samples from the Le Sueur and Maple rivers [*S. Kelly*, personal communication]. However, a single grain size (*D*) of 0.3 mm was used to calculate transport capacity across all cross-sections after experimentation with different values within that range produced negligible differences. After bankfull discharge and bankfull transport capacity were calculated at each cross-section, the results were used as input values to back-calculate bankfull width, depth, and slope using the *Li et al.* [2015] hydraulic geometry relations. This allowed us to examine how well the *Li et al.* relations perform in describing antecedent channel geometries in real world systems. Due to different geomorphic environments and associated channel behavior between the two different geomorphic zones, aggregated mean bankfull width, bankfull depth, and slope of cross sections measurements were analyzed for the reaches upstream of the knick zone and reaches within the knick zone for both rivers in addition to each river in its entirety. Of the 44 total cross-section measurements, 12 of the 20 Le Sueur River cross-sections are located within the knick zone and the other 8 are located above,

while 14 of the Maple River cross-sections are located with the knick zone and the other 10 are located above.

Finally, our model was run using peak flow data for the years 2008 to 2015 (Figure 9a) at each of the measured cross-sections in order to test its applicability and goodness of fit between the three different adjustment methods and the corresponding range of potential adjustment parameters. The period between 2008 and 2015 is of particular interest as it encompasses both the first and fourth largest peak flow events since 1940 (Figure 9b). The 2008 cross-sections measurements were used as initial conditions and the 2015 measurements were used as model targets. Adjustment parameters were manually manipulated until the best fit was obtained as characterized by the minimum residual possible between 2015 measurements of width and depth individually and model output for the year 2015. The best fit for each cross-section between all three adjustment methods was then selected as the characteristic adjustment method for that cross-section.

3.2. Empirical Analysis Results

3.2.1. Peak Flow Data

The GEV PDF parameters fitted to peak flow records before and after 1980, as well as the differences in the mean, standard deviation, and coefficients of variation for the corresponding distributions are presented in Figure 10. The trajectories of adjustment for GEV PDF parameters are presented in Table 1. The total difference in GEV PDF parameters fitted to peak flow records before and after 1980, as well as the differences in the mean, standard deviation, and coefficients of variation for the corresponding

distributions are presented in Figure 11 with the difference by percent change presented in Figure 12.
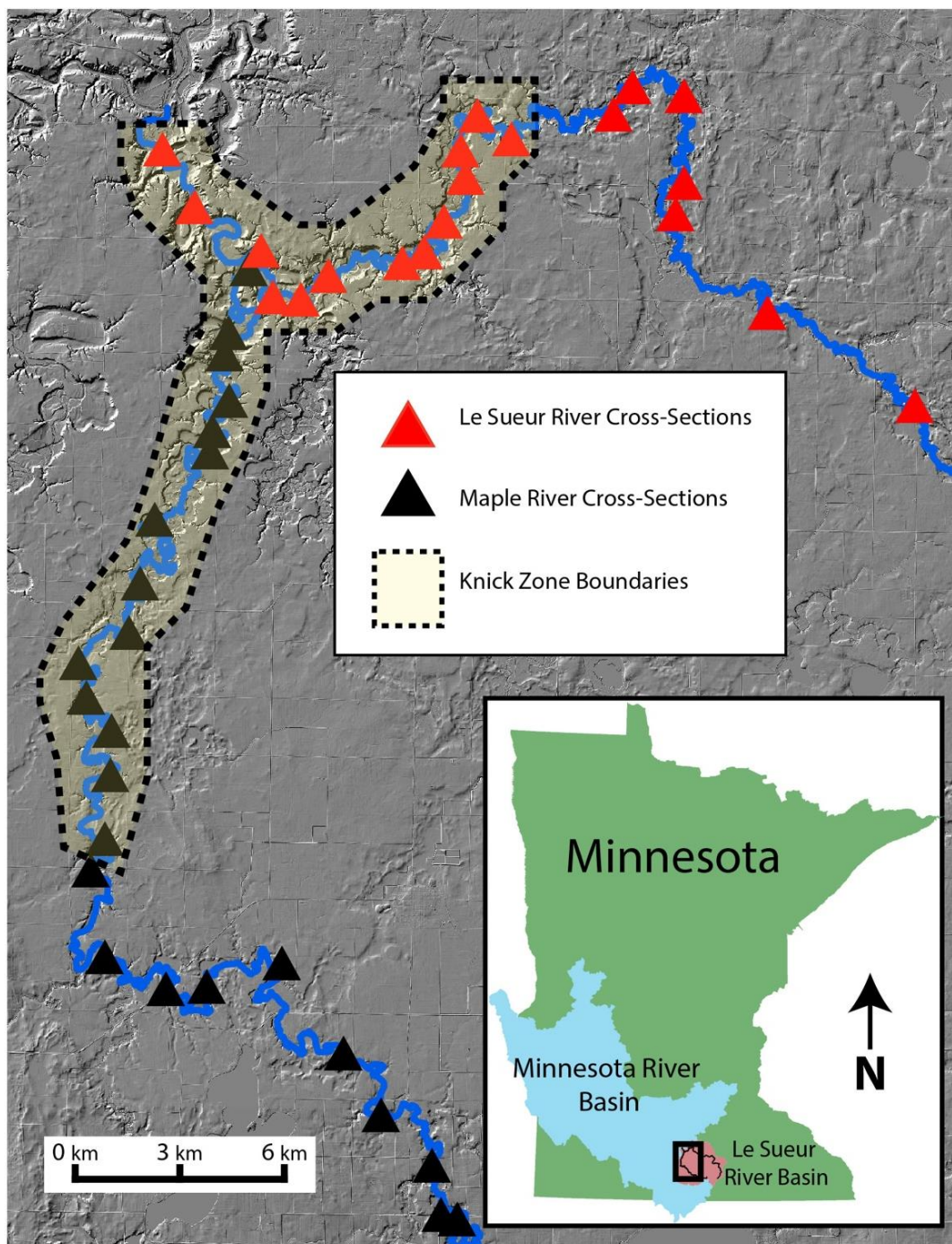
Figure 8. Map of measured cross-section locations for the Le Sueur (Red) and Maple (black) rivers with the downstream knick zone boundaries delineated (yellow).
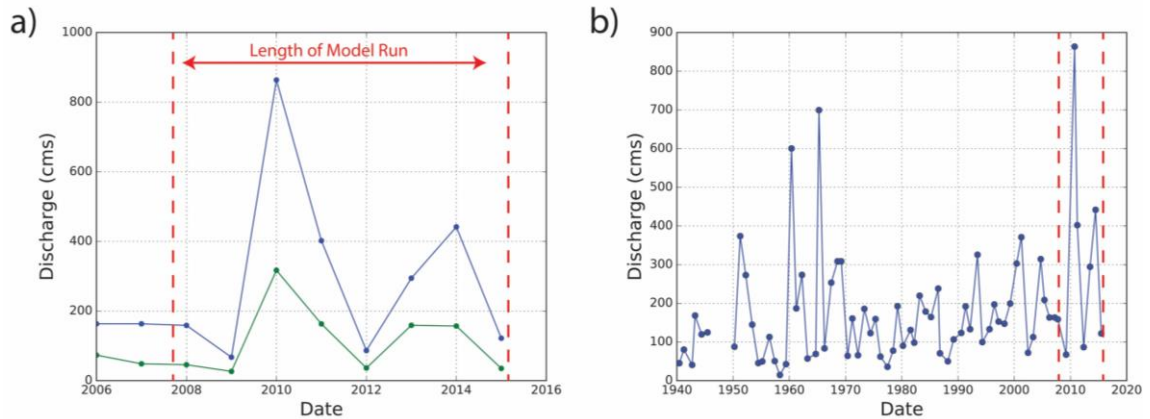
Figure 9. a) Peak flow data for the Le Sueur (blue) and Maple (green) Rivers used in model runs, b) peak flow data for the Le Sueur River going back to 1940.

Most of the analyzed gages have seen considerable increases in their location and scale parameters (83% and 68% respectively) and decreases in their shape parameter (68%). Additionally, most gages have seen considerable increases in the mean and standard deviation of their fit distributions (85% and 68% respectively), but the coefficients of variation have decreased by 63%. This suggests that increases in the standard deviation are not scaling with changes in the mean, thereby decreasing the coefficient of variation. In the MRB, 77% of gages had a decrease in the coefficient of variation while 92% had an increase in the mean and 69% had an increase in the standard deviation. The RRB exhibits a similar trend where 61% of gages had a decrease in the coefficient of variation while 89% had an increase in the mean and 72% had an increase in standard deviation. Additionally, decreases in the shape parameter lead to subsequent decreases in the distribution's mean and standard deviation. Therefore, the increases in

the mean and standard deviation across the MRB and RRB are somewhat offset by the many gages that decreased in their shape parameters (85% and 72%, respectively). Half of the gages in the UMR showed a decrease in the coefficient of variation while 70% had an increase in the mean and 60% had an increase in the standard deviation. Conversely, only 50% of the UMR's location parameters and 30% of the scale parameters increased. More gages likely saw increases in the mean and standard deviation while seeing greater decreases in the location and scale parameters because of the 60% of gages that had increases in their shape parameter.

In summary, the majority of gages in the RRB and MRB saw increases in their location and scale parameters along with increases in the mean and standard deviation of their distributions after 1980, but the majority of gages saw a decrease in the coefficient of variation, suggesting that increases in the standard deviation are not scaling proportionally with changes in the mean. The majority of gages in the UMR saw increases in the mean and standard deviation of their distributions after 1980, but this appears to be influenced more by increases in the shape parameter than increases in the location and scale parameters as was the case in the RRB and MRB. These results demonstrate that flood distributions are changing substantially and systematically in the upper Midwest, highlighting the urgent need for improved flood predictions under non-stationary conditions.
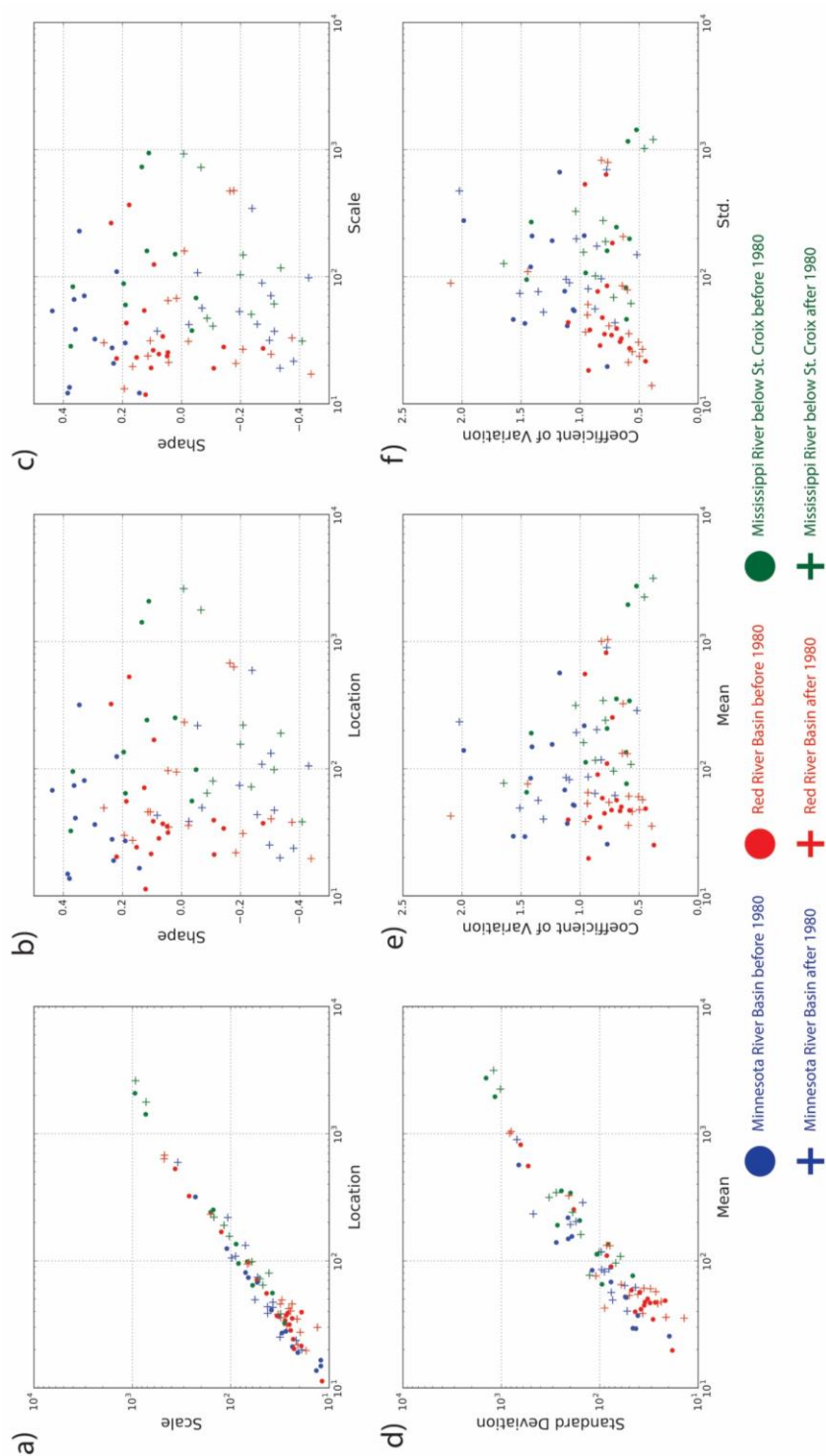
Figure 10. Generalized Extreme Value (GEV) PDF parameters fit to peak flow record before and after 1980 (a, b, c), and the corresponding mean, standard deviation (std.), and coefficients of variation (d, e, f).
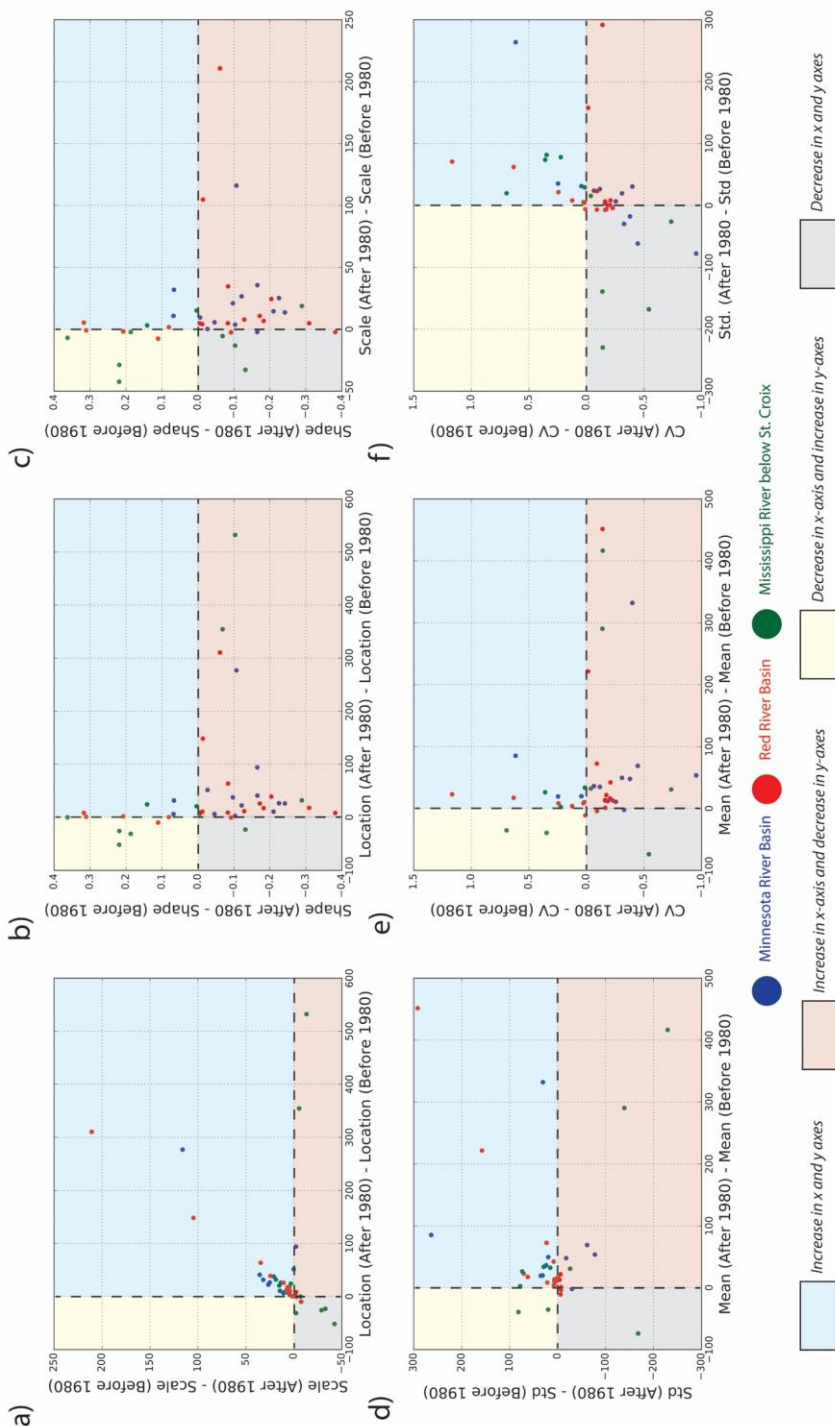
Figure 11. Differences in GEV PDF parameters fit to peak flow record before and after 1980 (a, b, c), and the corresponding differences in the mean, standard deviation (std.), and coefficient of variation (d, e, f).
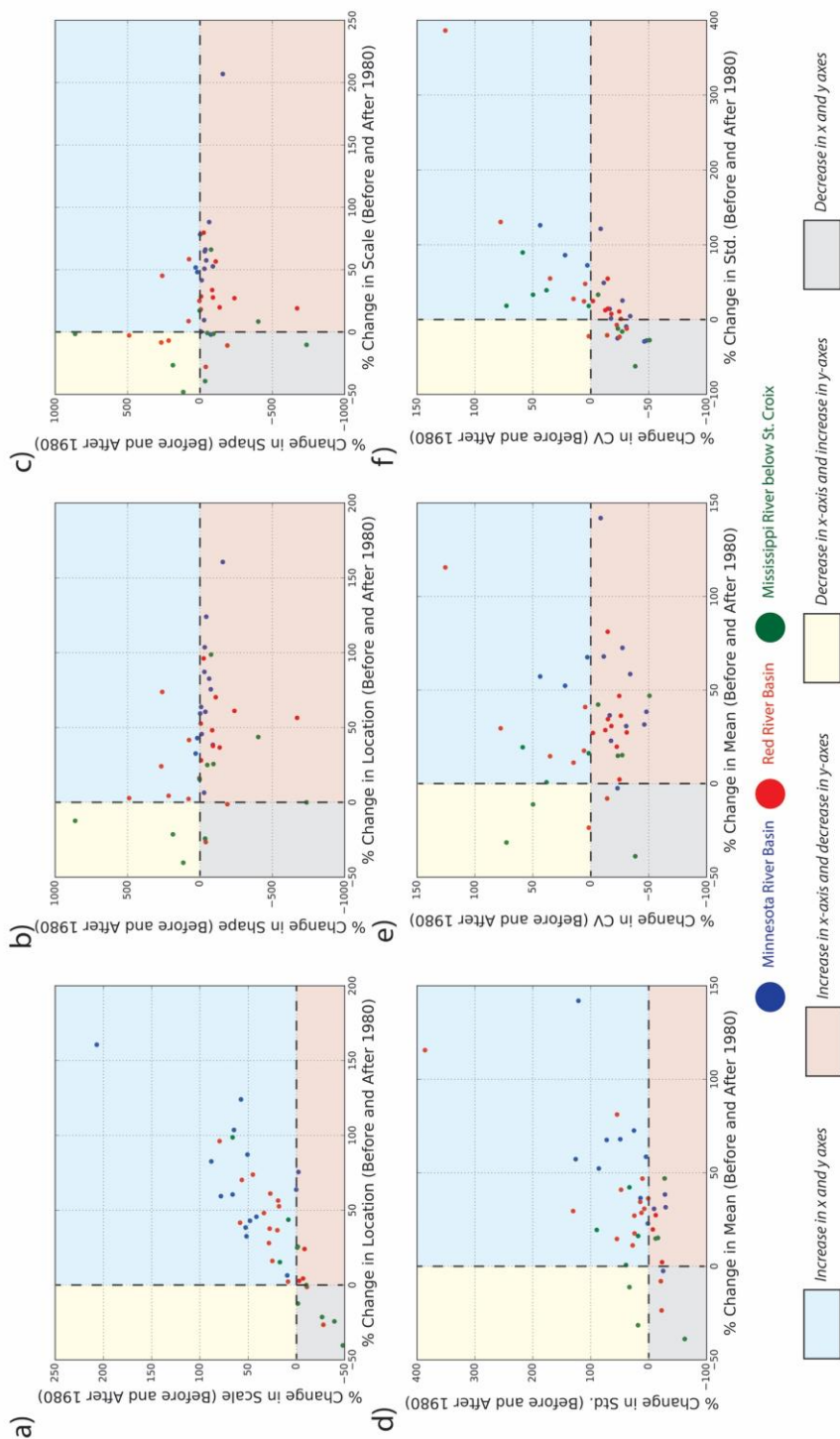
Figure 12. Percent change in GEV PDF parameters fit to peak flow record before and after 1980 (a, b, c), and the corresponding percent change in the mean, standard deviation (std.), and coefficient of variation (d, e, f).

Table 1. Trajectory of adjustment in PDF parameters (location, scale, and shape), and their corresponding summary statistics (mean, std., coefficient of variation) for the Minnesota, Red, and Mississippi (below St. Croix) Rivers.

	RED		MINNESOTA		MISSISSIPPI		ALL	
	Total	Percent	Total	Percent	Total	Percent	Total	Percent
RECORDS	18	100	13	100	10	100	41	100
LOCATION +	16	89	13	100	5	50	34	83
LOCATION -	2	11	0	0	5	50	7	17
SCALE +	13	72	12	92	3	30	28	68
SCALE -	5	28	1	8	7	70	13	32
SHAPE +	5	28	2	15	6	60	13	32
SHAPE -	13	72	11	85	4	40	28	68
MEAN +	16	89	12	92	7	70	35	85
MEAN -	2	11	1	8	3	30	6	15
STD. +	13	72	9	69	6	60	28	68
STD. -	5	28	4	31	4	40	13	32
CV +	7	39	3	23	5	50	15	37
CV -	11	61	10	77	5	50	26	63

3.2.2. Cross-Section Data

Measurements of slope, width, depth, and area at each cross-section on the Le Sueur and Maple rivers are presented in Figure 13 and Table C1, in addition to a summary of aggregated mean width, depth, and area changes for each river in its entirety and between reaches within and above the knick zone are available in Table 2. Comparisons between the measured and back-calculated widths, depths, areas, and slopes for each cross section on the Le Sueur and Maple rivers are available in Figure 14.

Overall channel changes were the largest on the Le Sueur River with mean width, depth, and area increasing by 18%, 29%, and 60% respectively between 2008 and 2015. The Maple River saw smaller mean width, depth, and area increases of 7%, 11%, and

21% respectively. Areas within the knick zone saw the largest amount of changes for both rivers. On the Le Sueur River, channel area increased by 85% within the knick zone with only 20% change above. While relative changes were slightly larger in channel width than depth above the knick zone (10% and 9%, respectively), changes in depth within the knick zone were nearly twice as large as changes in width (48% and 22%, respectively).

The Maple River saw smaller increases in channel area than the Le Sueur, with a 22% increase in channel area within the knick zone and 11% increase above. An increase of 10% in depth above the knick zone predominately contributed to the increase in area since changes in width were negligible, due in part to dense, woody riparian vegetation. In contrast to the knick zone of the Le Sueur River, the knick zone cross sections on the Maple River experienced similar change in width and depth (11% and 10%, respectively).

Visual inspection of Figures 14a (Le Sueur River) and Figure 14e (Maple River) shows that slope predictions are relatively close to slope measurements above the knick zone on both rivers. While the predictions diverge slightly more within the knick zone on the Maple River, predictions diverge much more within the knick zone and in the area slightly above it on the Le Sueur River.

Differences between measured and back-calculated mean width, depth, and area for the Le Sueur River and its sub-reaches above and within the knick zone were relatively small in 2008, but were much larger by 2015. In 2008, reaches above the knick
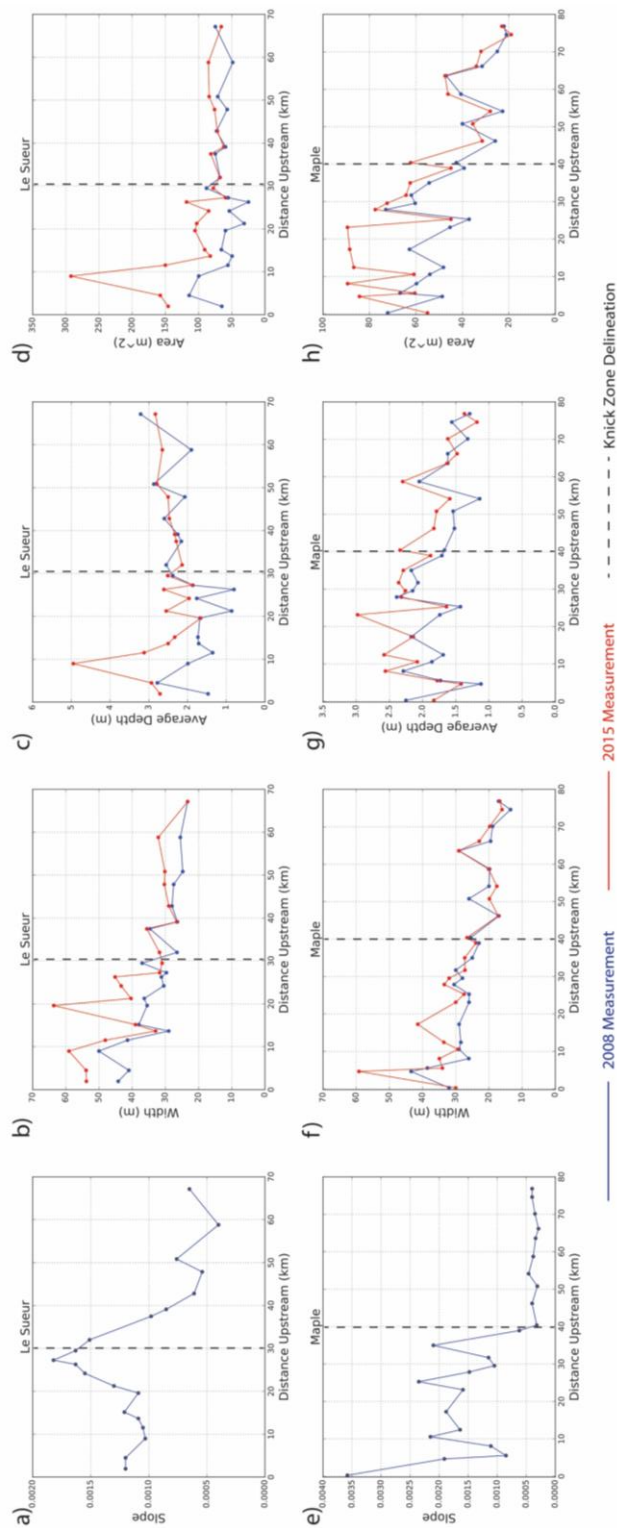
Figure 13. Cross-section measurements of slope (a and e), width (b and f), depth (c and g), and area (d and h) for the Le Sueur River (a, b, c, d) and Maple River (e, f, g, h).
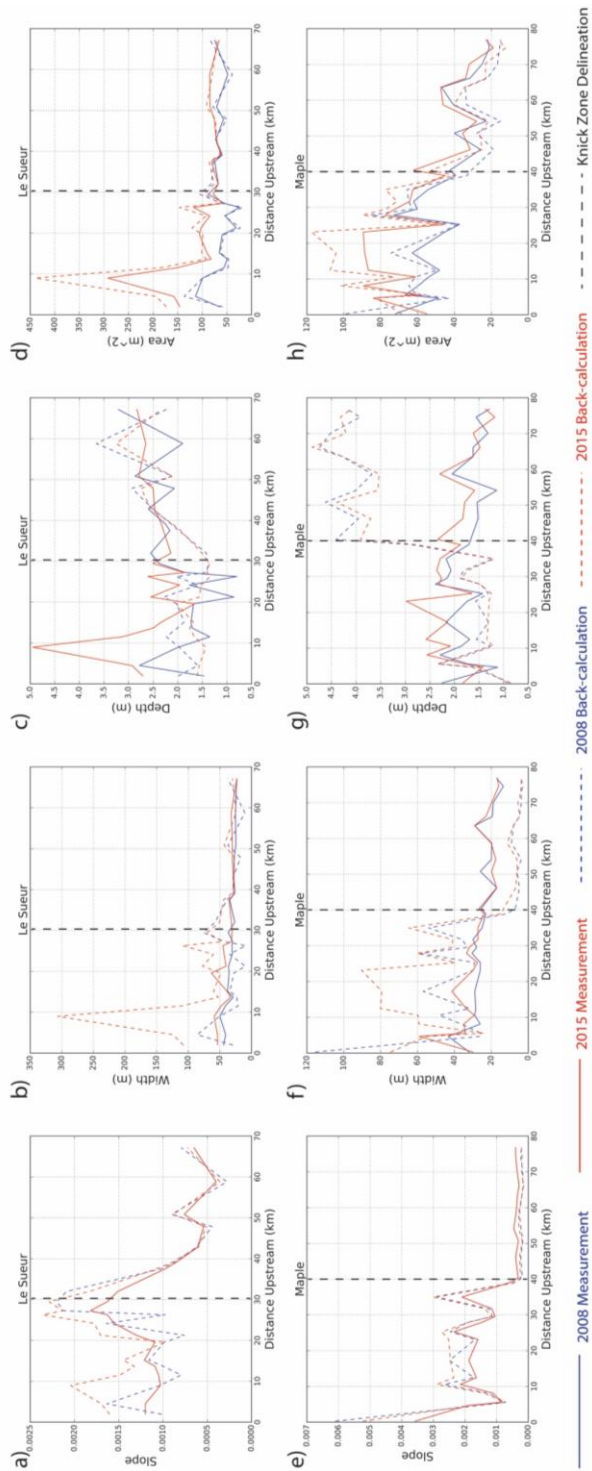
Figure 14. Cross-section measurements and back-calculations using the *Li et al.* [2015] hydraulic geometry relations of slope (a and e), width (b and f), depth (c and g), and area (d and h) for the Le Sueur River (a, b, c, d) and Maple River (e, f, g, h).

Table 2. Summary of mean channel width, depth, and area for the Le Sueur and Maple Rivers. Rows are grouped by aggregated measurements for the entire river (top), above the knick zone (middle), and within the knick zone (bottom).

	Le Sueur River				Maple River			
	2008	2015	Total Change	Percent Change	2008	2015	Total Change	Percent Change
Mean Width (m)	33.0	39.0	6.0	18%	24.7	26.5	1.8	7%
Mean Depth (m)	2.0	2.6	0.6	29%	1.7	1.9	0.2	11%
Mean Area (m^2)	64.4	103.1	38.6	60%	43.2	52.1	8.9	21%
Mean Width above knick zone	27.8	30.6	2.8	10%	19.4	19.4	0.1	0.3%
Mean Depth above knick zone	2.3	2.5	0.2	9%	1.5	1.7	0.1	10%
Mean Area above knick zone	63.9	76.7	12.8	20%	29.5	32.8	3.4	11%
Mean Width within knick zone	36.2	44.1	8.0	22%	29.2	32.5	3.3	11%
Mean Depth within knick zone	1.8	2.6	0.8	48%	2.0	2.2	0.2	10%
Mean Area within knick zone	63.8	118.1	54.2	85%	57.2	69.8	12.6	22%

zone were slightly wider and shallower than predicted, but became slightly narrower and deeper than predicted by the *Li et al.* [2015] relations by 2015 (Figures 14b and c). Conversely, the reaches within the knick zone were slightly narrower and of a similar depth as predicted in 2008, but were significantly narrower and deeper than predicted by the *Li et al.* [2015] relations by 2015 (Figures 14b and c). This is particularly apparent in the lower 15 km where the hydraulic geometry relations significantly over-predict an increase in width and fail to predict the significant increase in depth at all.

Differences between measured and predicted mean width, depth, and area for the Maple River and its sub-reaches above and within the knick zone were larger than those on the Le Sueur in 2008 (Figures 14f and g). Differences were largest in the reach above the knick zone where the measured channel was systematically wider and shallower than the back-calculated geometries derived from the *Li et al.* [2015] relations in both 2008 and 2015. Measurements from reaches within the knick zone, on the other hand, are

systematically narrower and deeper than back-calculated geometries in both 2008 and 2015. However, the overall differences between channel area measurements and back-calculations were relatively small. In order to better understand what may cause these systematic differences, we manually manipulated input values for channel slope in order to observe changes in the width-to-depth ratio of back-calculations and found that a near perfect fit was derived when cross-section slopes upstream of the Maple River's knick zone were increased by 0.001, which suggests that either our estimate of slope is slightly off, or this reach is out of equilibrium, potentially due to historical contingencies.

In summary, while we would not expect channels to have fully adjust to the equilibrium form predicted by the *Li et al.* [2015] relations, back-calculated geometries appear to match the 2008 width and depth measurements both above and within the knick zone of the Le Sueur River quite well. Differences between predictions and observations increased within the knick zone by 2015, consistent with our expectations that a) the channel would not fully adjust over such a short time period and b) the channel does not adjust allometrically (i.e., in proportion to the width/depth ratios that are implicit to the *Li et al.* [2015] relations), supporting use of the two parameter adjustment methods (B and C). The match between measurements and back-calculations of width and depth for the Maple River as a whole were worse than those of the Le Sueur as the back-calculated width-to-depth ratios were systematically different, particularly in the reach above the knick zone.

The pronounced differences between measurements and back-calculations also suggest that both rivers adjust differently above and below the knick zone, reflecting

differences in their respective geomorphic environments. Reaches above the knick zone

are freely meandering within a low gradient landscape. On the other hand, channels

within the knick zone are partially confined by bluffs composed of highly consolidated

glacial sediments in addition to bedrock outcrops on the lower 8 km of the Le Sueur

River that are both highly resistant to erosion and limit the channel's ability to widen

[*Gran et al.*, 2013]. This suggests that it is easier for channels to adjust their depth than

width in response to large floods, resulting in channels that are narrower and deeper than

predicted. This also strongly suggests that methods B or C are appropriate for model runs

in this system.

3.2.3. Model Results Compared with Repeat Cross Section Measurements

Input values for bankfull discharge (Q_{bf}) and bankfull transport capacity (Q_{tbf}) at

each cross-section are presented in Figure 15 along with values for back-calculated

bankfull velocity (U_{bf}) and the Chezy resistance coefficient (Cz). The adjustment

parameters and corresponding method of adjustment yielding the best fit at each cross-

section are presented in Figure 16a for the Le Sueur River and Figure 16b for the Maple

River. The differences between the 2015 width and depth measurements and model

outputs of 2015 are presented in Figure 16c for the Le Sueur River and Figure 16d for the

Maple River.

Of the 44 total cross-sections analyzed, Method B yielded the best fit at 31 sites

with Methods A and C yielding best fits at 7 and 6 cross-sections respectively. Of the Le

Sueur River's 20 cross-sections, 16 were deemed to have good fits with the other 4 not

being able to adequately predict changes in depth. These 4 are the most downstream

within the knick zone and could potentially be due to the presence of bluffs and bedrock outcrops, resulting in trajectories of adjustment that are uncharacteristic of fully alluvial channels and beyond the predictive capabilities of the model. Of the Maple River's 24 cross-section, 15 were deemed to have good fits with the other 9 not being able to adequately predict changes in depth. Like the Le Sueur, a sub-set of cross-sections within the Maple River's knick zone, roughly between 8 to 25 km upstream, were unable to predict changes in depth. Additionally, several cross-sections above the Maple River's knick zone resulted in poor fits for widths and depths, likely due to differences in the measured and back-calculated width-to-depth ratios in this reach (Figures 14f and g).

In summary, the model appears to reasonably predict width and depth adjustments for all of the Le Sueur River, aside from three cross-sections in the last 15 km, and the most downstream and upstream sections of the Maple River's knick zone. Through manual testing of different adjustment methods, Method B was found to be the most commonly applicable. This is likely due to the observed differences in adjustment mechanisms between channel width and channel depth as discussed in section 3.2.2. Results also demonstrate that the majority of fitted adjustment parameters are within a range of 0.0 and 0.1, but in some cases within the knick zone can exceed 0.2.
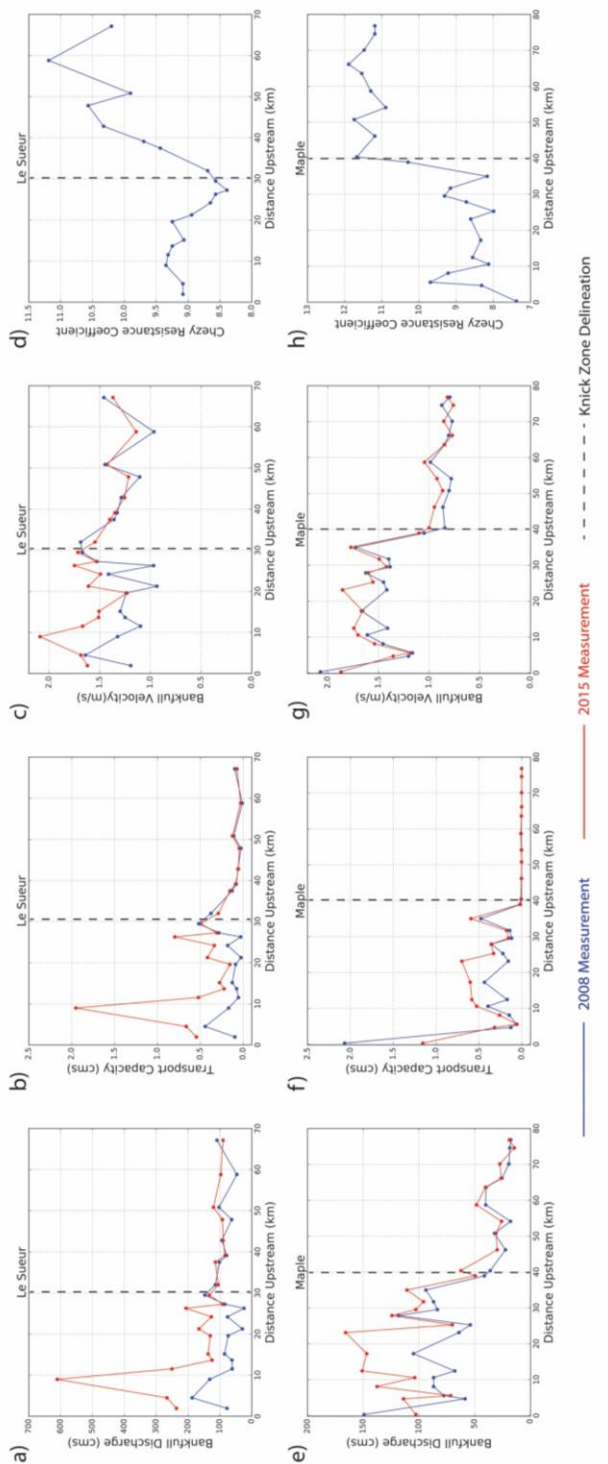
Figure 15. Back-calculations from cross-section measurements using *Li et al.* [2015] hydraulic geometry relations for bankfull discharge (a and e), bankfull transport capacity (b and f), bankfull velocity (c and g), and Chezy resistance coefficients (d and h) for the Le Sueur River (a, b, c, d) and Maple River (e, f, g, h).
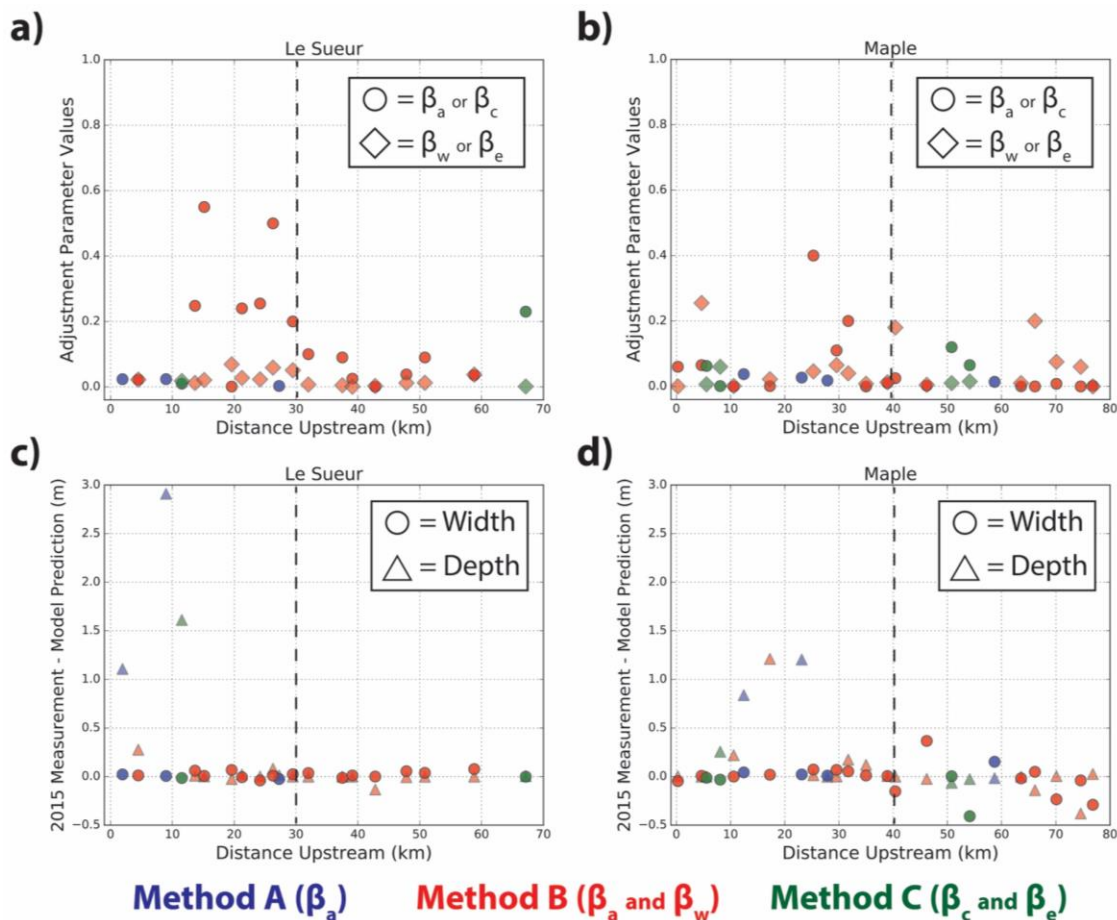
Figure 16. Adjustment parameters and the corresponding method of adjustment with the best fit at each cross-section are presented Le Sueur River (a) the Maple River (b), along with differences between the 2015 width and depth measurements and 2015 model outputs for the Le Sueur River (c) and the Maple River (d). Results are colored by the adjustment method determined to have the best fit between measurements and model outputs. For methods B and C, which have two adjustment parameters, each parameter is differentiated by different shapes in Figures a and b. The differences between the 2015 measurements and model outputs of 2015 in Figures d and d are also differentiated between width and depth by different shapes.

CHAPTER 4

HYPOTHETICAL SCENARIOS

Analyses presented above provide confidence that our approach is predicting

channel morphological adjustments in a reasonable manner on a reach-average basis and

that our adjustment parameters can be empirically constrained. In this section, we abstract

the inherent complexity of real world fluvial systems by using an ensemble of

hypothetical flow, sediment supply, and channel adjustment scenarios to explore how

changes in the mean and variance of a peak flow series influence the frequency and

magnitude of floodplain inundation.

4.1. Methods

We created six hypothetical annual peak discharge scenarios that each run for a

simulated timespan of 1000 years by randomly sampling from a Generalized Extreme

Value (GEV) PDF defined by location μ, scale σ, and shape ξ parameters, controlling the

distribution's mean, standard deviation, and skew, respectively. Non-stationary

conditions were simulated simply as an abrupt shift from one stationary state to another

by changing the PDF parameters at t = 500 years. A constant shape parameter of 0.2 was

chosen to minimize unnecessary complexity. Parameters for the first 500 years are

identical for all six scenarios ($\mu = 250$, $\sigma = 75$, $\xi = 0.2$), then parameters are changed

to different values in each scenario for the remaining 500 years of the simulation. The

location and scale parameters for the initial conditions and each of the six flow scenarios

are plotted in Figure 17a, the corresponding mean, standard deviation, and coefficients of

variation for each scenario are plotted in Figure 17b, and the PDFs are plotted in Figure
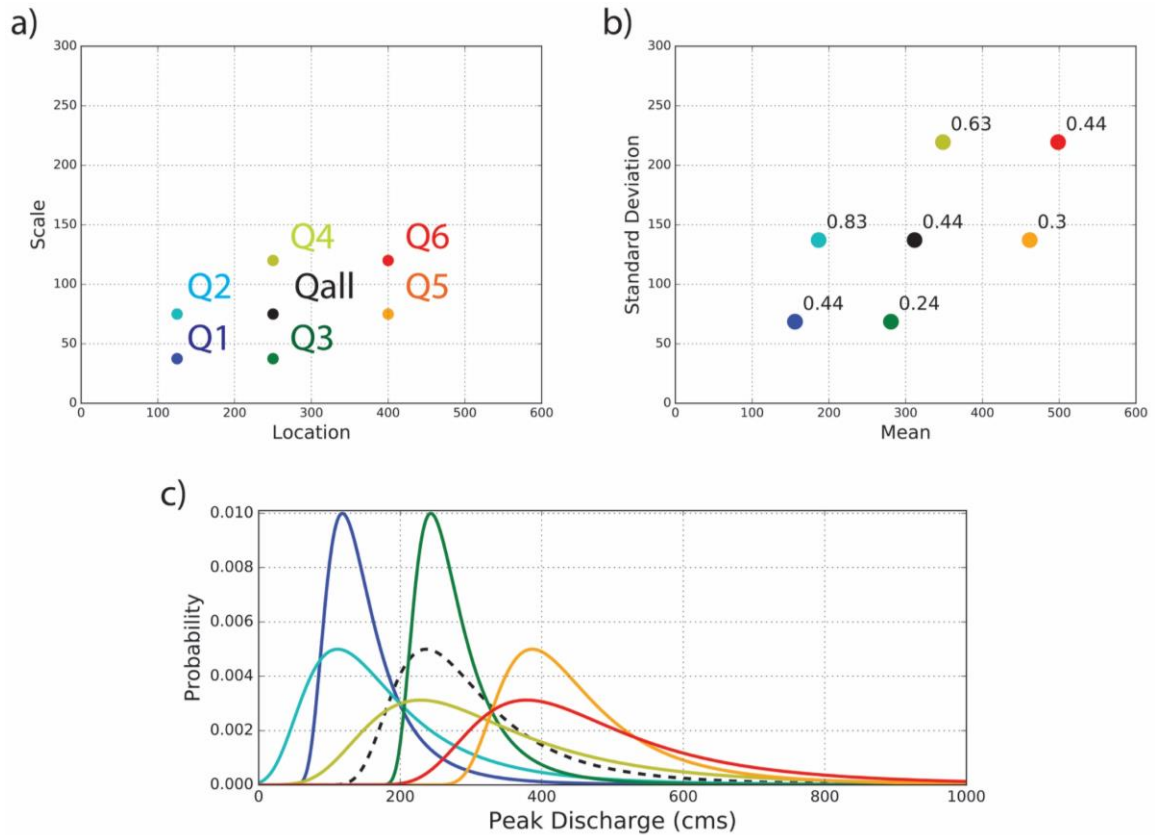
Figure 17. a) PDF parameters for the 6 flow scenarios and their initial PDF parameters (all scenarios have a shape parameter of 0.2), b) the corresponding mean and standard deviation of the distributions with the coefficient of variation (top-right of each point), and c) the GEV PDFs plotted for all scenarios by corresponding colors.

17c. A summary of flow scenario input parameters and their corresponding summary

statistics is also available in Table A2. From here on, each flow scenario will be

referenced with the letter Q and the corresponding scenario number (i.e., flow scenario 1

is Q1, flow scenario 2 is Q2, and etc.).

     Because sediment supply relative to discharge controls the width-to-depth ratio

and slope of predicted equilibrium channel geometries, each hydrologic scenario was
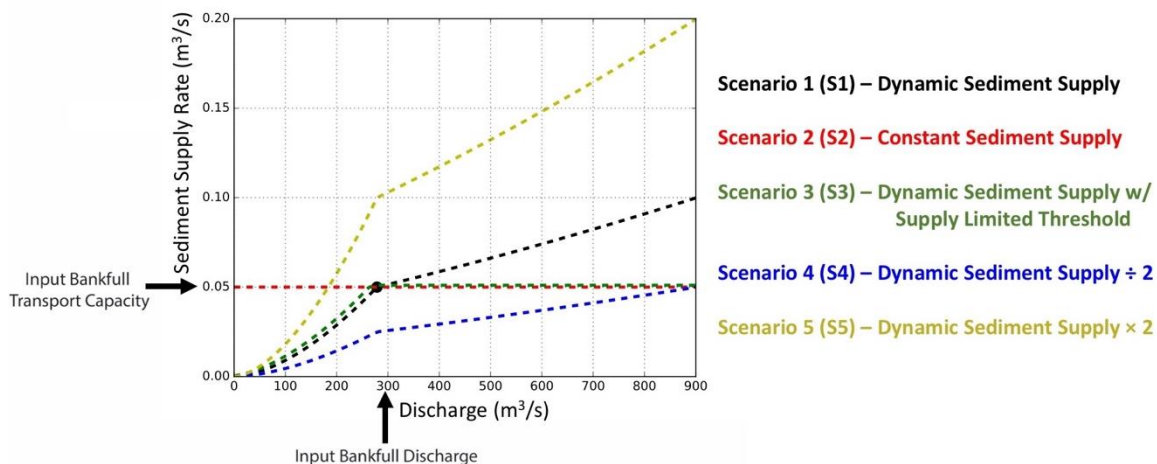
Figure 18. Relationships for the five different sediment supply rate scenarios that are functions of discharge along with the input bankfull discharge and bankfull transport capacity values that define the supply reach channel in all scenarios except for S2.

further tested with five different hypothetical sediment supply scenarios (Figure 18).

Scenario 1 (S1) uses the unmodified relation between peak discharge and sediment

supply rate defined by the transport capacity of the supply reach. Scenario 2 (S2) uses a

constant sediment supply rate as defined by the bankfull transport capacity of the supply

reach. Scenario 3 (S3) simulates supply limited conditions in which the sediment supply

rate is held constant for all flows that are above the bankfull transport capacity of the

supply reach. Scenarios 4 (S4) and 5 (S5) are based off the relation used for S1, with S4

halving the supply for any given discharge and S5 doubling the supply for any given

discharge.

Static input parameters used for all runs are presented in Table 3. Initial bankfull

discharge, $Q_{bf,init}$, was calculated as the median value from the initial distribution

specified in all model runs. Initial bankfull transport capacity, $Q_{tbf,init}$, was chosen as it

Table 3. Static parameters for hydrologic change scenarios.

Parameter	Variable	Static Value
Grain Size	D_{50}	0.3 (mm)
Floodplain Angle	θ	0.1 (degrees)
Floodplain Slope	S_f	0.0004
Chezy Floodplain Coefficient	Cz_f	2.01
Initial Bankfull Discharge	Q_{bf}	278 (m^3/s)
Initial Bankfull Transport Capacity	Q_{tbf}	0.05 (m^3/s)

appears to produce reasonable channel dimensions roughly based on the mainstem

Minnesota River near Mankato, Minnesota. Prior to each model run, a spin-up scheme

was used in which the model was run over the first 500 years of data with $\beta_a = 0.05$ in

order to allow the channel to adjust towards a characteristic equilibrium state determined

by the sediment supply scenario. This prevents aggregated statistics from model runs

being influenced by channel geometries that are chronically out of equilibrium in a non-

meaningful way.

Flow and sediment scenarios were repeatedly run at increments across a range of

adjustment parameter values for each of the three adjustment methods in order to

quantify the influence of all adjustment parameter combinations on the resulting channel

geometry and subsequent changes in the fraction of years with floodplain inundation as

well as the mean inundation width.

4.2. Results

Example model outputs for flow scenarios Q4, Q5, and Q6 using method A with $\beta_a = 0.05$ and sediment supply scenario S1 are presented in Figures 19-25 for: bankfull width (Figures 19), bankfull depth (Figures 20), bankfull area (Figures 21), slope (Figures 22), inundation widths (Figures 23), mean inundation width (Figures 24), and flood frequency (Figures 25). These flow scenarios were chosen to show differences in model output for changes only in the standard deviation (Q4), only in the mean (Q5), and changes in both the mean and standard deviation (Q6). Figures B1 through B30 present all model outputs with incrementally varying adjustment parameters from Methods A, B, and C, showing changes in the mean and standard deviation for width, depth, slope, and inundation width in addition to flood frequency, all aggregated from each model run.

4.2.1. Method A

Based on visual inspection of all model outputs for Method A (Figures A2 and A3), a general pattern of behavior emerges. An example of this behavior can be seen in a subset of these outputs for mean bankfull width in Figure 26 where the mean and standard deviation are plotted by flow scenario as a function of β_a for a range of values between 0.0 and 1.0 (Figures 26a and b, respectively) and a smaller range between 0.0 and 0.05 (Figures 26c and d, respectively). It is evident from this subset that mean channel widths converge in all flow scenarios to an equilibrium value around $\beta_a = 0.03$, after which they remain constant through $\beta_a = 1.0$ (Figures 26a and c). The standard deviation of channel widths, depths, and slopes exhibit rapid changes with parabolic shapes up to a value near $\beta_a = 0.02$, after which they increase in a non-linear fashion

until $\beta_a = 1.0$ (Figures 26b and d). This same behavior is observed in all method A

outputs for the mean and standard deviation of widths, depths, and slopes across all flow

and sediment scenarios. In order to examine how these equilibrium values relate to one

another, Figure 27 presents values for the mean and standard deviation of widths (a),

depths (b), slopes (c), and inundation widths (d) for values of $\beta_a = 0.05$ across all flow

and sediment scenarios (differentiated by flow and shape, respectively).
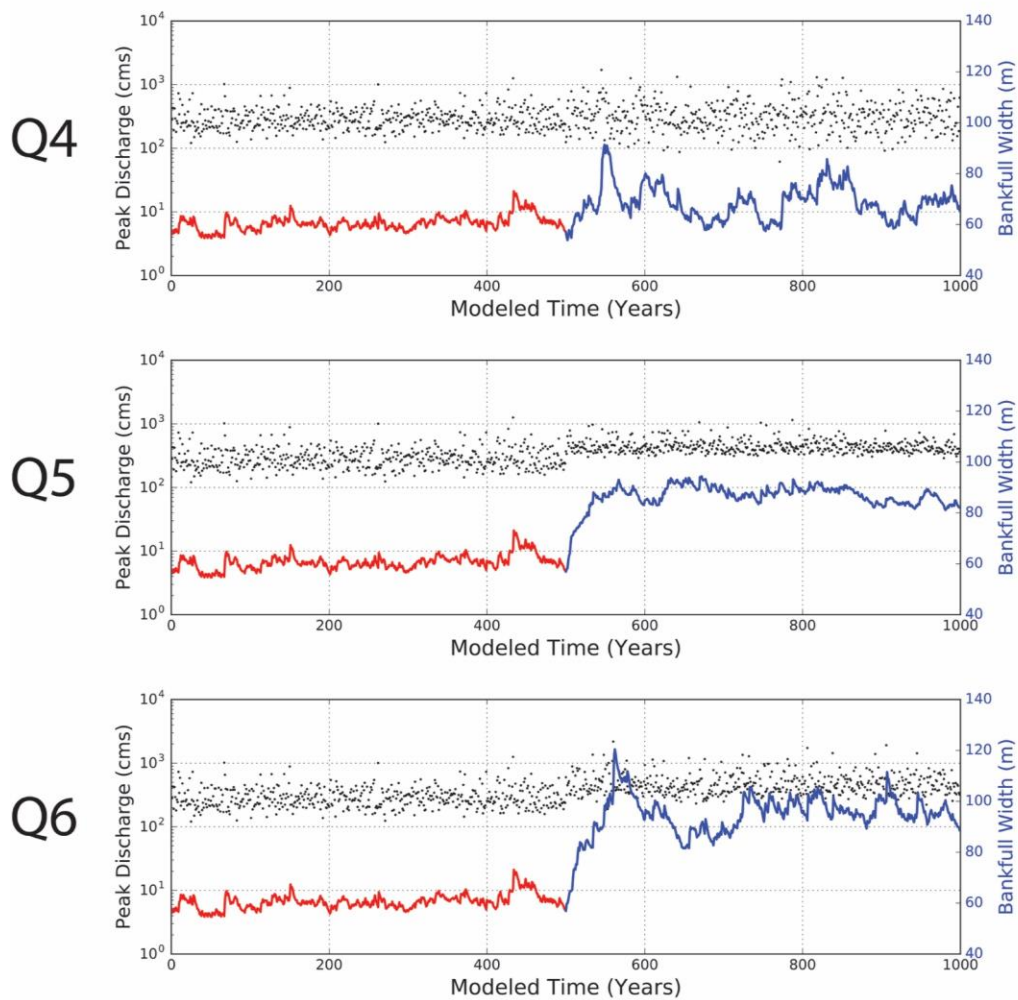
Figure 19. Example model outputs for bankfull width from flow scenarios Q4 (constant mean with increase in variance), Q5 (increase in mean with constant variance), and Q6 (increase in mean and variance).
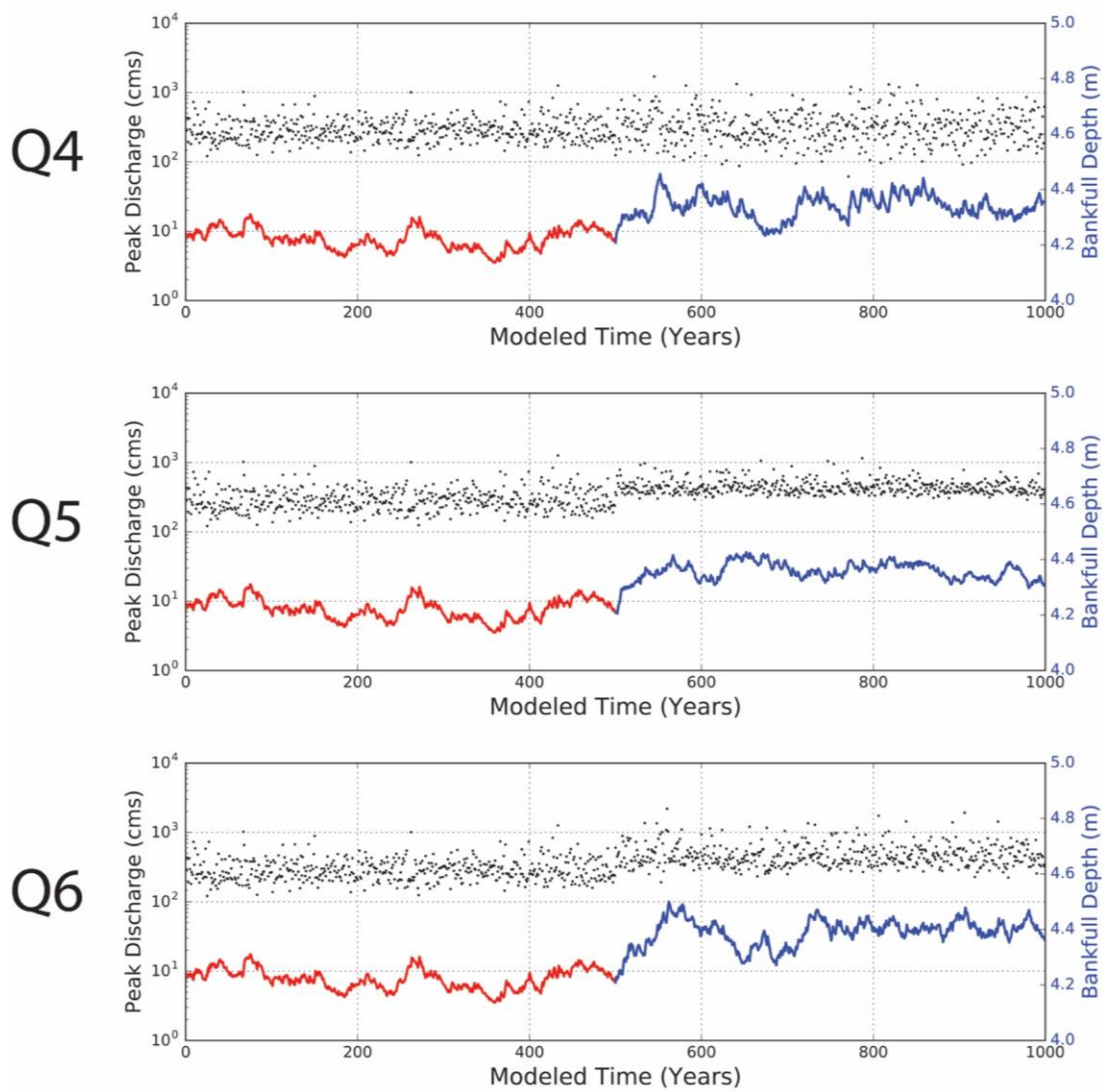
Figure 20. Example model outputs for bankfull depth from flow scenarios Q4 (constant mean with increase in variance), Q5 (increase in mean with constant variance), and Q6 (increase in mean and variance).
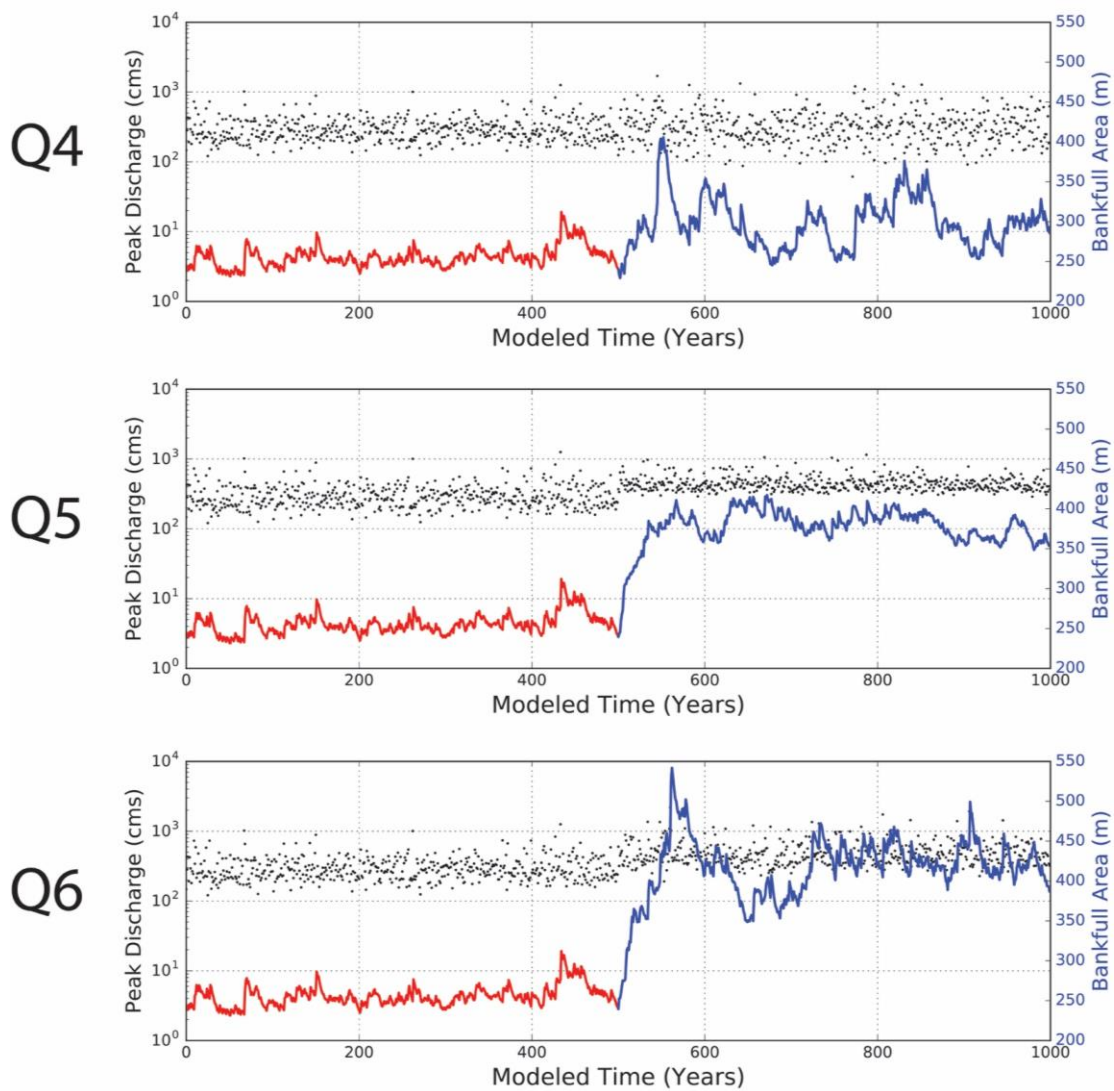
Figure 21. Example model outputs for bankfull area from flow scenarios Q4 (constant mean with increase in variance), Q5 (increase in mean with constant variance), and Q6 (increase in mean and variance).
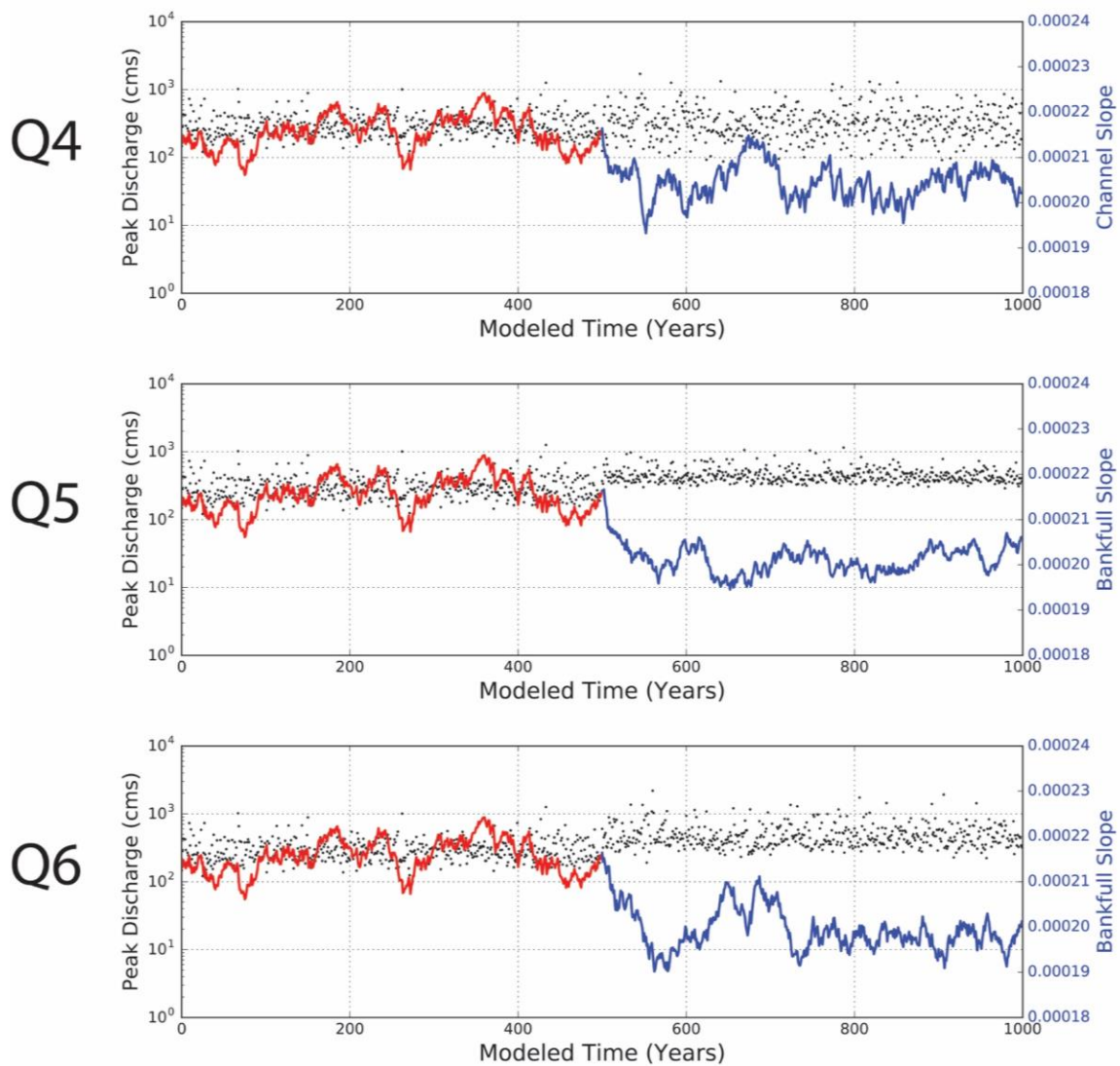
Figure 22. Example model outputs for channel slope from flow scenarios Q4 (constant mean with increase in variance), Q5 (increase in mean with constant variance), and Q6 (increase in mean and variance).
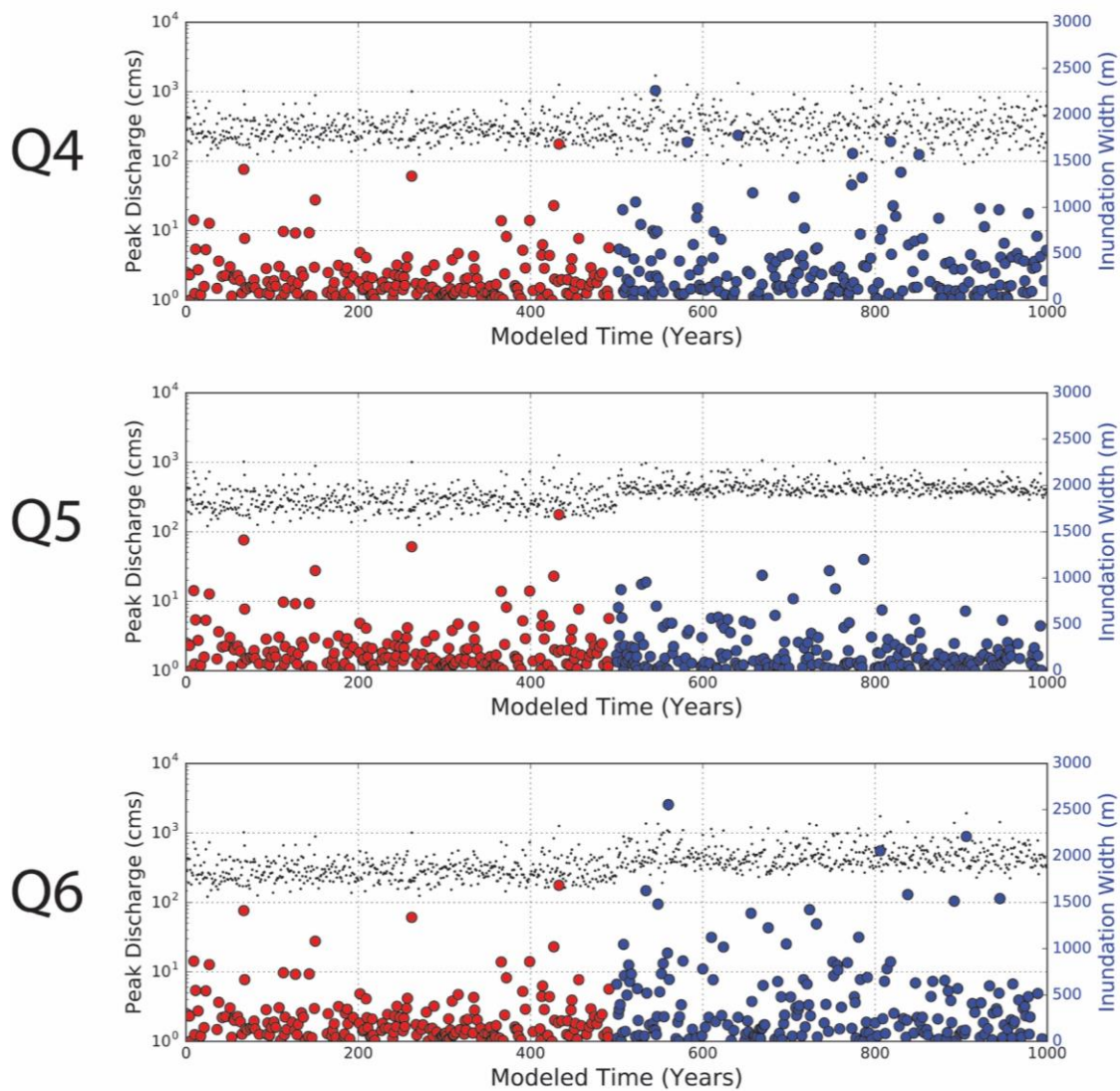
Figure 23. Example model outputs for inundation widths from flow scenarios Q4 (constant mean with increase in variance), Q5 (increase in mean with constant variance), and Q6 (increase in mean and variance).
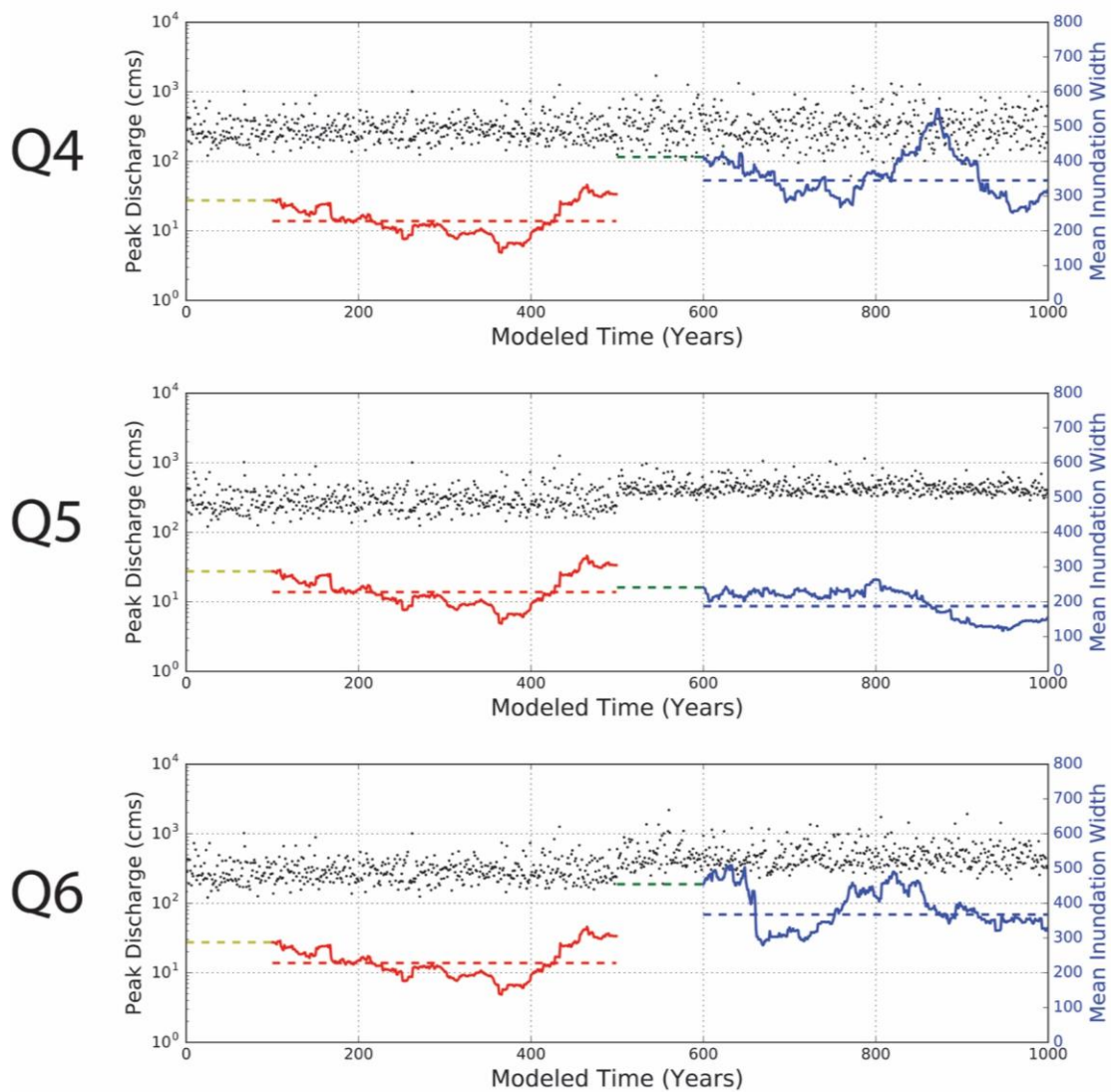
Figure 24. Example model outputs for mean inundation widths from flow scenarios Q4 (constant mean with increase in variance), Q5 (increase in mean with constant variance), and Q6 (increase in mean and variance).
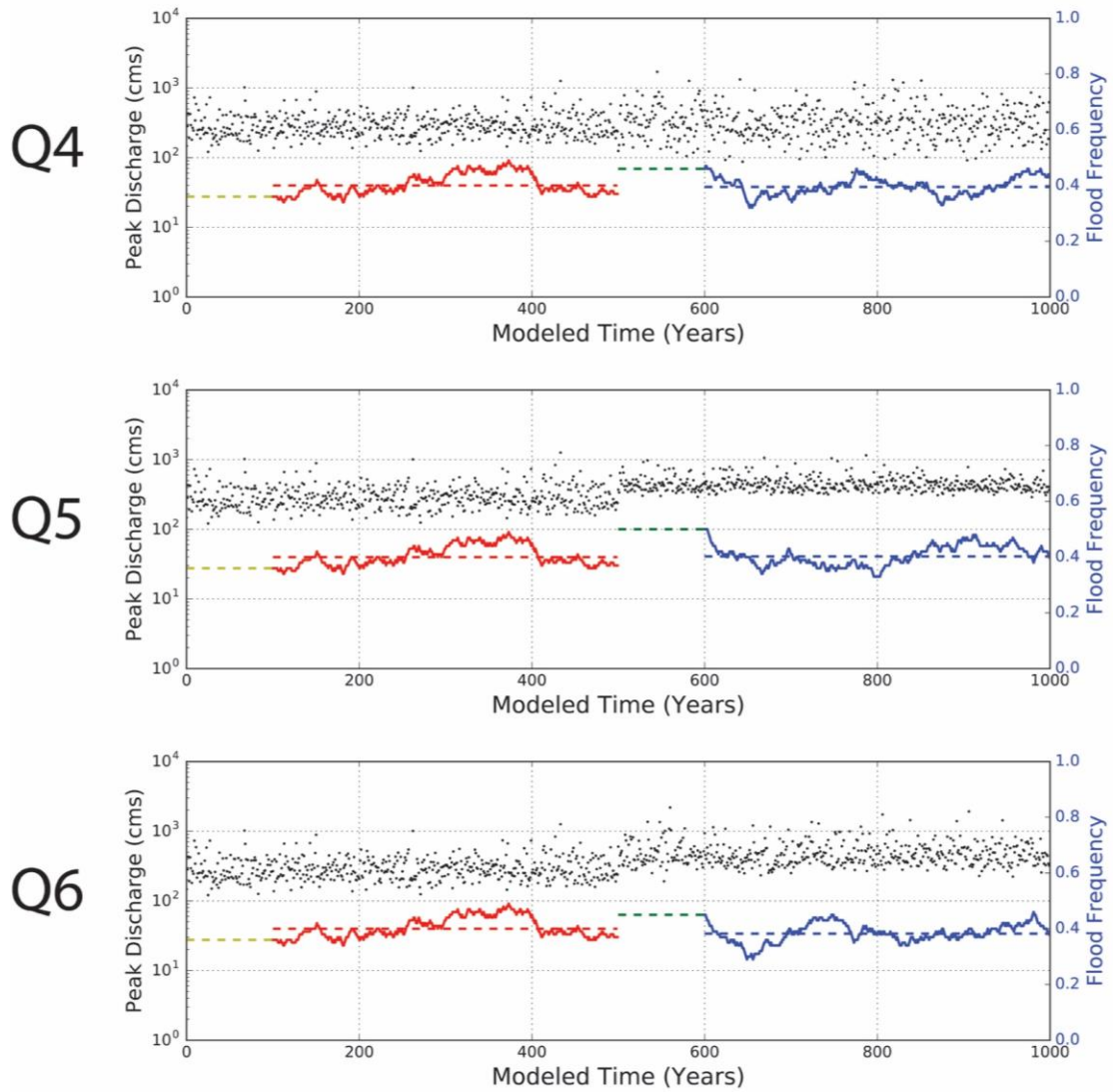
Figure 25. Example model outputs for flood frequency from flow scenarios Q4 (constant mean with increase in variance), Q5 (increase in mean with constant variance), and Q6 (increase in mean and variance).
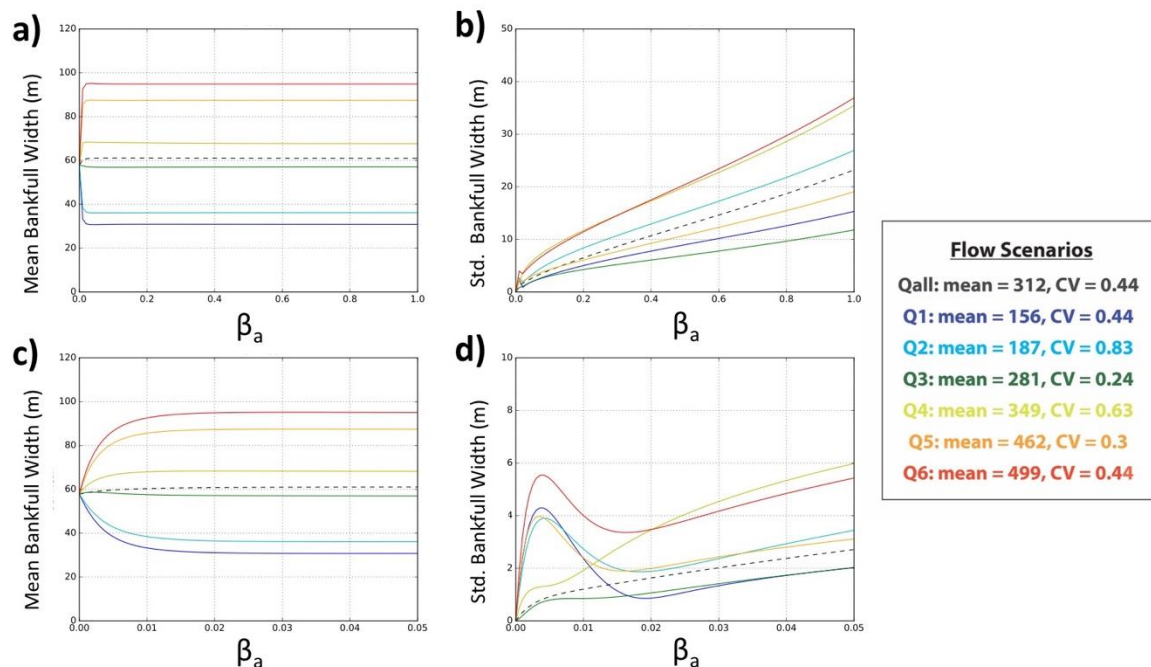
Figure 26. Results from method A analysis using sediment supply scenario S1 (dynamic sediment supply rate) showing mean and std. bankfull width for a range β_a between 0.0 and 1.0 (a and b, respectively), and mean and std. bankfull width for a range β_a between 0.0 and 0.05 (c and d, respectively).

Figure 27a shows that mean channel width is most closely related to the mean of each flow scenario (i.e., higher flows cause wider channels) and appears to scale with the magnitude of the sediment supply rate for S1 (circles), S4 (squares), and S5 (pentagons) (i.e., a higher sediment supply causes wider channels). Considering the pattern shown in Figure 27b, standard deviation of channel widths appears to scale according to the mean of each hydrologic scenario and the coefficient of variation for all flow and sediment scenarios. This pattern, along with a similar phenomenon in mean inundation widths, will be discussed in more detail below.

Both mean and standard deviation of channel depth and slope appear to be more
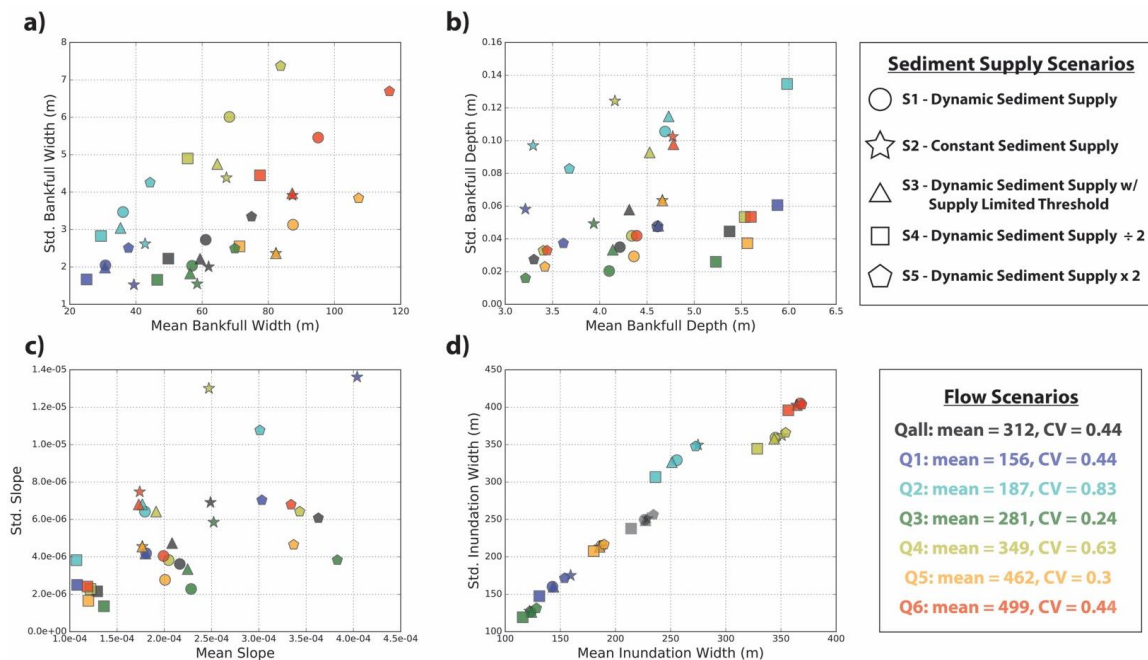
Figure 27. Results for the six flow (differentiated by color) and the five sediment supply rate scenarios (differentiated by shape) using adjustment method A where $\beta_a = 0.05$ showing relationships between: a) mean bankfull width and std. of bankfull width, b) mean bankfull depth and std. of bankfull depth, c) mean slope and std. of slope, and d), mean inundation width and. std. of inundation width.

sensitive to the magnitude of sediment supply rate than the magnitude of flows and are

inversely related to one another (i.e., higher sediment supply rates lead to smaller depths

and larger slopes while smaller sediment supply rates lead to larger depths and smaller

slopes). For example, mean depths calculated using S4, using a relatively small sediment

supply, are larger than mean depths calculated using other sediment supply scenarios.

Likewise, the range of values for the standard deviation of depth is larger than all other

sediment supply scenarios. This can be seen in Figure 27b where the mean depths for S4

(squares) are grouped together on the far right and extend across a greater portion of the

y-axis than other scenarios. Mean and standard deviation depths are consistently ordered

from smallest to largest by flow scenarios Q3, Q4, Q5, Q6, Q1, Q2, while mean slopes

are consistently ordered from smallest to largest by flow scenarios in the exact reverse

order, Q2, Q1, Q6, Q5, Q4, Q3. Conversely, values of mean slope for all flow scenarios

using S4 (the lowest sediment supply scenario) are smaller in magnitude than those

calculated with the other sediment supply scenarios, and can be seen grouped together on

the far left corner of Figure 27c with a much narrower range in the standard deviation.

The reverse trend is evident in values of mean depth and slope for all flow scenarios

calculated using the highest sediment supply scenario, S5 (pentagons).

　　　　S3 (triangles), consisting of a moderate, dynamic sediment supply that is limited

at all values above bankfull, results in mean and standard deviation depths and slopes

similar in magnitude to those of S1 (circles), but with slightly larger depths and smaller

slopes where differences increase by flow scenario (i.e., values are nearly identical for

Q1, but are much larger for Q6). S2 (stars), consisting of a constant sediment supply that

is high relative to other scenarios at low flows and low relative to other scenarios at high

flows, does not follow a pattern similar to the other scenarios, demonstrating the

importance of sediment supply in determining channel adjustment trajectory. Instead, it is

similar to the pattern seen by the standard deviation of widths where both the mean and

standard deviation depth and slope scale by the mean of each hydrologic scenario and the

coefficient of variation.

　　　　Although channel widths, depths, and slopes can diverge significantly from one

another depending on their sediment supply scenario, the resulting mean inundation

widths and flood frequencies are nearly identical across all discharge scenarios.

Furthermore, changes in inundation magnitude and frequency are only sensitive to small

values of β_a.

The mean and standard deviation of inundation widths are relatively stable when

averaged over the 400-year analysis windows, at values of β_a greater than 0.02 across all

flow and sediment scenarios. An example of this can be seen in Figure 28 showing model

results calculated using S1 across a range of values for β_a between 0.0 and 1.0 (Figures

28a and b, respectively) and a smaller range between 0.0 and 0.05 (Figures 28c and d,

respectively). Q5 has the largest change in mean inundation width between the range 0.0

and 0.2 as it decreases from 300 m to 200 m. Furthermore, mean and standard deviation
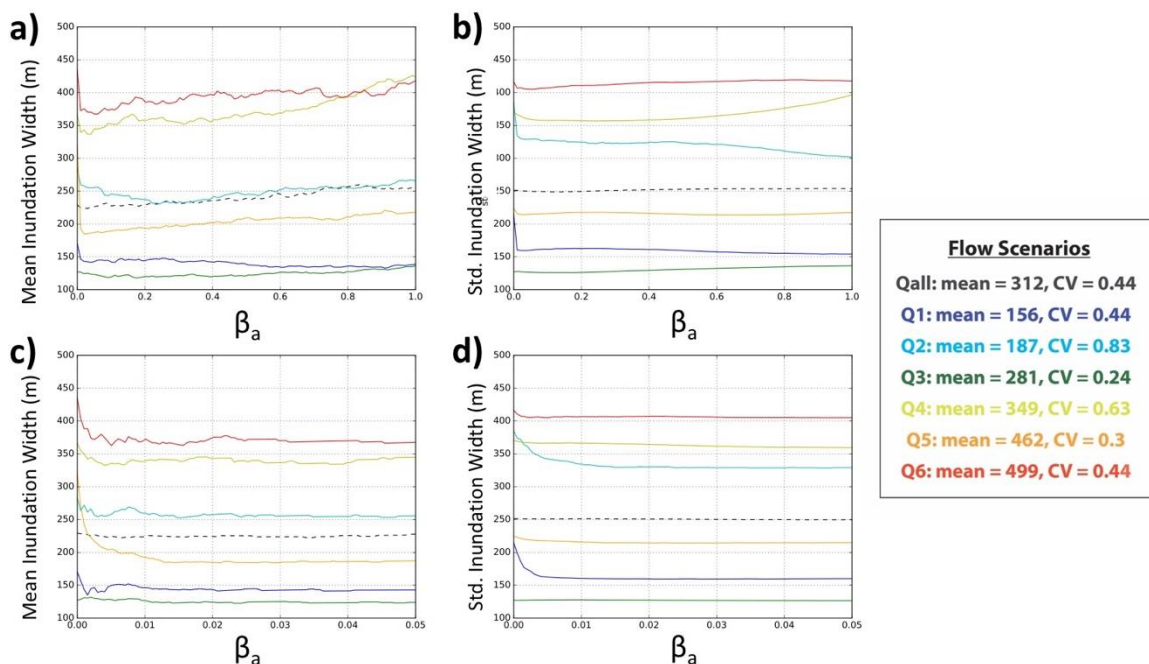
Figure 28. Results from method A using sediment supply scenario S1 (dynamic sediment supply rate) showing mean and std. inundation width for a range β_a between 0.0 and 1.0 (a and b, respectively), and mean and std. bankfull width for a range β_a between 0.0 and 0.05 (c and d, respectively).

inundation widths appear to scale uniformly (Figure 28d).

Interestingly, mean inundation widths are not simply correlated with the mean of the flow distribution; the coefficient of variation also appears to be an important influence. This can be seen in Figure 29 where the mean of each flow scenario's flood distribution is plotted against the mean inundation width for $\beta_a = 0.05$ with the corresponding coefficient of variation annotated to the top-right of each plotted point. This shows that the coefficient of variation controls how mean inundation width scales by the mean of the flood distribution. Scenarios with a coefficient of variation of 0.44 exhibit a near one-to-one correlation between the mean of their flood distributions and their mean inundation widths. However, coefficients of variation greater than 0.44
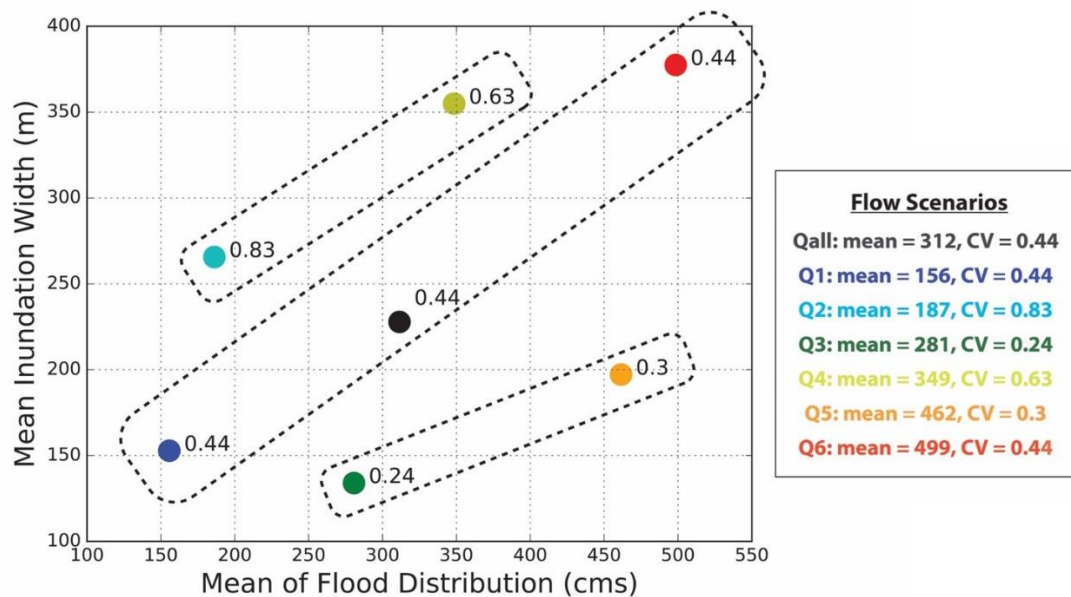
Figure 29. The mean of each flow scenario's flood distribution plotted against the resulting mean inundation width using adjustment method A where $\beta_a = 0.05$. Scenarios are plotted by color with the corresponding coefficient of variation annotated to the top-right of each data point. Scenarios are further grouped together by similar coefficients of variation (black dashed line).

increase mean inundation width relative to the mean of the flood distribution (Q2 (cyan) and Q4 (yellow)) while coefficient of variation smaller than 0.44 decrease mean inundation width relative to the mean of the flood distribution (Q3 (green) and Q5 (orange)).

The fraction of years with inundation for all flow scenarios is quite divergent for $\beta_a = 0.0$ and mostly scale according to the mean of each flow scenario (i.e., scenario 1 has the smallest mean and the smallest fraction of years with inundation). This suggests that channels with non-adjustable geometries, as is often assumed in many flood inundation studies, would see extreme changes in the frequency of floodplain inundation. As β_a approaches a value of 0.02, however, the fraction of years with inundation converge to range between 0.35 and 0.45, after which all scenarios gradually increase towards a range of 0.45 and 0.55 where $\beta_a = 1.0$. An example of this can be seen in Figure 30 showing model results calculated using S1 across a range of values for β_a between 0.0 and 1.0 (Figures 30a) and a smaller range between 0.0 and 0.05 (Figures 30b).
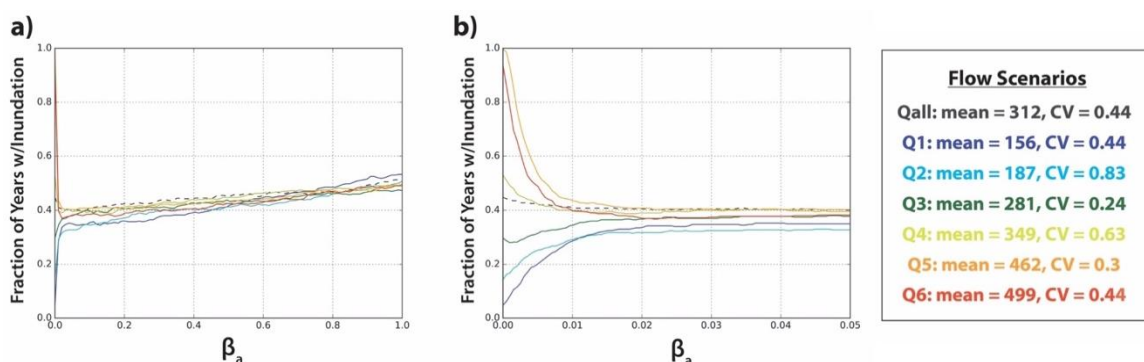
Figure 30. The fractions of years with inundation for each flow scenario plotted against adjustment parameter values using adjustment method A, where a) shows a range of β_a values between 0.0 and 1.0, and b), shows a range of β_a values between 0.0 and 0.05.

4.2.2. Methods B and C

Understanding how channel geometries change based on the two adjustment parameters used in methods B and C requires visualization of a three-dimensional solution space. This is accomplished by using three-dimensional plots with x and y-axes forming a two-dimensional array of parameter value combinations and the z-axis representing a response variable (Figure 31). When two adjustment parameters have the same value, the model functions identically to Method A. This allows us to conceptualize how methods B and C relate to results from Method A based on the divergence of the two adjustment parameters from a one-to-one ratio.

Figure 32 shows a characteristic solution space for mean and standard deviation widths, which should be noted, is identical irrespective of method B or C being used
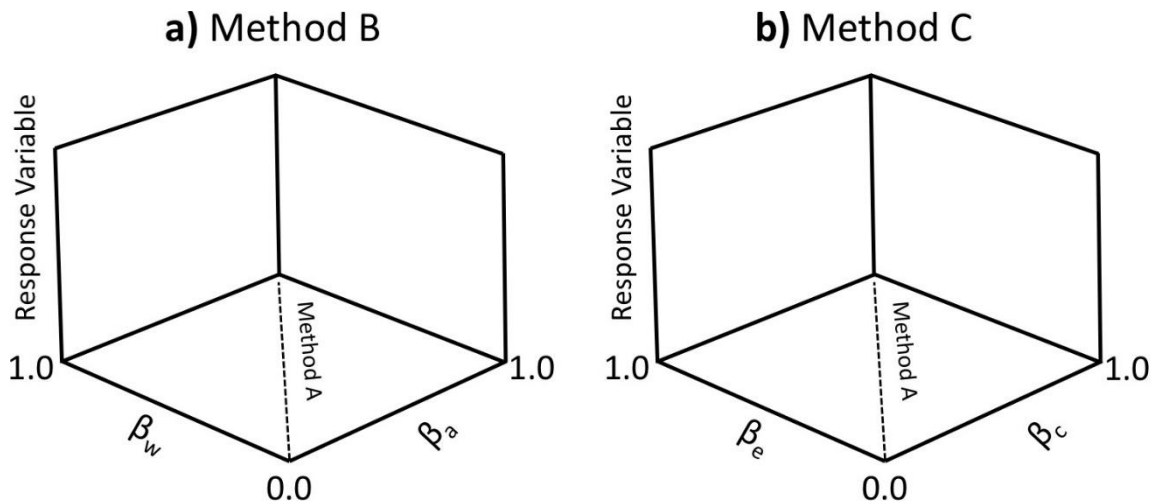
Figure 31. Diagram illustrating how to visualize 3D plots of: a) method B's solution space relative to adjustment parameters β_w and β_a , and b) method C's solution space relative to adjustment parameters β_e and β_c. The dashed line shows the location of the one-dimensional solution space for method A relative to methods B and C's three-dimensional solution space. The z-axis is the response variable.

since the scheme for width adjustment is practically identical for both even though

different parameters are used (i.e., β_w and β_e both control the rate of widening while β_a

and β_c both control the rate of narrowing). Depths and slopes, however, can differ

significantly between methods B and C. Figure 33 shows a characteristic solution space

for mean and standard deviation depths and Figure 34 shows a characteristic solution

space for mean and standard deviation slopes. When there is a one-to-one correspondence

between β_w and β_a or β_e and β_c, mean channel geometries are identical to those in

method A that converge to an equilibrium value around $\beta_a = 0.03$. In Method B, these

equilibrium values remain constant through $\beta_a = 1.0$ for mean depth and slope. In

Method C, mean width, depth, and slope vary non-linearly away from Method A's

equilibrium values depending on the relative ratio of the two adjustment parameters. For

example, if the ratio of β_w / β_a or β_e / β_c is greater than one, the geometries mean will
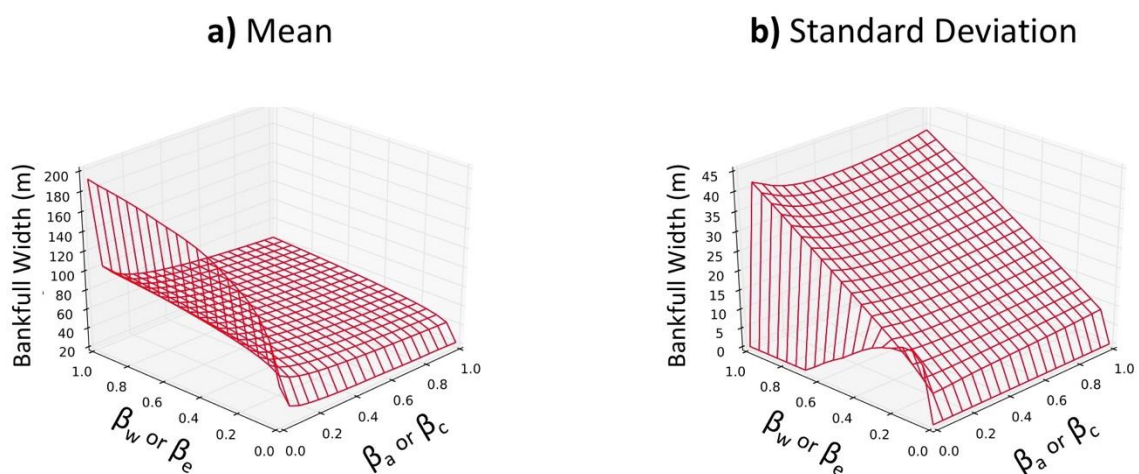
Figure 32. Solution space for mean bankfull width (a) and standard deviation of bankfull width (b) relative to different adjustment parameter combinations for methods B (using β_w and β_a) and C (using β_e and β_c). Results are for years 0-500 in all flow scenarios utilizing S1 (dynamic sediment supply rate).
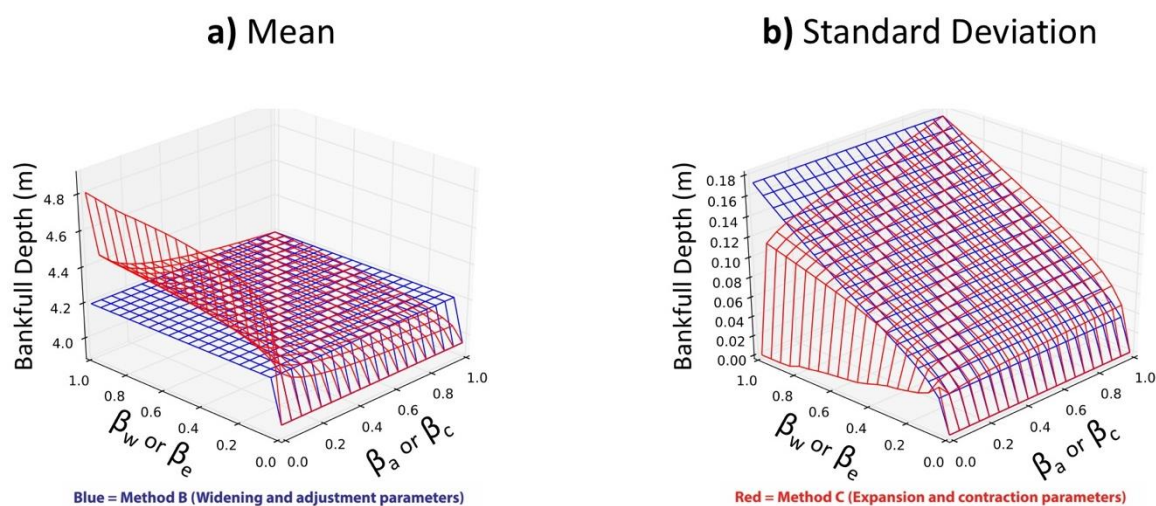
Figure 33. Solution space for mean bankfull depth (a) and standard deviation of bankfull depth (b) relative to different adjustment parameter combinations for methods B (plotted in blue; using β_w and β_a) and C (plotted in red; using β_e and β_c). Results are for years 0-500 in all flow scenarios utilizing S1 (dynamic sediment supply rate).
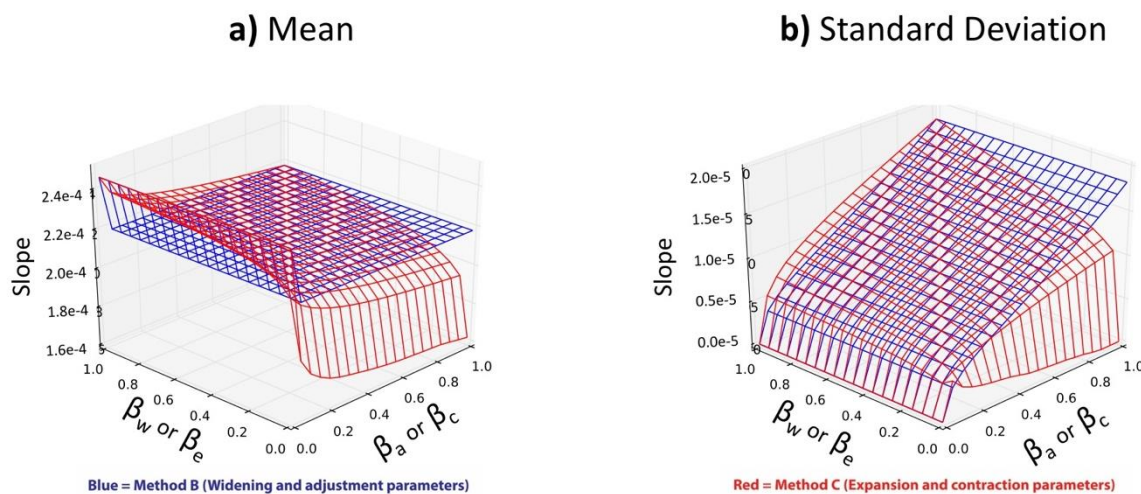
Figure 34. Solution space for mean slope (a) and standard deviation of slope (b) relative to different adjustment parameter combinations for methods B (plotted in blue; β_w and β_a) and C (plotted in red; β_e and β_c). Results are for years 0-500 in all flow scenarios utilizing S1 (dynamic sediment supply rate).

increase non-linearly. On the other hand, if the ratio of β_w / β_a or β_e / β_c is less than

one, the geometries mean will decrease non-linearly.

Figure 35 shows a characteristic solution space for mean and standard deviation

inundation widths. Mean inundation widths in methods B and C scale similar to those in

Method A and are sensitive near adjustment parameter values between 0.0 and 0.01 with

different trajectories of change depending on the ratio of the two adjustment parameters.

For example, the larger the widening or expansion parameter is relative to the adjustment

or contraction parameter, mean inundation widths will decrease rapidly around this

sensitive range of values and vice versa. Mean and standard deviation inundation widths

between methods B and C are relatively similar when the ratio of adjustment parameters

is close to one, but diverge away from it. For example, mean inundation widths are

approximately 100 m greater for method C when either β_a or β_c is significantly greater
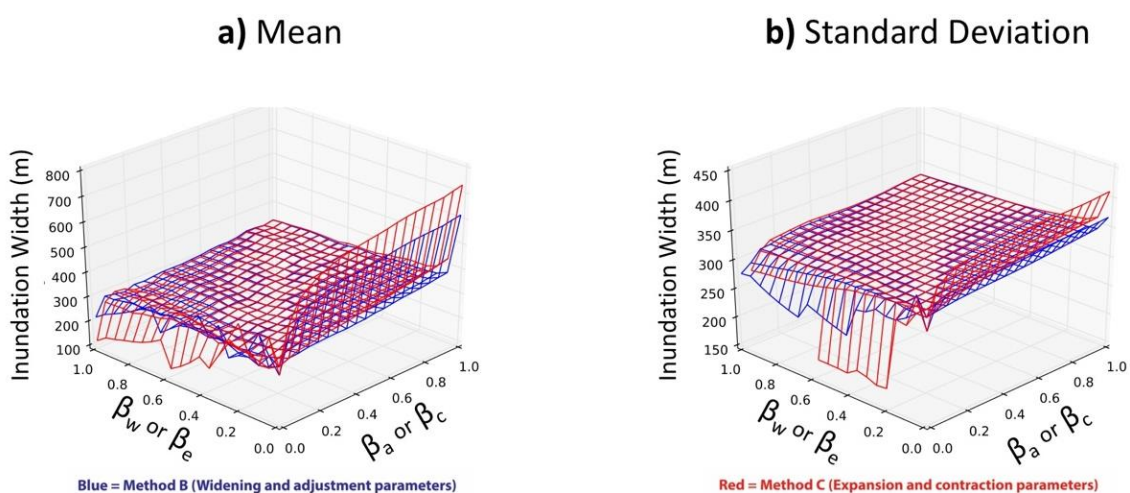
Figure 35. Solution space for mean inundation width (a) and standard deviation of inundation width (b) relative to different adjustment parameter combinations for methods B (plotted in blue; using β_w and β_a) and C (plotted in red; using β_e and β_c). Results are for years 0-500 in all flow scenarios utilizing S1 (dynamic sediment supply rate).

than β_w or β_e. This is due to a larger amount of channel contraction occurring in Method

C, which constricts channel capacity more than Method B.

Figure 36 shows a characteristic solution space for fraction of years with

inundation and shows that flood frequency is highly sensitive to the ratio of the two

adjustment parameters. For example, the larger the widening or expansion parameter is

relative to the adjustment or contraction parameter, the smaller the fraction of years with

inundation will be. Conversely, the smaller the widening or expansion parameter is

relative to the adjustment or contraction parameter, the greater the fraction of years with

inundation will be. Channel depths and slopes are always larger or smaller with Method

C than those predicted with similar parameters using methods A and B due to preferential

adjustment that depends on whether expansion or contraction is predicted for a particular

geometry. For example, consider a channel that can contract more easily than it can
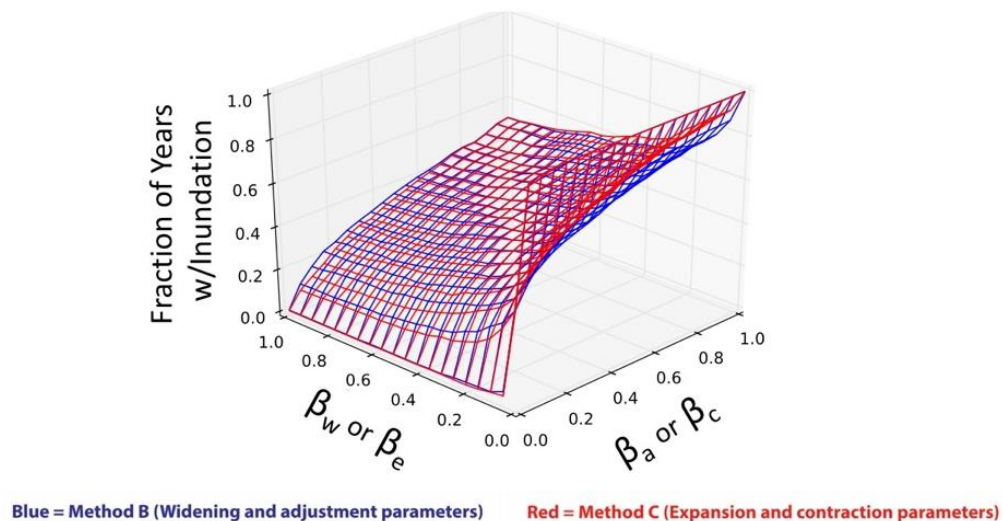
Figure 36. Solution space for the fraction of years with inundation (flood frequency) relative to different adjustment parameter combinations for methods B (plotted in blue; using β_w and β_a) and C (plotted in red; using β_e and β_c). Results are for years 0-500 in all flow scenarios utilizing S1 (dynamic sediment supply rate).

expand. If an identical pair of adjustment parameters are specified for a given model

scenario, runs using Method C will systematically produce slightly larger mean

inundation widths and flood frequencies than method B. This is due to Method C

producing overall smaller channel capacities due to higher rates of aggradation and slope

reduction relative to Method B's equal rates of depth and slope adjustment. Conversely,

Method C would produce slightly smaller mean inundation widths and flood frequencies

than Method B if the same model runs were specified with a channel that can expand

more easily than it can contract due to Method C producing channel capacities that are

overall smaller than Method B.

4.3. Discussion

The influence of channel behavior and flood inundation between adjustment

methods and different combinations of adjustment parameters can be conceptually

summarized by two example model runs with deliberately chosen differences in

adjustment parameters. Figures 37 depicts a channel that can widen or expand much more

easily than it can narrow or contract (β_w and $\beta_e = 0.1$, β_a and $\beta_c = 0.01$). Conversely,

Figure 38 depicts a channel that can narrow or contract much more easily than it can

widen or expand (β_w and $\beta_e = 0.01$, β_a and $\beta_c = 0.1$). Methods A, B, and C are plotted

by color (blue, red, and green, respectively) for width (a), depth (b), area (c), and slope

(d) as well as one-hundred year running averages for mean inundation width (e) and flood

frequency (f).

Mean inundation width is relatively insensitive to the adjustment parameter.

Figure 37e shows that mean inundation widths are relatively similar across methods A, B,

and C when the channel can expand more easily than contract, while Figure 38e shows slightly greater variability between them when the channel can contract more easily than it can expand. The more significant control on mean inundation width appears to be the flood distribution's coefficient of variation, which controls how the mean inundation width scales with the flood distribution's mean and can lead to counterintuitive results. For example, increasing mean peak discharge was shown to produce a decrease in mean inundation width in Q5, for which the coefficient of variation was reduced. Conversely, decreasing the mean peak discharge while increasing the coefficient of variation was shown to produce an increase in mean inundation width for Q2 (Figure 29). Flood frequencies are largely dependent on the ability of the channel to expand or contract depending on the trajectory of change in the flow regime. Figure 37e shows that channels that can more easily expand towards their long-term equilibrium form due to low bank strength have lower flood frequencies while channel that can more easily contract due to high bank strength have much higher flood frequencies. In the former example, Method C has slightly lower flood frequencies than method B, and in the latter example, slightly higher flood frequencies.
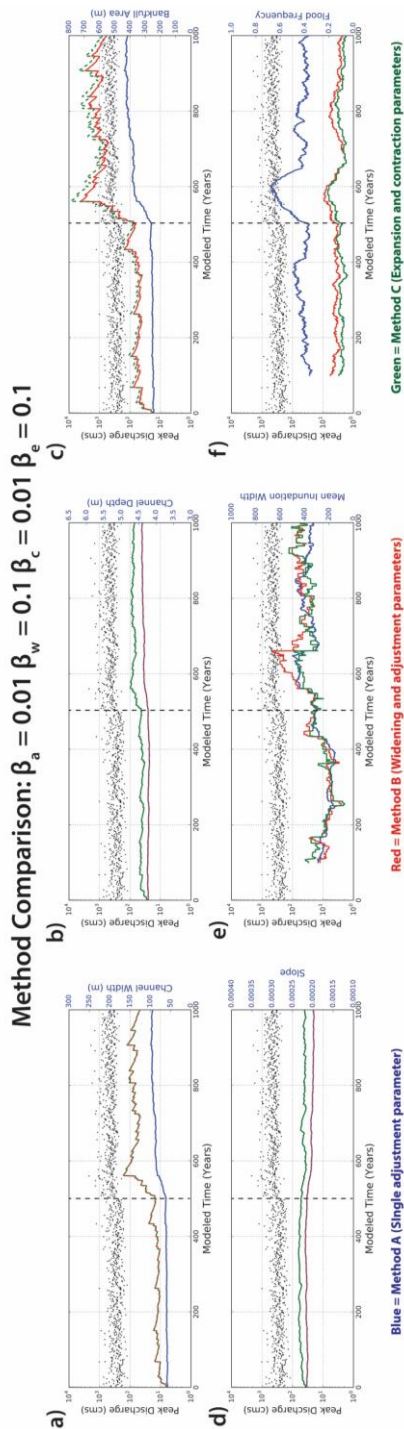
Figure 37. Model output plots of width (a), depth (b), area (c), slope (d), mean inundation width (e), and flood frequency (f) using Q6 (increase in mean and variance of peak flows) and S1 (dynamic sediment scenario) to illustrate differences between methods A, B, and C using a pair of adjustment parameter values that simulate a channel that can expand more easily than it can contract.
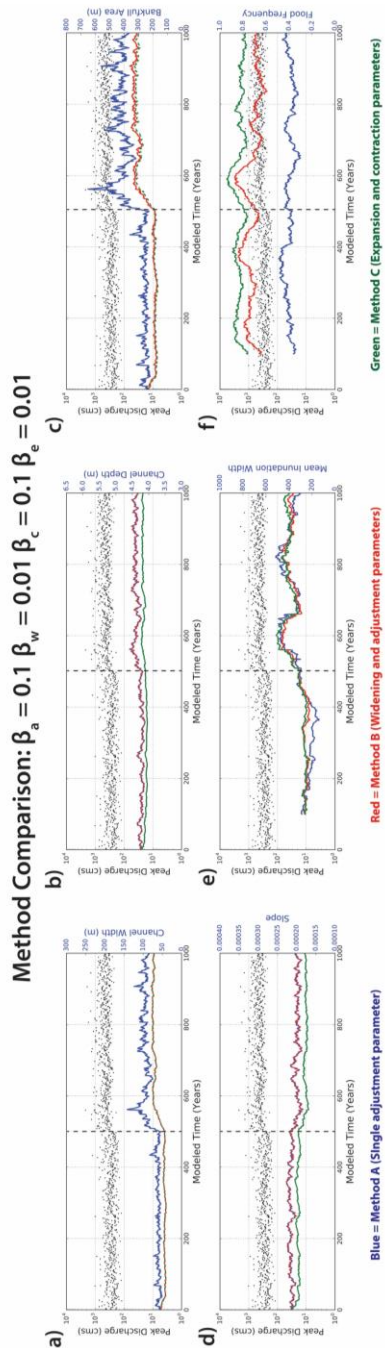
Figure 38. Model output plots of width (a), depth (b), area (c), slope (d), mean inundation width (e), and flood frequency (f) using Q6 (increase in mean and variance of peak flows) and S1 (dynamic sediment scenario) to illustrate differences between methods A, B, and C using a pair of adjustment parameter values that simulate a channel that can contract more easily than it can expand.

CHAPTER 5

SUMMARY

We developed, empirically tested, and applied a reduced complexity model to a variety of hypothetical water and sediment scenarios to explore the influence of non-stationary hydrology and channel adjustment on floodplain inundation. The model's use of hydraulic geometry relations and a specified adjustment parameter were found to be reasonable through comparison with repeat measurements of channel geometry. Further, the changes in mean and standard deviation of flood frequency PDFs in our hypothetical scenarios were consistent with shifts that have been observed in the upper Midwest over the past 3 decades. Through the utilization of an ensemble of hypothetical flow and sediment scenarios, we are able to examine how changes in the magnitude and/or variability of peak flows and commensurate adjustments in channel geometry can alter the frequency and magnitude of floodplain inundation.

Results suggest that systematic shifts in peak flows cannot be translated directly to changes in the frequency or magnitude of floodplain inundation due to the non-linear factors controlling changes in channel capacity. Results suggest that the frequency of floodplain inundation is primarily dependent on the relative rate and trajectory of channel adjustment towards an equilibrium geometry, as dictated by the mean and standard deviation of peak flows. Long-term changes in the frequency of floodplain inundation under non-stationary hydrology occur when a relatively slow rate of adjustment prevents the channel from quickly or fully adjusting to a new equilibrium geometry. For example, an increase in the mean of peak flows would likely result in more frequent inundation

over a relatively short period of adjustment as the channel expands by small fractions each year towards a new long-term equilibrium geometry. However, this may not necessarily cause a long-term increase in the frequency of floodplain inundation if the channel is able to adjust relatively quickly towards the new equilibrium geometry, as defined by the mean and standard deviation of the new hydrologic regime. Conversely, a decrease in the mean of peak flows would likely result in less frequent inundation over a relatively short period of adjustment as the channel contracts by small fractions each year towards a new long-term equilibrium geometry. However, this may not necessarily cause a long-term decrease in the frequency of floodplain inundation if the channel is able to adjust relatively quickly towards the new equilibrium geometry.

Analyzed flow records for stream gages in the upper Midwest show that flow regimes are systematically changing. While the majority of analyzed gage records show that the mean and standard deviation of their flood distributions have increased since 1980, their coefficients of variation (standard deviation divided by mean) have decreased, suggesting that increases in the standard deviation are not scaling proportionally with changes in the mean. Such observations may potentially be significant in understanding changes in the average areal extent of flood inundation as model results suggest that the most significant control on the mean horizontal width of floodplain inundation appears to be the flood distribution's coefficient of variation instead of simple changes in the mean of the peak flow distribution. Furthermore, changes in the mean that alter the coefficient of variation of peak flows can lead to counterintuitive results. For example, model results show that simply increasing the mean of peak discharges while preserving the standard

deviation resulted in a decrease in mean inundation widths because the coefficient of variation was simultaneously reduced. Conversely, model results also show that simply decreasing the mean of peak discharges while preserving the standard deviation resulted in an increase in mean inundation widths because the coefficient of variation was simultaneously increased. Model results further suggest that the horizontal width of floodplain inundation is not strongly influenced by the rate and trajectory of channel adjustment.

The modeling framework presented in this paper could be extended to address other questions related to fluvial geomorphology and landscape evolution such as 1) a more thorough definition of adjustment parameters, constraining their physical basis, and formulating a way to account for the influence of flow duration, threshold exceedance events, feedback mechanisms, and changes in grain-size distributions, 2) potential modification of predictions from the *Li et al.* [2015] hydraulic geometry relations to simulate the preferential adjustments in depth seen in the non-fully alluvial knick zone environment of the Le Sueur and Maple rivers, 3) modeling more complex changes in PDFs, including more gradual transitions as well as cyclical changes in parameters over time, and 4) including more process-based methods to constrain the potential amount of adjustment possible within a given time-step, such as a numerical scheme of the Exner equation to model bed elevation adjustments and floodplain deposition along multiple reach-averaged cross-sections within a river basin.

REFERENCES

Allred, T. W., and J. C. Schmidt (1999), Channel narrowing by vertical accretion along the Green River near Green River, UT, *Geol. Soc. Am. Bull.*, *111*(12), 1757–1772, doi: 10.1130/0016-7606(1999)111<1757:CNBVAA>2.3.CO;2.

Belmont, P. (2011), Floodplain width adjustments in response to rapid base level fall and knickpoint migration, *Geomorphology*, *128*, 92–101, doi: 10.1016/j.geomorph.2010.12.026.

Belmont, P., K. B. Gran, S. P. Schottler, P. R. Wilcock, S. S. Day, C. Jennings, J. W. Lauer, E. Viparelli, J. K. Willenbring, D. R. Engstrom, and G. Parker (2011), Large shift in source of fine sediment in the Upper Mississippi River, *Environ. Sci. Technol.*, *45*(20), 8804-8810, doi: 10.1021/es2019109.

Burkham, D. (1972), Channel changes of the Gila River in Safford valley, Arizona, 1846-1970, *U.S. Geol. Surv. Prof. Pap.*, *655-G*, 24 p.

Charlson, R. J., S. E. Schwartz, J. M. Hales, R. D. Cess, J. E. Hansen, and D. J. Hofmann (1992), Climate forcing by anthropogenic aerosols, *Science*, *255*(5043), 423-430, doi: 10.1126/science.255.5043.423.

Collins, M., R. Knutti, J. Arblaster, J. L. Dufresne, T. Fichefet, P. Friedlingstein, X. Gao, W. J. Gutowski, T. Johns, G. Krinner, M. Shongwe, C. Tebaldi, A. J. Weaver, and M. Wehner, 2013, Long-term Climate Change: Projections, Commitments and Irreversibility, in *Climate Change 2013: The Physical Science Basis. Contribution of Working Group I to the Fifth Assessment Report of the Intergovernmental Panel on Climate Change* Stocker, edited by T. F. Stocker, D. Qin, G. K. Plattner, M. Tignor, S. K. Allen, J. Boschung, A. Nauels, Y. Xia, V. Bex and P. M. Midgley, pp. 1029–1136, Cambridge University Press, Cambridge, United Kingdom and New York, NY, USA, doi:10.1017/CBO9781107415324.024.

Cox, P. M., R. A. Betts, C. D. Jones, S. A. Spall, and I. J. Totterdell (2000), Acceleration of global warming due to carbon-cycle feedbacks in a coupled climate model, *Nature, 408*(6809), 184-187, doi:10.1038/35041539.

Dean, D. J., and J. C. Schmidt (2011), The role of feedback mechanisms in historic channel changes of the lower Rio Grande in the Big Bend region, *Geomorphology*, *126*, 333–349, doi: 10.1016/j.geomorph.2010.03.009.

Dean, D. J., and J. C. Schmidt (2013), The geomorphic effectiveness of a large flood on the Rio Grande in the Big Bend region: Insights on geomorphic controls and post-

flood geomorphic response, *Geomorphology*, *201*, 183–198, doi: 10.1016/j.geomorph.2013.06.020.

Everitt, B. (1993), Channel responses to declining flow on the Rio Grande between Ft. Quitman and Presidio, Texas, *Geomorphology*, *6*, 225–242, doi: 10.1016/0169-555X(93)90048-7.

Friedman, J. M., W. R. Osterkamp, M. L. Scott, and G. T. Auble (1998), Downstream effects of dams on channel geometry and bottomland vegetation: Regional patterns in the great plains, *Wetlands*, *18*(4), 619–633, doi: 10.1007/BF03161677.

Foufoula-Georgiou, E., Z. Takbiri, J. A. Czuba, and J. Schwenk, (2015), The change of nature and the nature of change in agricultural landscapes: Hydrologic regime shifts modulate ecological transitions, *Water Resour. Res.*, *51*(8), 6649-6671.

Gleason, C. J. (2015), Hydraulic geometry of natural rivers: A review and future directions, *Prog. in Phys. Geogr.*, *39*(3), doi:10.1177/0309133314567584.

Gran, K. B., P. Belmont, S. S. Day, N. Finnegan, C. Jennings, J. W. Lauer, and P. R. Wilcock (2011), Landscape evolution in south-central Minnesota and the role of geomorphic history on modern erosional processes, *GSA Today*, 21(9), 7–9, doi:10.1130/G121A.1.

Gran, K. B., N. Finnegan, A. L. Johnson, P. Belmont, C. Wittkop, and T. Rittenour (2013), Landscape evolution, valley excavation, and terrace development following abrupt postglacial base-level fall, *Geol. Soc. Am. Bull.*, *125*(11-12), 1851-1864.

Hack, J. T. (1960), Interpretation of erosional topography in humid temperate regions, *Am. J. Sci.*, *258*(A), 80–97.

Rao, A. R., and K. Hamed (1999), *Flood frequency analysis*, CRC press, Bocca Raton, Florida.

Interagency Advisory Committee on Water Data (IACWD) (1982), Guidelines for determining flood flow frequency: Bulletin 17-B, Hydrol. Subcomm., Off. Water Data Coord., U.S. Geol. Surv., Reston, Virginia, pp. 183.

James, L.A., and S. A. Lecce (2013), Impacts of land-use and land-cover change on river systems, in *Treatise on Geomorphology*, edited by E. Wohl, vol. 9, pp. 768–793, Academic Press, San Diego, California, doi: 10.1016/B978-0-12-374739-6.00264-5.

Junk, W. J., P. B. Bayley, and R. E. Sparks (1989), The flood pulse concept in river-floodplain systems, *Canadian special publication of fisheries and aquatic sciences*, *106*, 110–127.

Kasprak, A. (2015), Linking form and process in braided rivers using physical and numerical models, Ph.D dissertation, Dept. of Watershed Science, Utah State Univ, Logan, Utah.

Kelly, S., Z. Takbiri, P. Belmont, E. Foufoula-Georgiou (in review), Human amplified changes in precipitation-runoff patterns in large river basins of the Midwestern United States. Submitted to *Hydrol. Earth. Syst. Sc.*

Kundzewicz, Z. W., S. Kanae, S. I. Seneviratne, J. Handmer, N. Nicholls, P. Peduzzi, R. Mechler, L. M. Bouwer, N. Arnell, K. Mach, and R.Muir-Wood (2014), Flood risk and climate change: global and regional perspectives, *Hydrol. Sci. J.*, *59*(1), 1–28, doi: 10.1080/02626667.2013.857411.

Lane, E. W. (1955), The Importance of Fluvial Morphology in Hydraulic Engineering, *American Society of Civil Engineers Proceedings Separate, 81*(745), 1–17.

Lane, S. N. (2013), 21st century climate change: where has all the geomorphology gone?, *Earth Surf. Process. Landf.*, *38*(1), 106-110, doi: 10.1002/esp.3362.

Leopold, L. B., and T. Maddock Jr. (1953), The hydraulic geometry of stream channels and some physiographic implications, *U.S. Geol. Surv. Prof. Pap.*, 252, 57 p.

Li, C. (2014), Modeling the transport of sand and mud in the Minnesota River, M.S. thesis, Civil Engineering in the Graduate College, Univ. of Illinois at Urbana-Champaign, Urbana, Illinois

Li, C., M. J. Czapiga, E. C. Eke, E. Viparelli, and G. Parker (2015), Variable Shields number model for river bankfull geometry: bankfull shear velocity is viscosity-dependent but grain size-independent, *J. Hydraul. Res*., 53(1), 36-48, doi:10.1080/00221686.2014.939113.

Lotsari, E., V. Thorndycraft, and P. Alho (2015), Prospects and challenges of simulating river channel response to future climate change, *Prog. in Phys. Geogr.*, *39*(4), 483-513, doi: 10.1177/0309133315578944.

Milly, P. C. D., J. Betancourt, M. Falkenmark, R. M. Hirsch, Z. W. Kundzewicz, D. P. Lettenmaier, and R. J. Stouffer (2008), Stationarity is dead: whither water management? *Science*, *319*, 573–574, doi: 10.1126/science.1151915.

Markus, H. D. (2011), Aquatic Life Water Quality Standards Draft Technical Support Document for Total Suspended Solids (Turbidity), *2011 Triennial Water Quality Standard Amendments to Minn. R. chs. 7050 and 7052*, Minnesota Pollution Control Agency, Saint Paul, Minnesota.

Nilsson, C., C. A. Reidy, M. Dynesius, and C. Revenga (2005), Fragmentation and Flow Regulation of the World's Large River Systems, *Science*, *308*, 405–408, doi: 10.1126/science.1107887.

Olsen, J. R. (2006), Climate change and floodplain management in the United States, *Clim. Change*, *76*(407), 407–426, 10.1007/s10584-005-9020-3.

Parker, G. (1978a). Self-formed straight rivers with equilibrium banks and mobile bed. Part 1. The sand-silt river, *J. Fluid Mech.*, *89*(1), 109-125.

Parker, G. (1978b). Self-formed straight rivers with equilibrium banks and mobile bed. Part 2. The gravel river, *J. Fluid Mech.*, *89*(1), 127-146.

Parker, G., P. R. Wilcock, C. Paola, W. E. Dietrich, and J. Pitlick (2007), Physical basis for quasi-universal relations describing bankfull hydraulic geometry of single-thread gravel bed rivers, *J. Geophys. Res. Earth Surf.*, *112*(F4), 1–21, doi: 10.1029/2006JF000549.

Pizzuto, J. E. (1994), Channel adjustments to changing discharges, Powder River, Montana, *Geol. Soc. Am. Bull.*, *106*(11), 1494–1501, doi: 10.1130/0016-7606(1994)106<1494:CATCDP>2.3.CO;2.

Schottler, S.P., J. Ulrich, P. Belmont, R. Moore, J. Lauer, D. R. Engstrom, and J. E. Almendinger (2014), Twentieth century agricultural drainage creates more erosive rivers, *Hydrol. Process.*, *28*(4), 1951-1961, doi:10.1002/hyp.9738.

Schumm, S. A., and R. W. Lichty(1965), Time, space, and causality in geomorphology, *American Journal of Science*, 263(2), 110-119.

Schumm, S. and Lichty, R. (1963), Channel widening and flood-plain construction along Cimarron River in southwestern Kansas, *Geol. Surv. Prof. Pap. 352-D*, 88 p.

Slater, L. J., M. B. Singer, and J. W. Kirchner (2015), Hydrologic versus geomorphic drivers of trends in flood hazards, *Geophys. Res. Lett.*, *42*(2), 370–376, doi: 10.1002/2014GL062482.

Tockner, K., F. Malard, and J. V. Ward (2000), An extension of the Flood pulse concept, *Hydrol. Process.*, *14*(16-17), 2861–2883, doi: 10.1002/1099-1085(200011/12)14:16/17<2861::AID-HYP124>3.0.CO;2-F.

Vörösmarty, C., D. Lettenmaier, C. Leveque, M. Meybeck, C. Pahl-Wostl, J. Alcamo, W. Cosgrove, H. Grassl, H. Hoff, P. Kabat, and F. Lansigan (2004), Humans transforming the global water system, *Eos. Trans. AGU*, *85*(48), 509-514, doi: 10.1029/2004EO480001.

Wilkerson, G. V., and G. Parker (2011), Physical Basis for Quasi-Universal Relationships Describing Bankfull Hydraulic Geometry of Sand-Bed Rivers, *J. Hydraul. Eng.* 137, 739–753, doi: 10.1061/(ASCE)HY.1943-7900.0000352.

Wolman, M. G., and R. Gerson (1978), Relative scales of time and effectiveness of climate in watershed geomorphology, *Earth Surf. Process.*, *3*(2), 189–208, doi: 10.1002/esp.3290030207.

Wolman, M. G., and J. P. Miller (1960), Magnitude and Frequency of Forces in Geomorphic Processes, *J. Geol.*, *68*(1), 54–74.

Yu, B., and M. G. Wolman (1987), Some Dynamic Aspects of River Geometry, *Water Resour. Res.*, *23*(3), 501-509, doi: 10.1029/WR023i003p00501.

APPENDICES

APPENDIX A. SUPPORTING FIGURES

Model Algorithm

Variables

B_{bf} = Bankfull Width (m)
B_f = Floodplain Inundation Width (m)
B_{pred} = Predicted Bankfull Width (m)
D = Characteristic Grain Size (m)
Cz = Chezy Friction Coefficient
Cz_f = Floodplain Chezy Friction Coefficient
H_{bf} = Bankfull Depth (m)
H_{ch} = Channel Depth (m)
H_e = Extra Channel Depth above bankfull (m)
H_f = Floodplain Inundation Depth (m)
H_{pred} = Predicted Bankfull Depth (m)
Q_{bf} = Bankfull Discharge (m³/s)
Q_{ch} = Channel Discharge (m³/s)
Q_e = Extra Channel Discharge above bankfull (m³/s)
Q_f = Floodplain Discharge (m³/s)
Q_i = Peak Discharge for t = i (m³/s)
$Q_{s,i}$ = Sediment Supply Rate (m³/s)
Q_{tbf} = Bankfull Transport Capacity (m³/s)
$q_{s,ch}$ = Unit Sediment Supply Rate (m³/s)
S = Slope
S_{supply} = Slope of the Supply Channel
S_f = Floodplain Slope
S_{pred} = Predicted Slope
β_a = Adjustment Parameter
θ = Floodplain Angle
μ = Location Parameter of GEV Distribution
σ = Scale Parameter of GEV Distribution
ξ = Shape Parameter of GEV Distribution
τ^*_{ch} = Channel Shields Number

Initial Steps
Iterable Steps
Variable Modification Methods
Hydraulic Model Output

Generate Peak Flow Series
$Q_p = GEV(\mu, \sigma, \xi)$

Calculate Initial Channel Geometry
$B_{bf,init} = f(Q_{bf,init}, Q_{tbf,init}, D)$
$H_{bf,init} = f(Q_{bf,init}, Q_{tbf,init}, D)$
$S_{init} = f(Q_{bf,init}, Q_{tbf,init}, D)$

Set Supply Channel Geometry
$B_{bf,supply} = B_{bf,init}$
$H_{bf,supply} = H_{bf,init}$
$S_{supply} = S_{init}$

Supply Channel Hydraulic Model
$Cz = f(S_{supply})$
$H_{ch} = f(Q_{ch}, B_{bf,supply}, S_{supply}, Cz)$
$H_e = f(Q_e, B_{bf,supply}, S_{supply}, Cz)$
$H_f = f(Q_f, S_f, Cz_f, \theta)$

Calculate Sediment Supply
$\tau^*_{ch} = f(H_{ch}, S_{supply}, D)$
$q_{s,ch} = f(\tau^*_{ch}, D)$
$Q_{s,i} = f(\tau^*_{ch}, B_{bf,supply})$

Iterate Through Each Time Step
$Q_{p,i} = Q_p @ t = i$

Update Channel Variables
$B_{bf,i}$
$H_{bf,i}$
S_i

Hydraulic Model
$Cz = f(S_{supply})$
$H_{ch} = f(Q_{p,i}, B_{bf,i}, S_i, Cz)$
$H_e = f(Q_e, B_{bf,i}, S_i, Cz)$
$H_f = f(Q_f, S_f, Cz_f, \theta)$

Output
$B_i = f(H_f, B_{bf}, \theta)$

Predict New Channel Geometry
$B_{pred} = f(Q_{p,i}, Q_{s,i}, D)$
$H_{pred} = f(Q_{p,i}, Q_{s,i}, D)$
$S_{pred} = f(Q_{p,i}, Q_{s,i}, D)$

Modify Predict Channel Geometry

Method A
$B_{bf,i+1} = B_{bf,i} + \beta_a(B_{pred} - B_{bf,i})$
$H_{bf,i+1} = H_{bf,i} + \beta_a(H_{pred} - H_{bf,i})$
$S_{i+1} = S_i + \beta_a(S_{pred} - S_i)$

Method B
If $B_{pred} > B_{bf,i}$ then $B_{bf,i+1} = B_{bf,i} + \beta_a(B_{pred} - B_{bf,i})$
Else $B_{bf,i+1} = B_{bf,i} + \beta_a(B_{pred} - B_{bf,i})$
$H_{bf,i+1} = H_{bf,i} + \beta_a(H_{pred} - H_{bf,i})$
$S_{i+1} = S_i + \beta_a(S_{pred} - S_i)$

Method C
If $B_{pred} > B_{bf,i}$ then $B_{bf,i+1} = B_{bf,i} + \beta_c(B_{pred} - B_{bf,i})$
Else $B_{bf,i+1} = B_{bf,i} + \beta_c(B_{pred} - B_{bf,i})$
If $H_{pred} > H_{bf,i}$ then $H_{bf,i+1} = H_{bf,i} + \beta_c(H_{pred} - H_{bf,i})$
Else $H_{bf,i+1} = H_{bf,i} + \beta_c(H_{pred} - H_{bf,i})$
If $S_{pred} > S_i$ then $S_{i+1} = S_i + \beta_c(S_{pred} - S_i)$
Else $S_{i+1} = S_i + \beta_c(S_{pred} - S_i)$

Figure A1. Schematic of model algorithm and functional relationships between variables.

Table A2. Summary of flow scenario input parameters and their corresponding summary statistics.

SCENARIO	LOCATION	SCALE	SHAPE	PDF MEAN	PDF STD.	PDF CV
ALL	250	75	0.2	311.5	137.1	0.44
1	125	37.5	0.2	155.7	68.5	0.44
2	125	75	0.2	186.5	137.1	0.83
3	250	37.5	0.2	280.7	68.5	0.24
4	250	120	0.2	348.5	219.4	0.63
5	400	75	0.2	461.5	137.1	0.3
6	400	120	0.2	498.5	219.4	0.44

APPENDIX B. RESULTS FROM HYPOTHETICAL FLOW AND SEDMINET

SCENARIOS

Figure B1. Plots of the mean and standard deviation of channel width for all scenarios using adjustment parameter between 0.0 and 1.0 with adjustment method A.

Channel Depth

Figure B2. Plots of the mean and standard deviation of channel depth for all scenarios using adjustment parameter between 0.0 and 1.0 with adjustment method A.

Figure B3. Plots of the mean and standard deviation of channel slope for all scenarios using adjustment parameter between 0.0 and 1.0 with adjustment method A.

Figure B4. Plots of the mean and standard deviation of inundation width for all scenarios using adjustment parameter between 0.0 and 1.0 with adjustment method A.

Figure B5. Plots of flood frequency for all scenarios using adjustment parameter between 0.0 and 1.0 with adjustment method A.

Figure B6. Plots of the mean and standard deviation of channel width for all scenarios using adjustment parameter between 0.0 and 0.05 with adjustment method A.

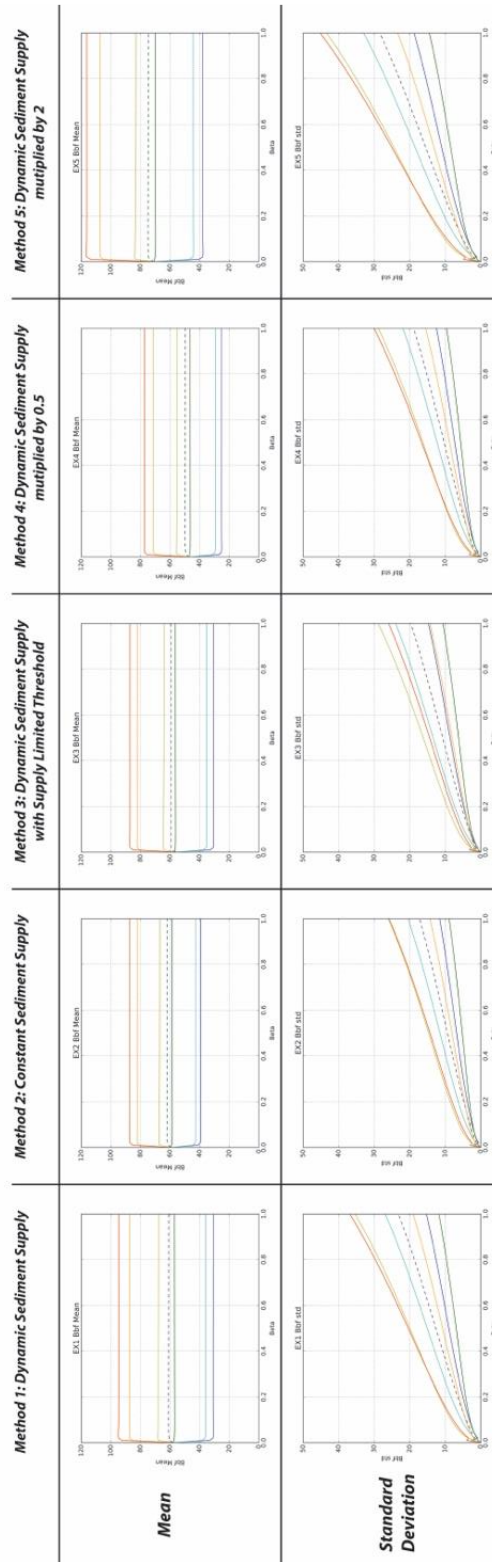**Figure B7.** Plots of the mean and standard deviation of channel depth for all scenarios using adjustment parameter between 0.0 and 0.05 with adjustment method A.
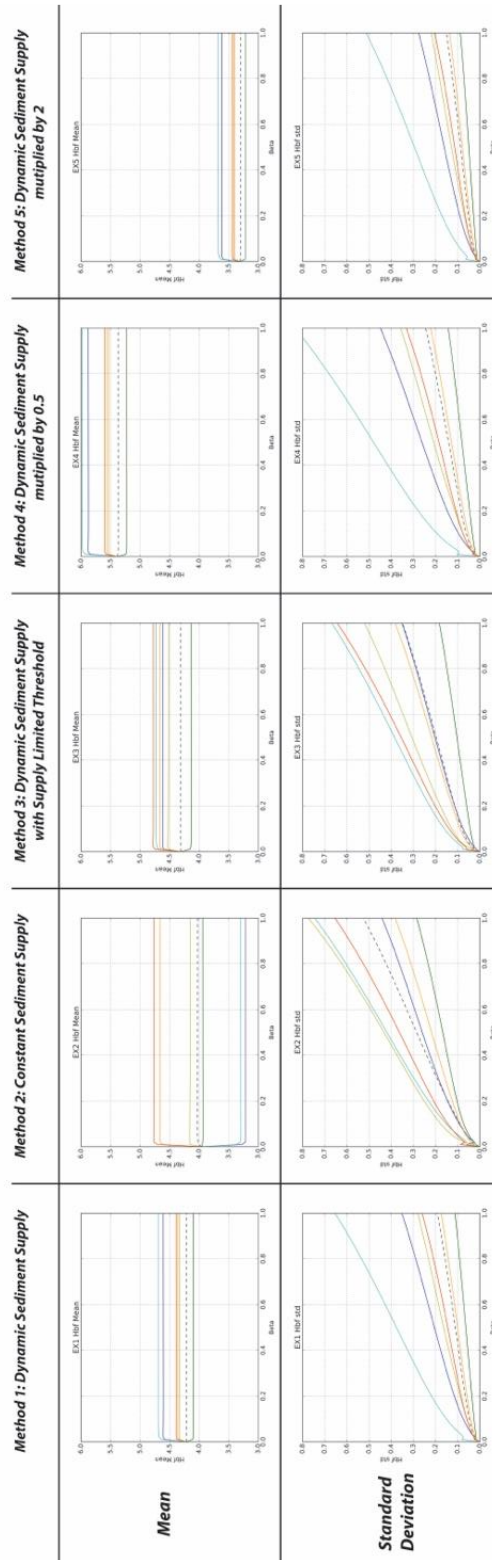
Figure B8. Plots of the mean and standard deviation of channel slope for all scenarios using adjustment parameter between 0.0 and 0.05 with adjustment method A.

Figure B9. Plots of the mean and standard deviation of inundation width for all scenarios using adjustment parameter between 0.0 and 0.05 with adjustment method A.

Figure B10. Plots of flood frequency for all scenarios using adjustment parameter between 0.0 and 0.05 with adjustment method A.

Figure B11. 3D plots of the mean and standard deviation of channel width for all scenarios using adjustment parameters between 0.0 and 1.0 with adjustment method B.

Figure B12. 3D plots of the mean and standard deviation of channel depth for all scenarios using adjustment parameters between 0.0 and 1.0 with adjustment method B.
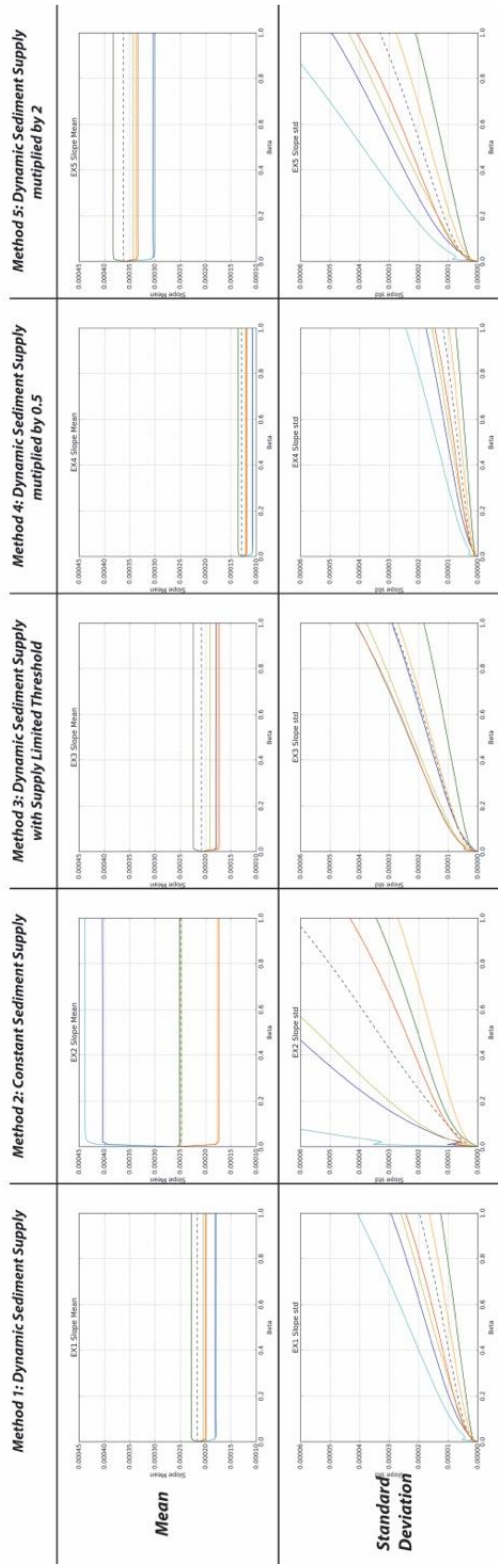
Figure B13. 3D plots of the mean and standard deviation of slope for all scenarios using adjustment parameters between 0.0 and 1.0 with adjustment method B.

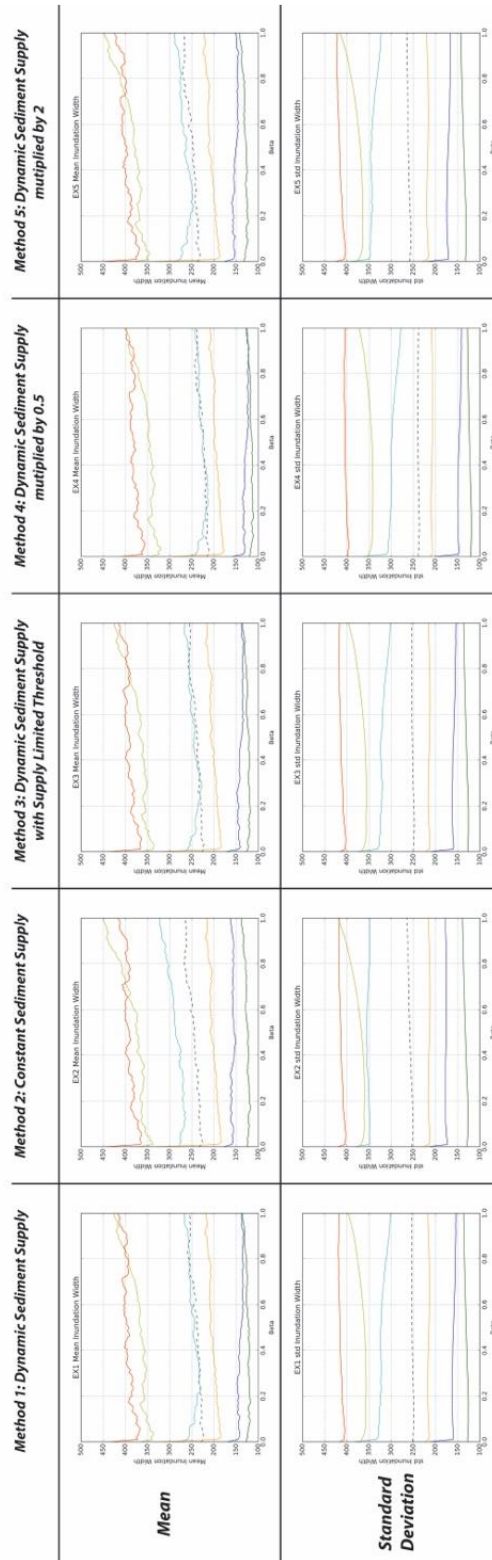**Figure B14.** 3D plots of the mean and standard deviation of inundation width for all scenarios using adjustment parameters between 0.0 and 1.0 with adjustment method B.
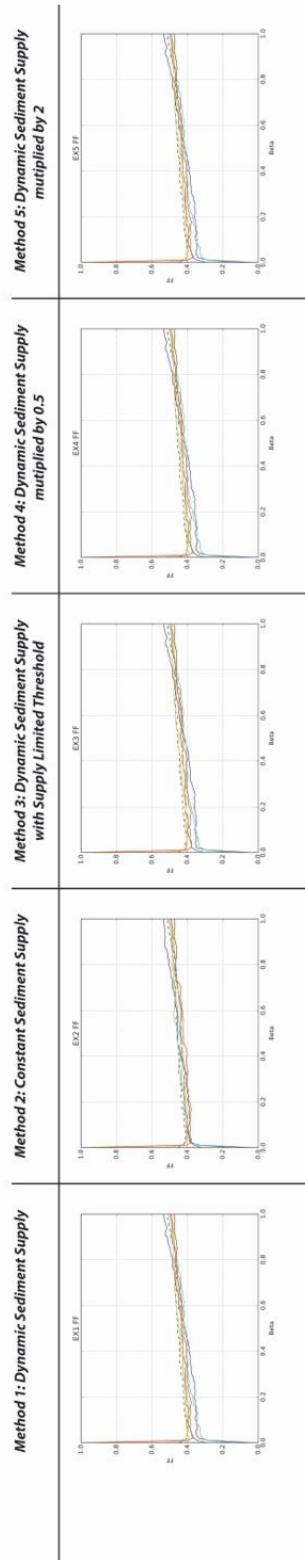
Figure B15. 3D plots of flood frequency for all scenarios using adjustment parameters between 0.0 and 1.0 with adjustment method B.
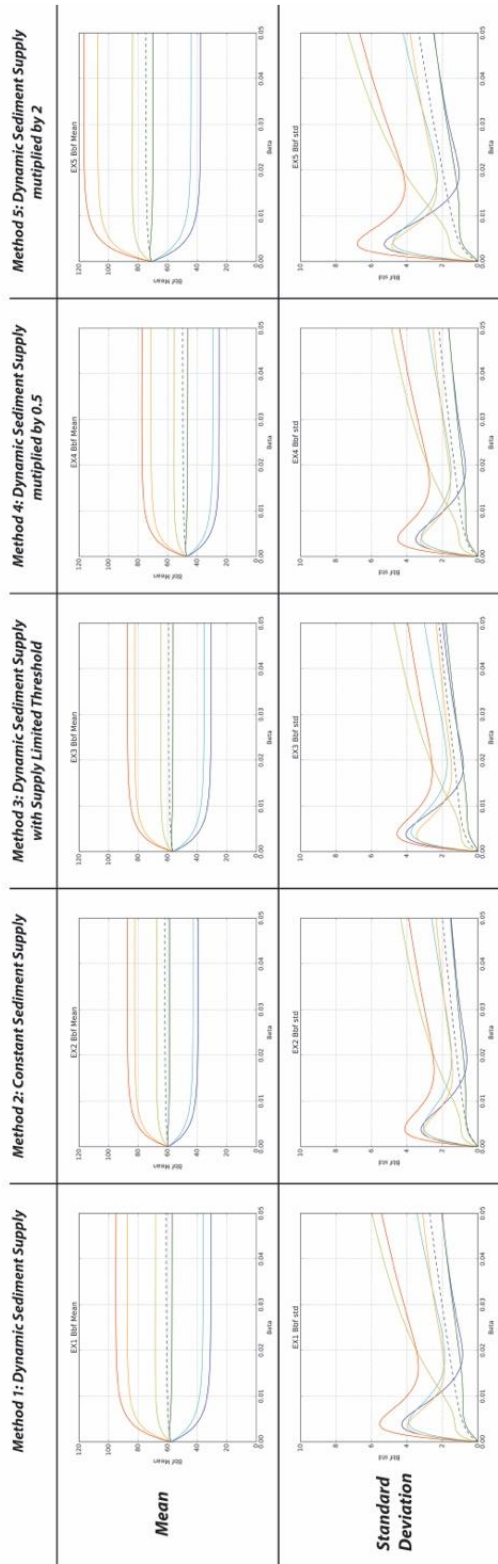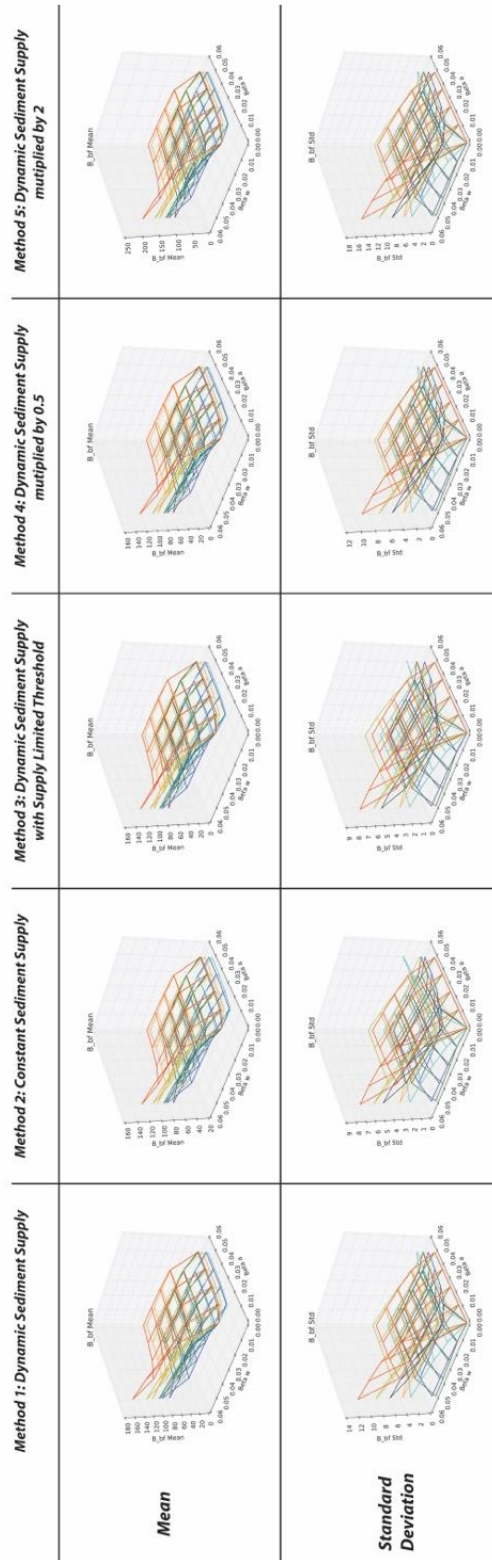
Figure B16. 3D plots of the mean and standard deviation of width for all scenarios using adjustment parameters between 0.0 and 0.05 with adjustment method B.

Figure B17. 3D plots of the mean and standard deviation of depth for all scenarios using adjustment parameters between 0.0 and 0.05 with adjustment method B.

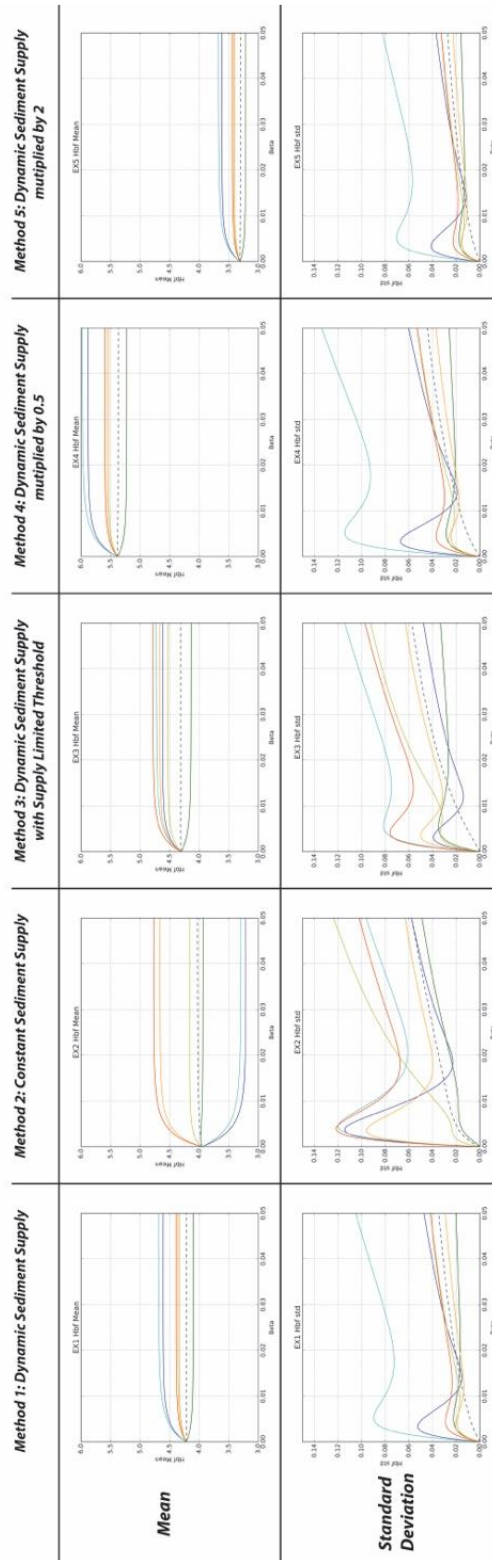**Figure B18.** 3D plots of the mean and standard deviation of slope for all scenarios using adjustment parameters between 0.0 and 0.05 with adjustment method B.

Figure B19. 3D plots of the mean and standard deviation of inundation width for all scenarios using adjustment parameters between 0.0 and 0.05 with adjustment method B.

Figure B20. 3D plots of flood frequency for all scenarios using adjustment parameters between 0.0 and 0.05 with adjustment method B.
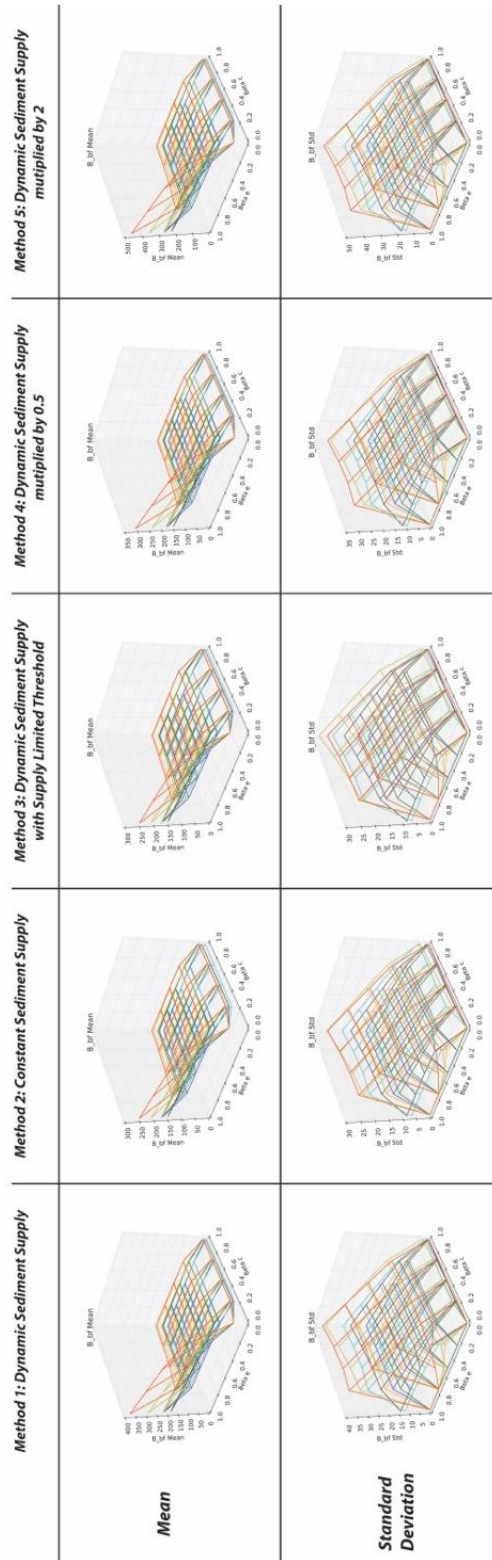
Figure B21. 3D plots of the mean and standard deviation of channel width for all scenarios using adjustment parameters between 0.0 and 1.0 with adjustment method C.
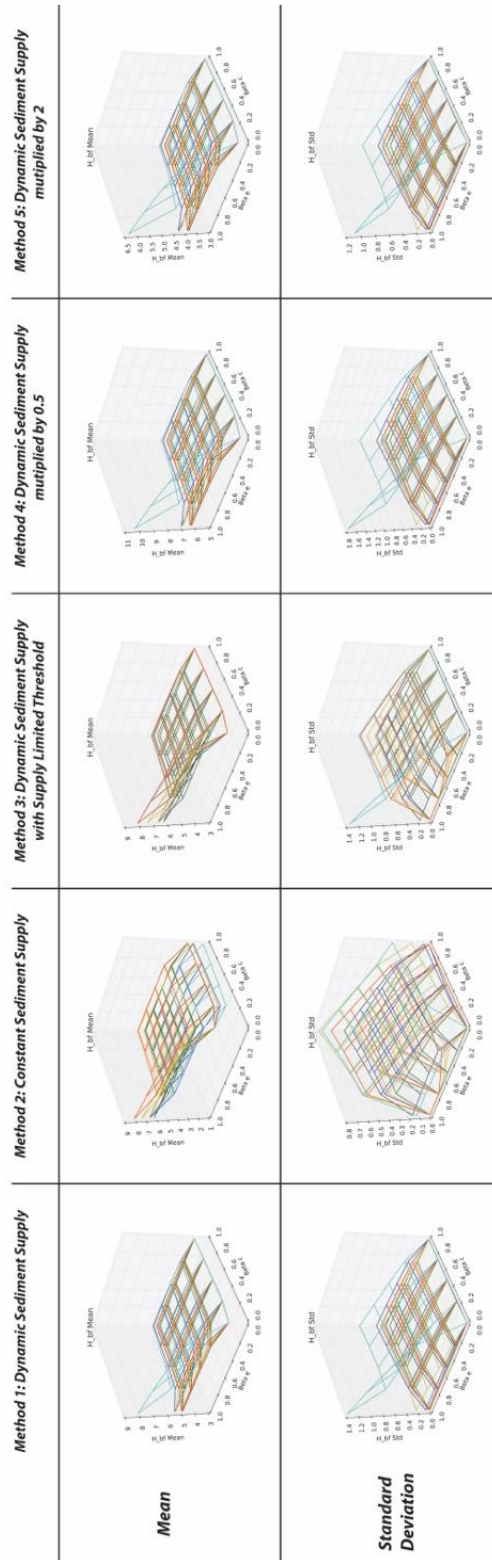
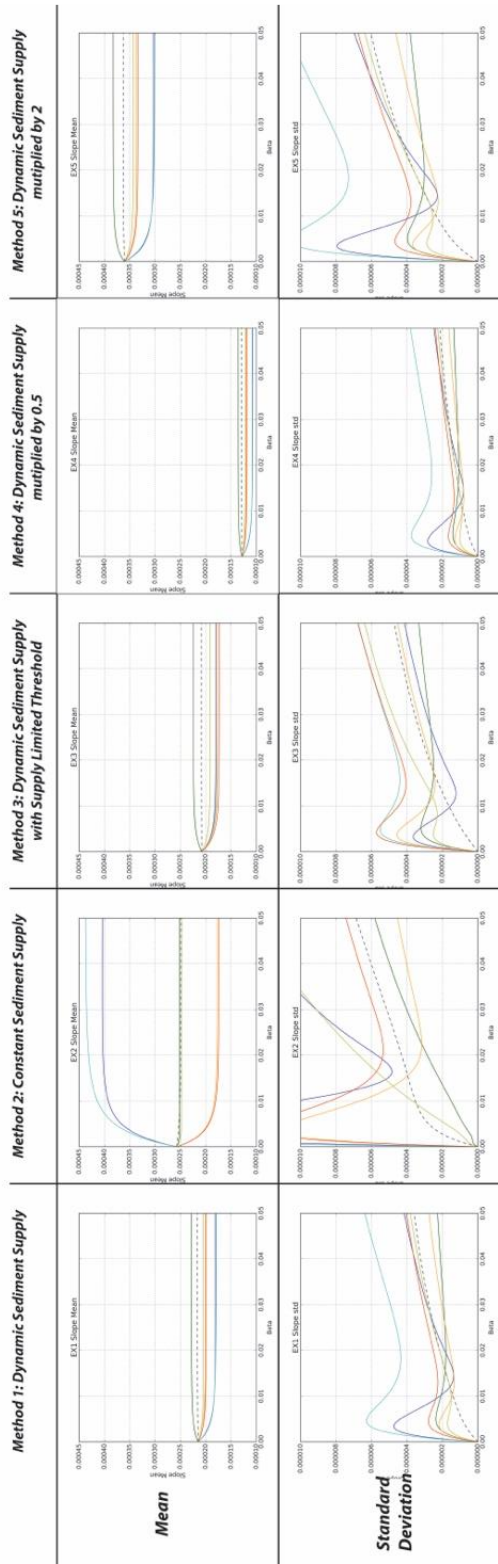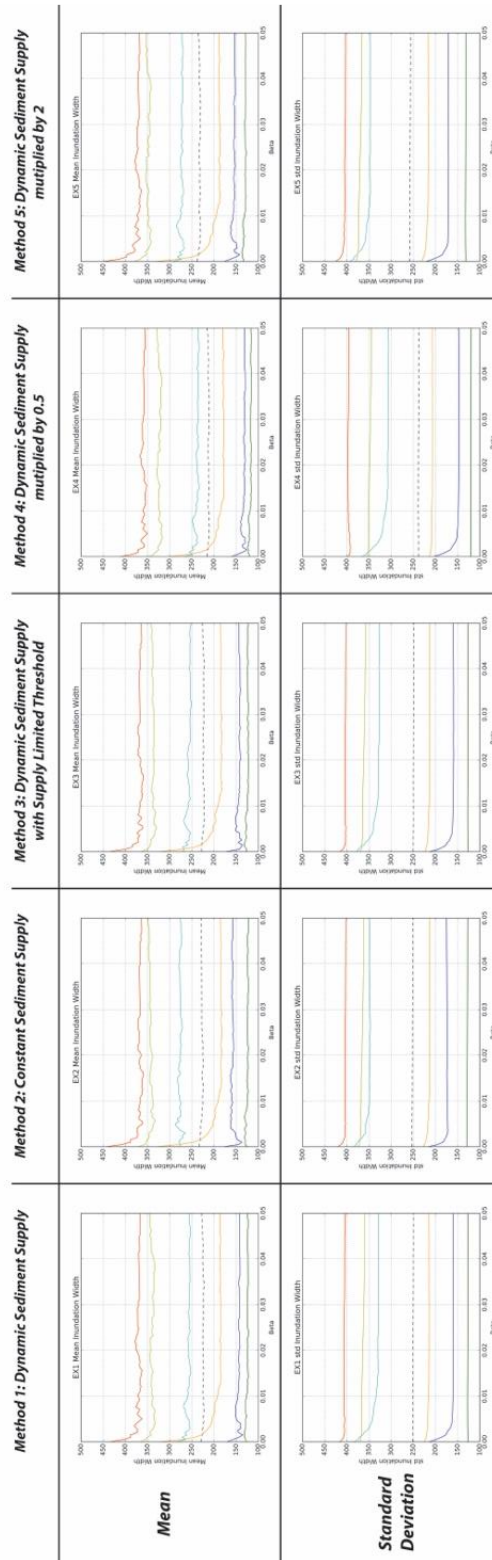**Figure B22.** 3D plots of the mean and standard deviation of channel depth for all scenarios using adjustment parameters between 0.0 and 1.0 with adjustment method C.
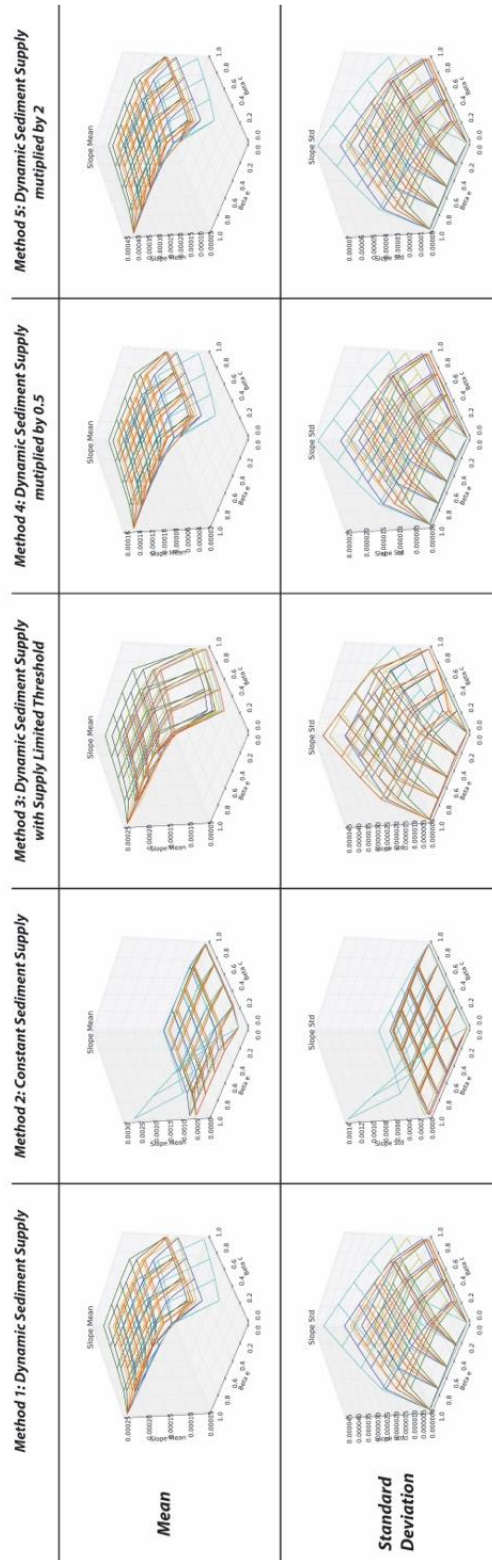
Figure B23. 3D plots of the mean and standard deviation of channel slope for all scenarios using adjustment parameters between 0.0 and 1.0 with adjustment method C.

113
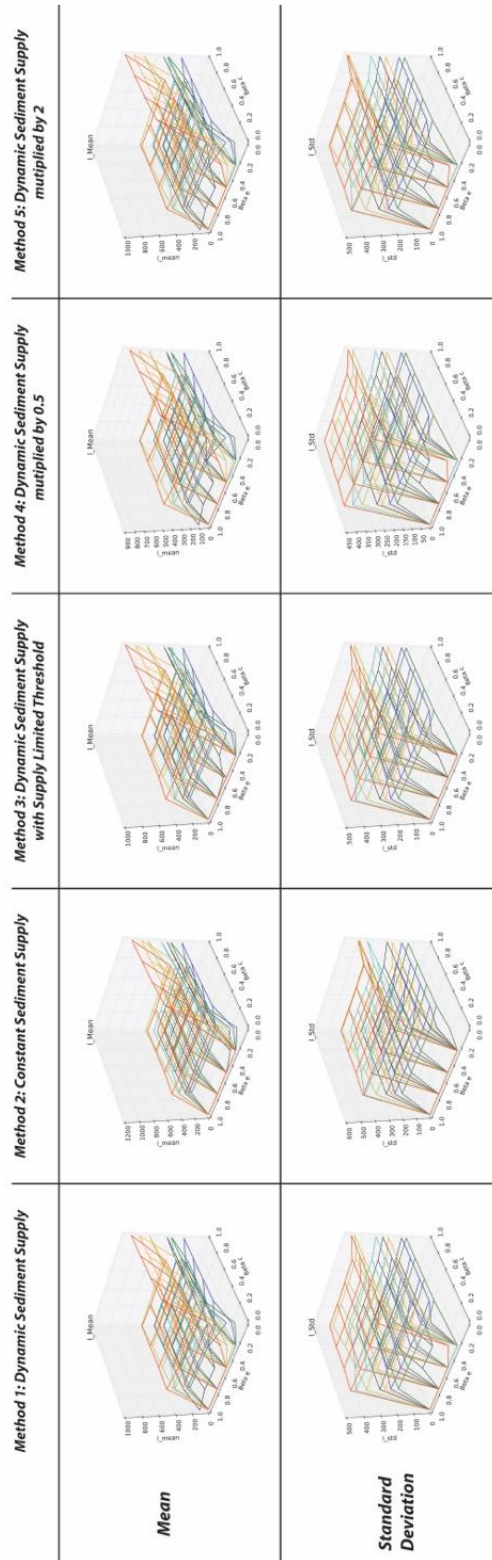
Figure B24. 3D plots of the mean and standard deviation of inundation width for all scenarios using adjustment parameters between 0.0 and 1.0 with adjustment method C.
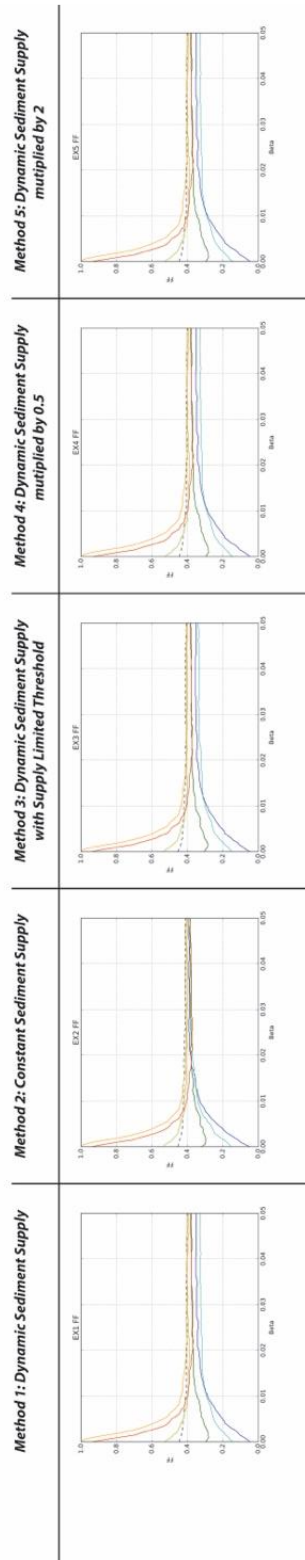
114
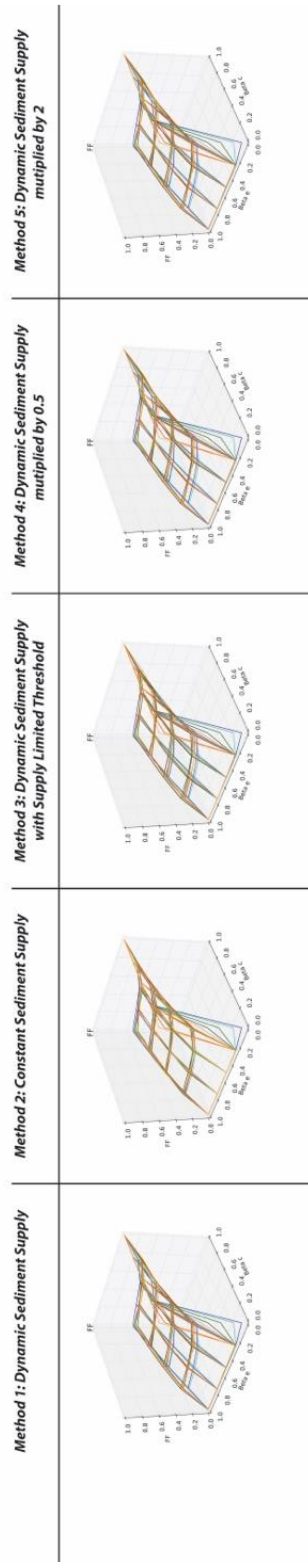
Figure B25. 3D plots of flood frequency for all scenarios using adjustment parameters between 0.0 and 1.0 with adjustment method C.
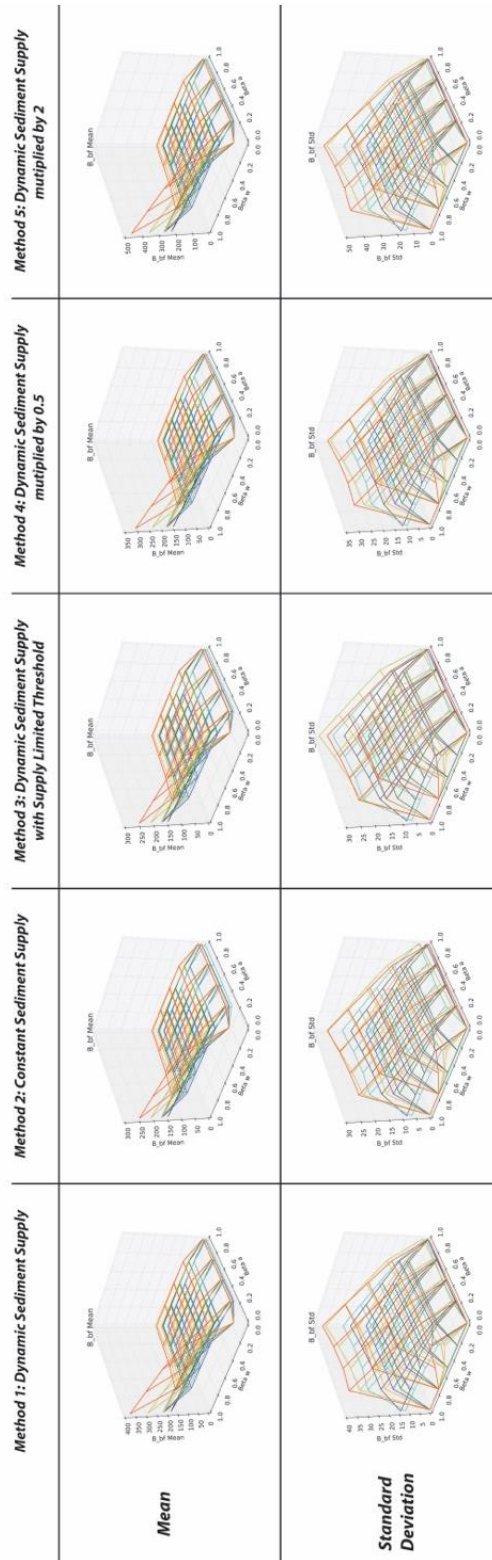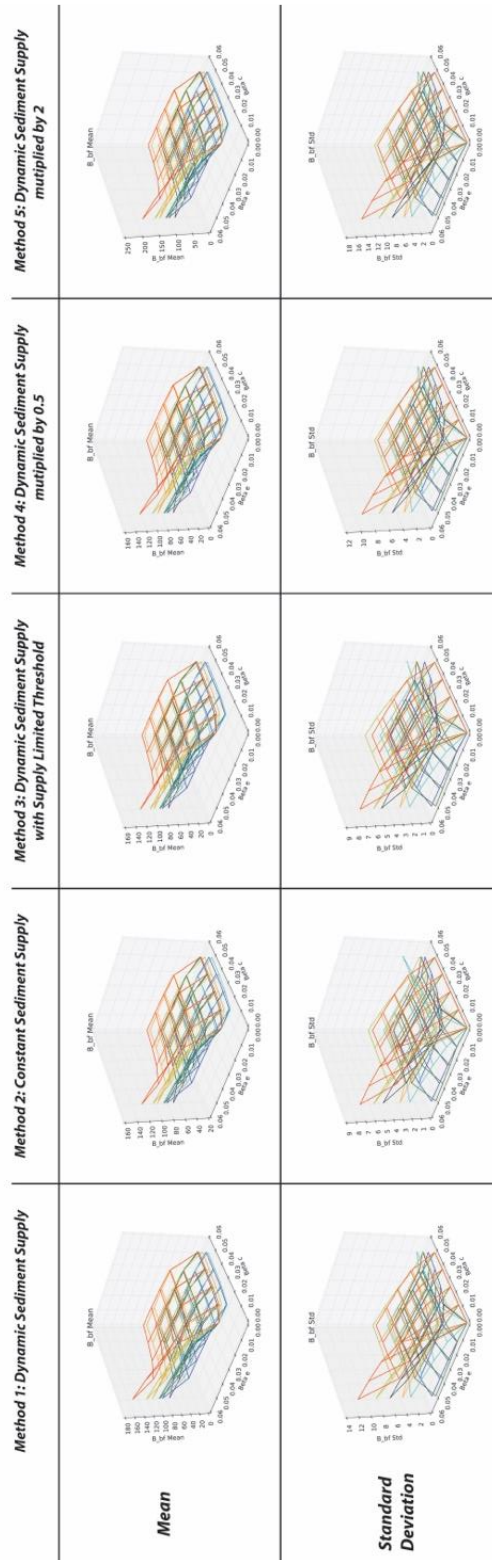
Figure B26. 3D plots of the mean and standard deviation of channel width for all scenarios using adjustment parameters between 0.0 and 0.05 with adjustment method C.
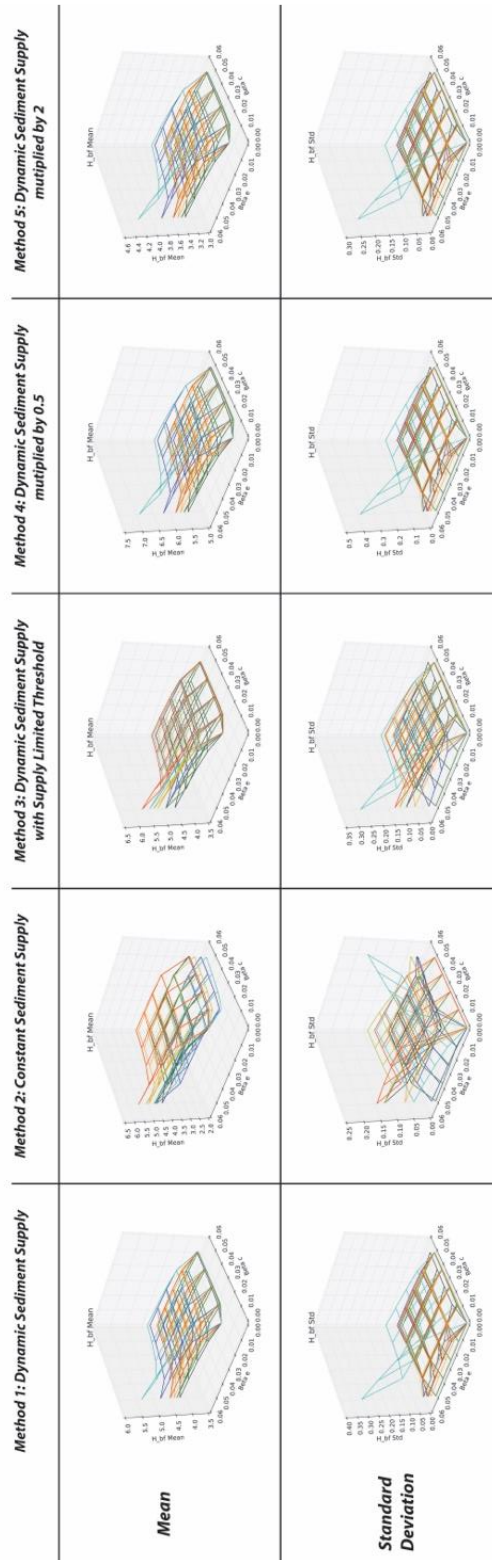
Figure B27. 3D plots of the mean and standard deviation of channel depth for all scenarios using adjustment parameters between 0.0 and 0.05 with adjustment method C.

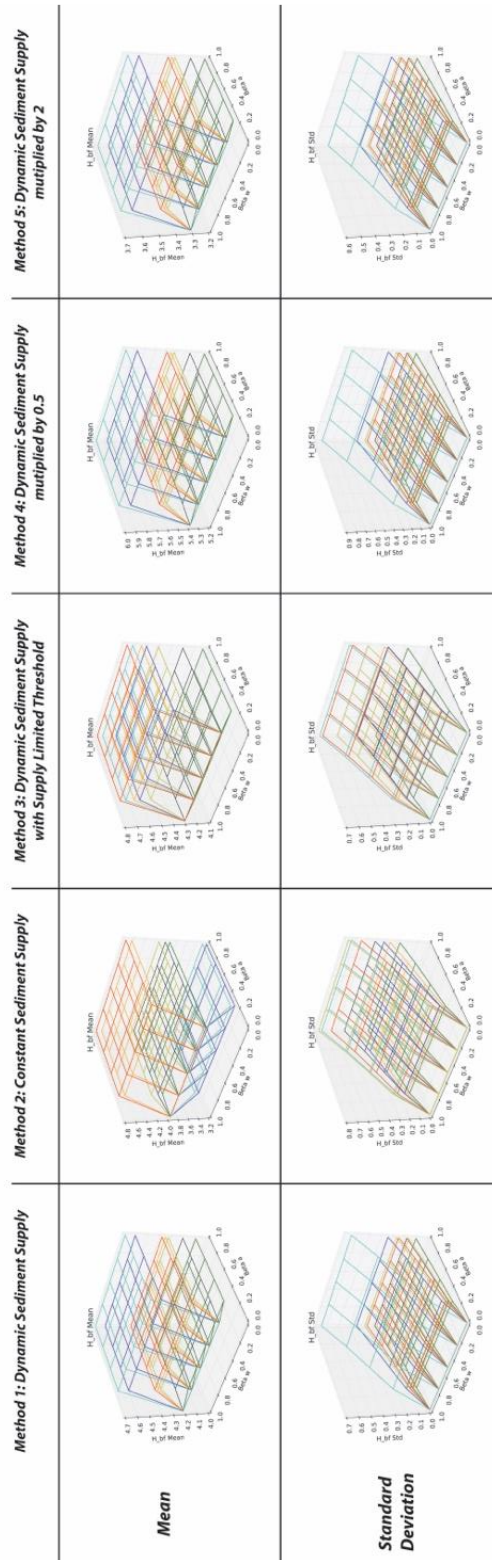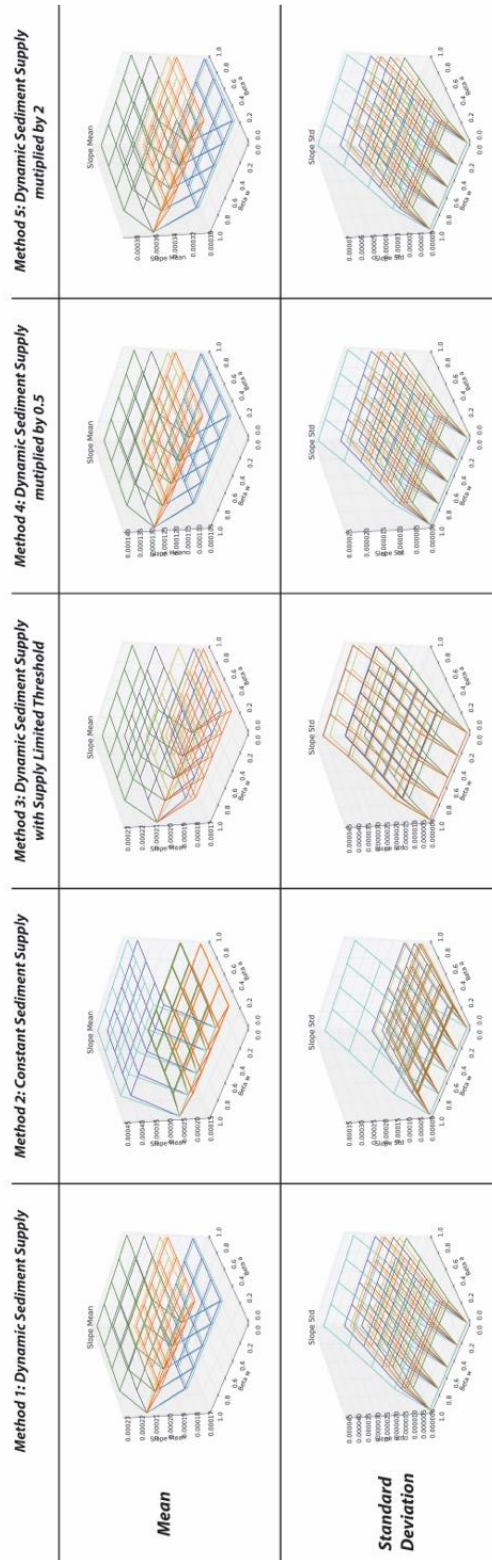**Figure A28.** 3D plots of the mean and standard deviation of channel slope for all
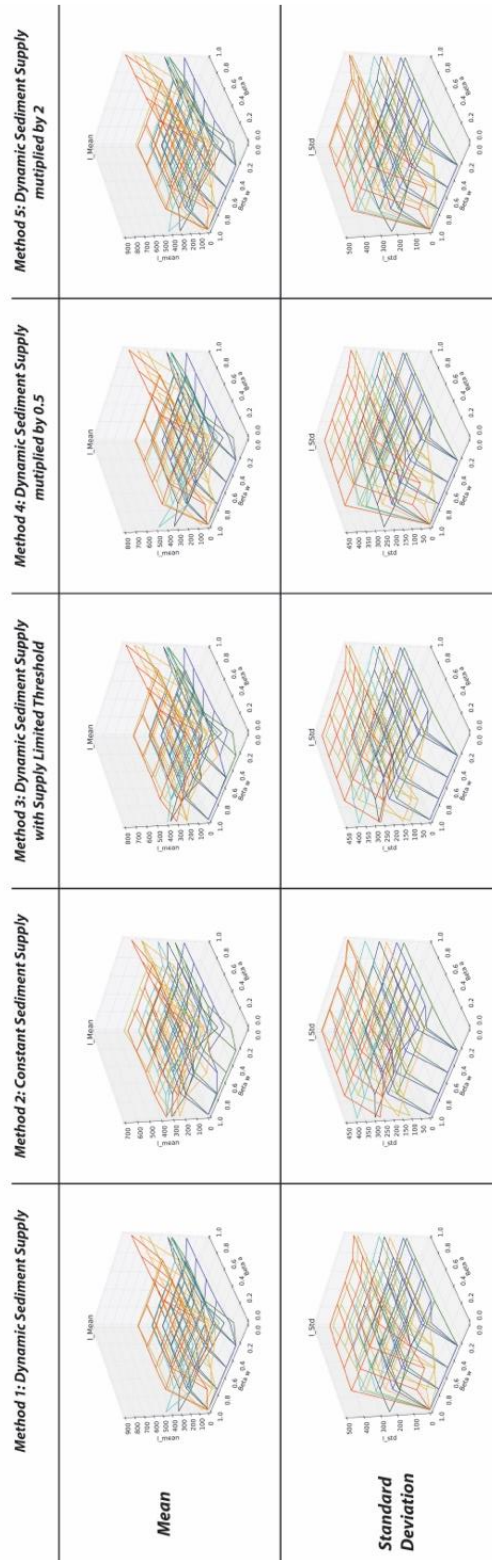scenarios using adjustment parameters between 0.0 and 0.05 with adjustment method C.

Figure B29. 3D plots of the mean and standard deviation of inundation width for all scenarios using adjustment parameters between 0.0 and 0.05 with adjustment method C.
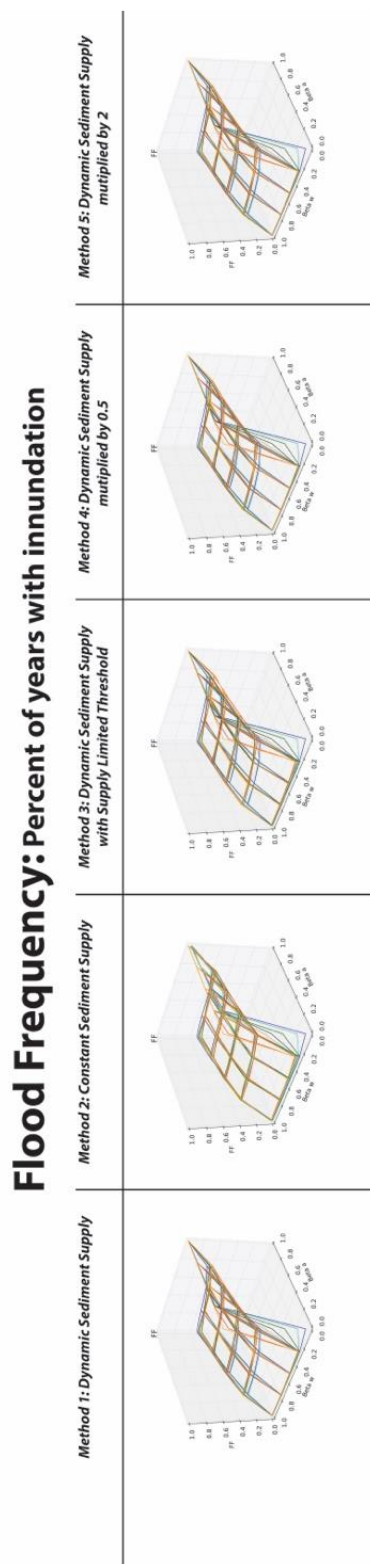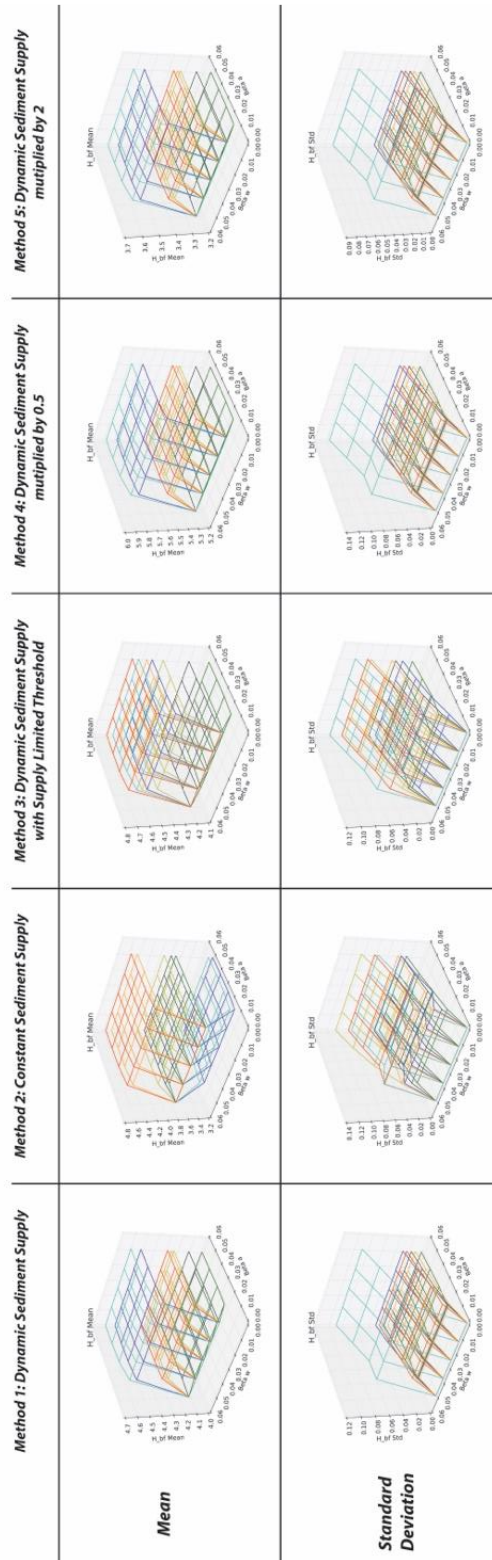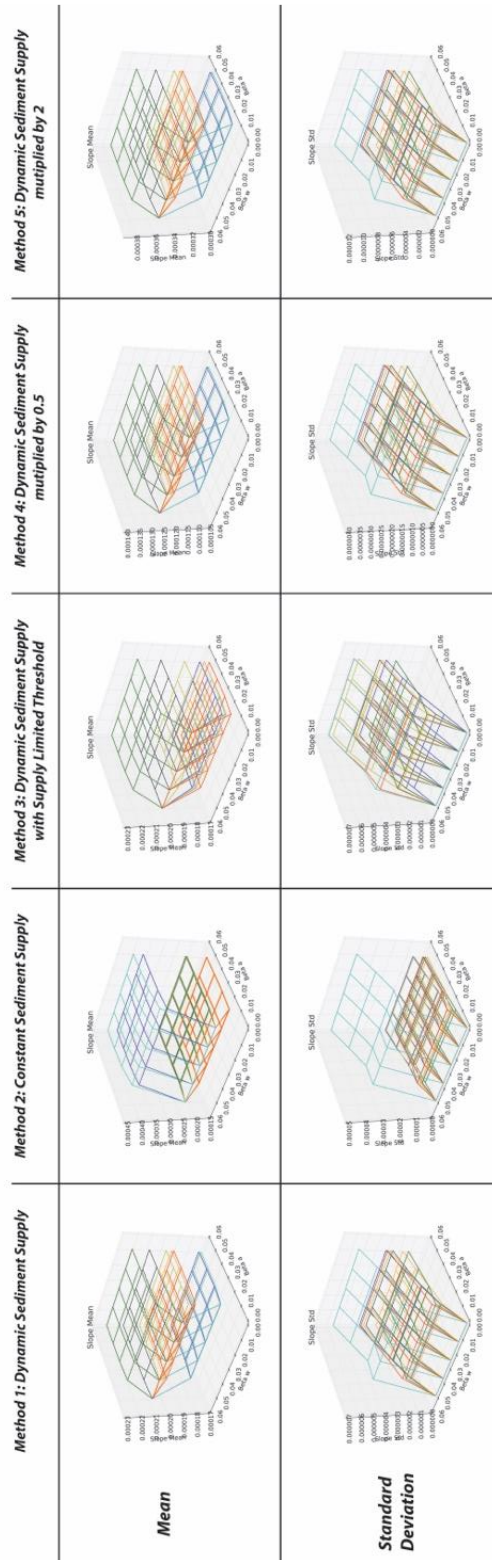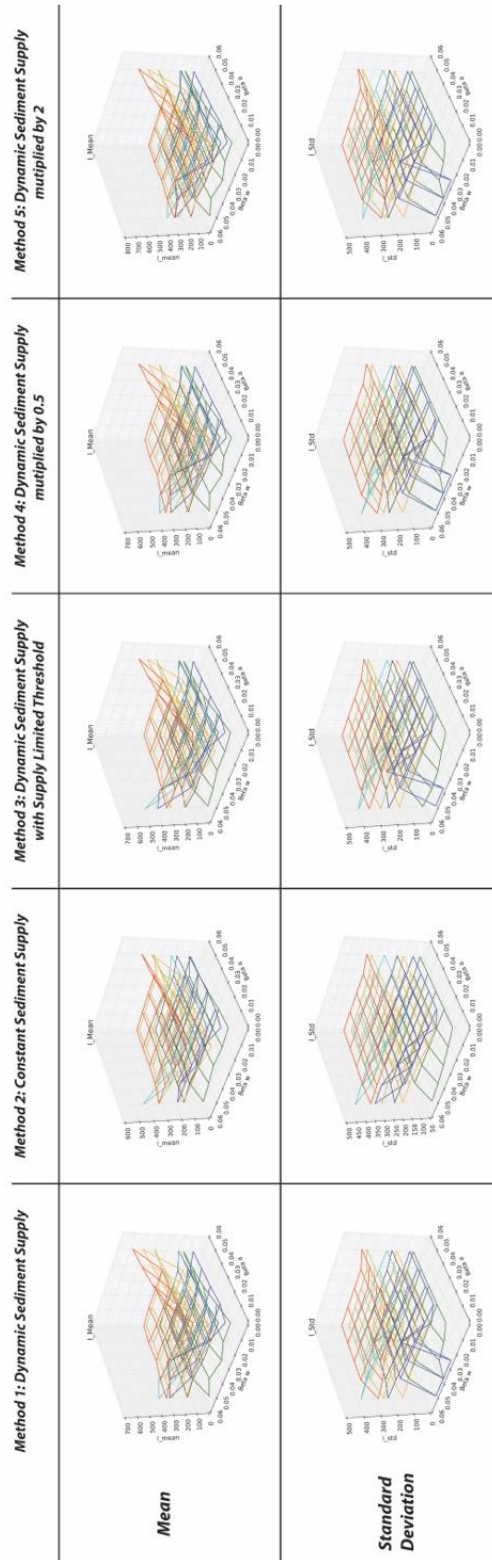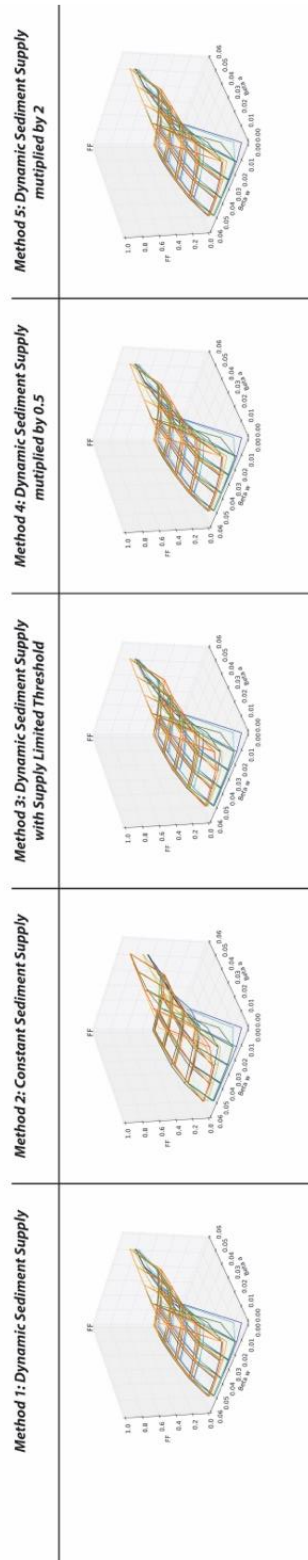
Figure B30. 3D plots of flood frequency for all scenarios using adjustment parameters between 0.0 and 0.05 with adjustment method C.
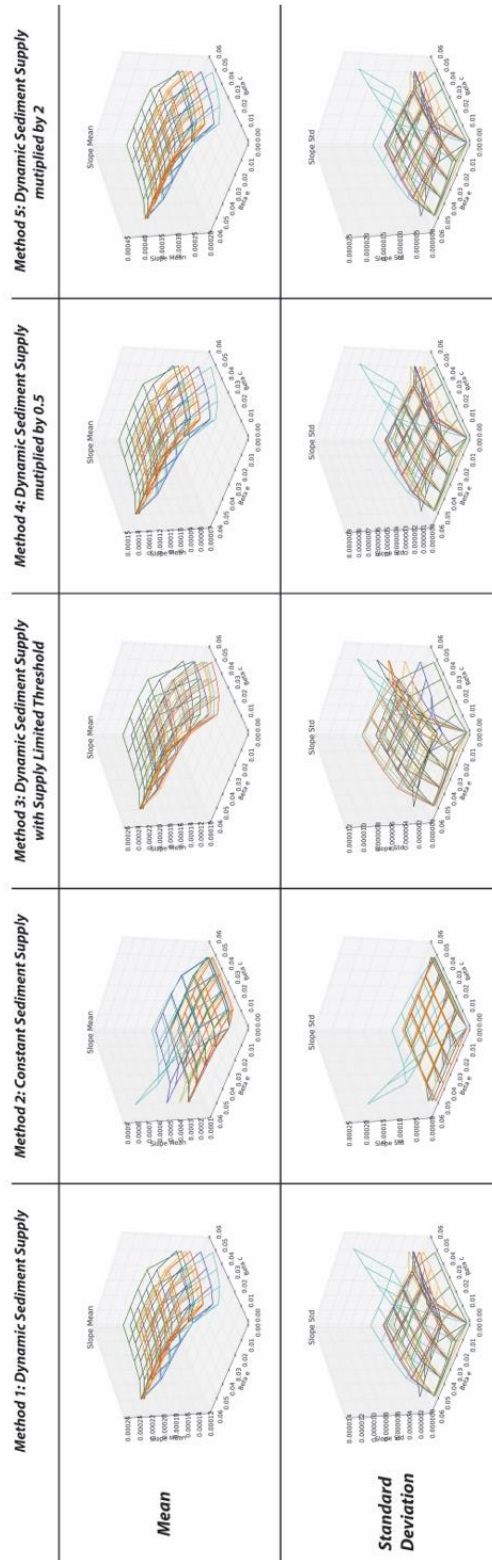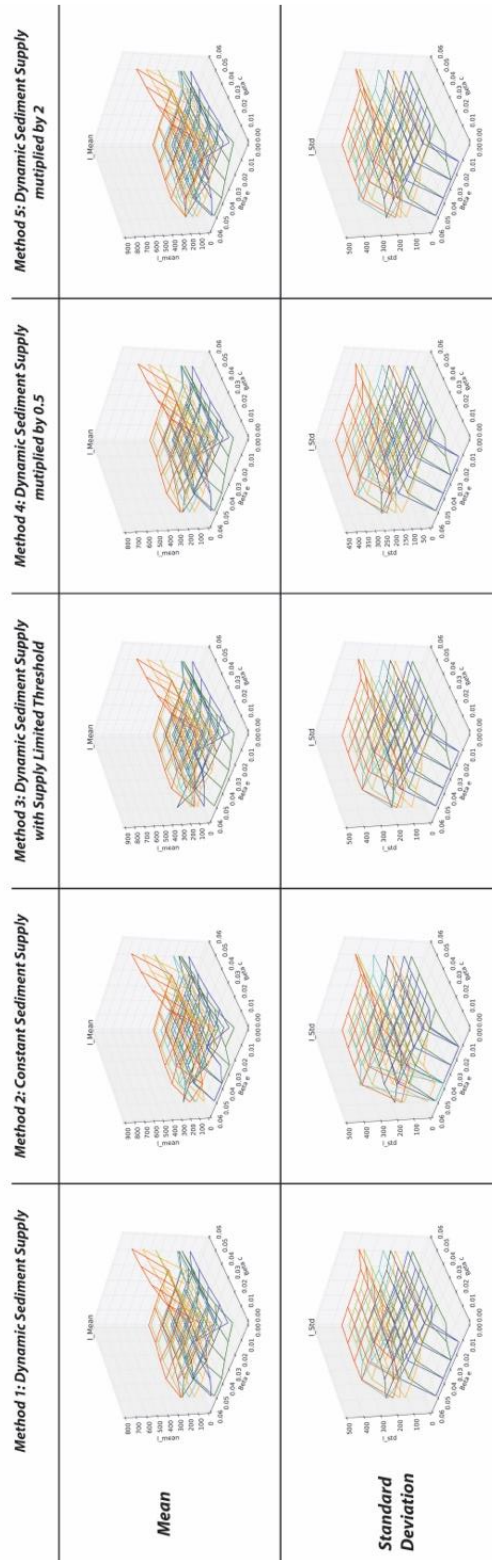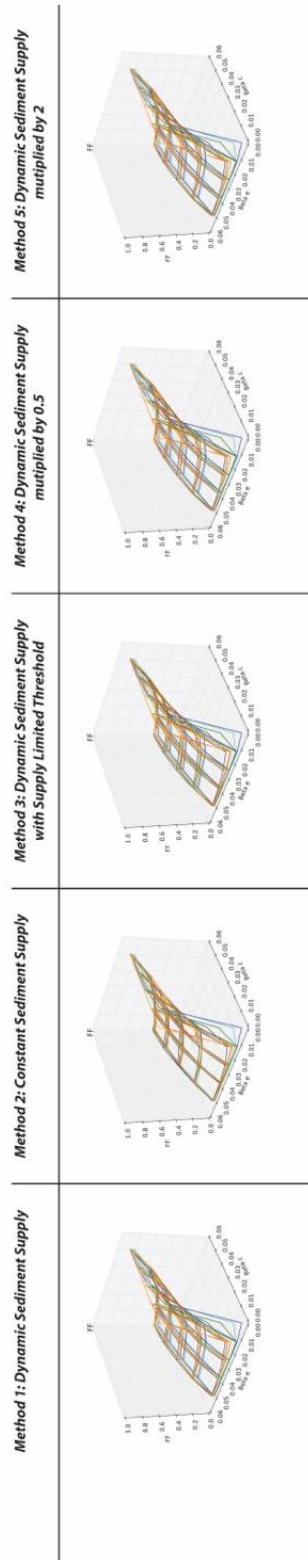
APPENDIX C. CROSS-SECTION DATA

Table C1. Cross-section data from 2008 for the Le Sueur River within the knick zone (darker blue) and above (lighter blue) and for the Maple river within the knick zone (darker orange) and above (lighter orange).

Name	US_dist_km	UTM_N	UTM_E	Slope	DrainA_km2	Date_2008	Width_m_2008	AvgDepth_m_2008	MaxDepth_m_2008	WetPerim_m_2008	Area_m2_2008	HydRadius_2008
L1.94	1.94	4885385	416037	0.0012	2869	9/5/08	44.20	1.47	2.01	44.60	64.97	1.46
L4.49	4.49	4883766	416938	0.0012	2860.3	7/16/08	41.00	2.78	3.92	43.25	114.18	2.64
L8.98	8.98	4882531	418808	0.00103	2852.2	7/16/08	50.00	1.99	2.81	51.10	99.72	1.95
L11.53	11.53	4881227	419141	0.00105	1956.6	9/4/08	41.41	1.35	1.83	41.97	55.81	1.33
L13.66	13.66	4881179	419929	0.00109	1151.8	7/16/08	29.00	1.71	2.43	30.26	49.51	1.64
L15.15	15.15	4881816	420688	0.00121	1145.8	9/5/08	38.00	1.73	2.82	39.18	65.63	1.68
L19.59	19.59	4882179	422770	0.00109	1142.6	7/15/08	35.50	1.68	2.39	37.01	59.48	1.61
L21.25	21.25	4882480	423392	0.0013	1138.1	7/24/08	36.36	0.86	1.15	36.64	31.26	0.85
L24.18	24.18	4883355	423949	0.00155	1109.3	7/15/08	30.50	1.76	2.78	31.56	53.66	1.70
L26.27	26.27	4884573	424549	0.00163	1107.8	9/5/08	31.20	0.80	1.31	31.68	24.83	0.78
L27.26	27.26	4885345	424417	0.00182	1106	7/15/08	29.70	1.86	2.61	30.68	55.32	1.80
L29.48	29.48	4886325	424880	0.00163	1089.2	7/15/08	37.00	2.38	3.25	38.38	88.08	2.29
L31.99	31.99	4885664	425843	0.00151	1086.5	9/5/08	26.50	2.55	2.91	28.92	67.55	2.34
L37.48	37.48	4886366	428713	0.00098	1072.6	6/27/08	34.63	2.16	2.75	35.76	74.84	2.09
L39.11	39.11	4887116	429246	0.00085	1070.6	6/27/08	26.37	2.25	3.63	28.45	59.37	2.09
L42.8	42.8	4886875	430696	0.00061	1068.4	6/27/08	28.00	2.60	3.41	30.03	72.89	2.43
L47.84	47.84	4884432	430691	0.00054	951.4	6/26/08	27.50	2.07	2.95	28.84	56.87	1.97
L50.83	50.83	4883546	430450	0.00076	949.5	6/26/08	24.76	2.87	3.87	28.02	71.15	2.54
L58.81	58.81	4880796	433023	0.0004	864.7	6/25/08	25.50	1.90	2.51	27.17	48.55	1.79
M0.28	0.28	4882023	418467	0.00358	893.7	7/9/08	32.00	2.25	2.88	33.60	72.13	2.15
M4.66	4.66	4880222	417911	0.00191	889.5	7/9/08	43.45	1.12	2.33	44.30	48.68	1.10
M5.56	5.56	4879631	417801	0.00085	883.9	7/9/08	38.56	1.73	2.31	39.37	66.84	1.70
M8.09	8.09	4878314	417921	0.00111	882.8	7/9/08	26.07	2.29	3.08	28.27	59.78	2.11
M10.58	10.58	4877472	417442	0.00215	878.6	7/9/08	29.00	1.86	2.71	30.49	54.01	1.77
M12.44	12.44	4876871	417387	0.00164	877.8	7/9/08	28.47	1.69	2.62	30.11	48.15	1.60
M17.26	17.26	4874984	415827	0.00188	870.1	7/8/08	29.00	2.17	3.29	30.72	62.79	2.04
M23.13	23.13	4873190	415416	0.00159	866.1	7/8/08	26.00	1.74	2.36	27.36	45.34	1.66
M25.28	25.28	4871803	415090	0.00235	828.5	7/8/08	26.00	1.43	2.04	26.85	37.11	1.38
M27.87	27.87	4870957	413694	0.00148	826.9	7/8/08	30.50	2.39	2.81	32.31	72.98	2.26
M29.55	29.55	4869982	413896	0.00105	824.9	7/1/08	28.00	2.15	2.76	29.66	60.32	2.03
M31.71	31.71	4869056	414615	0.00115	824.1	7/1/08	30.00	2.07	3.15	31.10	62.01	1.99
M34.99	34.99	4867819	414426	0.0021	815	7/1/08	25.04	2.17	2.55	27.12	54.31	2.00
M38.94	38.94	4866019	414023	0.00062	802.8	7/1/08	23.00	1.71	2.16	24.78	39.28	1.59
M40.39	40.39	4865138	414420	0.00032	799.3	7/16/08	25.50	1.67	2.56	26.41	42.62	1.61
M46.19	46.19	4862708	416142	0.00007	723.7	6/19/08	17.00	1.52	2.12	18.03	25.86	1.43
M50.78	50.78	4861801	417285	0.00031	516.7	6/19/08	26.00	1.54	2.79	28.12	39.98	1.42
M54.12	54.12	4861856	419403	0.00046	500.1	6/19/08	20.00	1.14	1.95	20.47	22.70	1.11
M58.71	58.71	4862522	421129	0.00038	479.1	6/19/08	19.80	2.05	3.14	21.39	40.62	1.90
M63.59	63.59	4859986	421129	0.00034	469	6/18/08	29.00	1.62	2.03	30.77	46.94	1.53
M66.15	66.15	4859986	422178	0.00029	468	6/18/08	19.50	1.62	2.08	21.26	31.52	1.48
M70.11	70.11	4858268	423605	0.00035	457.1	6/17/08	18.90	1.32	2.14	19.77	24.97	1.26
M74.59	74.59	4856852	423864	0.00009	400	6/17/08	13.50	1.56	2.36	14.76	21.04	1.43
M76.83	76.83	4855467	423864	0.00092	227.1	6/17/08	17.10	1.29	1.83	17.82	22.11	1.24

Table C2. Cross-section data from 2015 for the Le Sueur River within the knick zone (darker blue) and above (lighter blue) and for the Maple river within the knick zone (darker orange) and above (lighter orange).

Date_2015	Width_m_2015	AvgDepth_m_2015	MaxDepth_m_2015	WetPerim_m_2015	Area_m2_2015	HydRadius_2015
5/8/15	53.80	2.71	3.93	55.49	145.80	2.63
5/9/15	53.88	2.93	3.95	56.13	157.68	2.81
5/11/15	59.05	4.95	6.80	62.56	292.27	4.67
5/7/15	48.10	3.12	3.94	50.53	150.06	2.97
5/11/15	32.93	2.50	3.54	35.89	82.33	2.29
5/9/15	39.04	2.33	3.58	40.42	90.79	2.25
5/11/15	63.64	1.66	2.97	65.18	105.36	1.62
5/9/15	40.35	2.55	3.31	42.30	102.80	2.43
5/11/15	43.32	1.96	3.34	45.22	84.79	1.88
5/9/15	45.16	2.61	3.83	47.12	118.07	2.51
5/12/15	31.73	1.87	2.66	32.85	59.30	1.80
5/12/15	30.98	2.51	3.41	32.66	77.82	2.38
5/9/15	31.76	2.14	2.87	33.00	67.88	2.06
5/12/15	35.59	2.29	3.01	36.84	81.50	2.21
5/12/15	26.60	2.33	3.54	27.99	62.04	2.22
5/13/15	28.97	2.47	3.11	30.79	71.70	2.33
5/13/15	30.30	2.50	3.10	32.75	75.89	2.32
5/13/15	30.15	2.79	4.10	32.16	84.08	2.61
5/8/15	32.14	2.65	3.27	34.66	85.12	2.46
5/11/15	30.01	1.83	2.47	31.24	55.02	1.76
5/14/15	59.18	1.42	2.91	60.39	84.32	1.40
5/9/15	34.02	1.78	2.36	35.17	60.45	1.72
5/16/15	34.94	2.56	2.97	37.50	89.41	2.38
5/16/15	29.32	2.08	2.80	31.26	60.88	1.95
5/16/15	33.58	2.58	3.46	35.70	86.76	2.43
5/16/15	41.44	2.14	3.63	42.42	88.51	2.09
5/16/15	30.00	2.98	4.01	32.73	89.46	2.73
5/28/15	27.49	1.64	2.36	28.79	44.97	1.56
5/28/15	33.45	2.32	3.27	34.65	77.51	2.24
5/9/15	32.00	2.26	2.93	33.30	72.42	2.17
5/28/15	27.22	2.36	3.38	29.66	64.24	2.17
5/28/15	27.29	2.29	2.68	29.41	62.47	2.12
5/28/15	23.93	1.88	2.37	25.49	44.96	1.76
5/9/15	26.62	2.34	3.25	29.22	62.29	2.13
5/26/15	17.18	1.83	2.24	18.74	31.47	1.68
5/23/15	19.87	1.79	2.22	21.32	35.52	1.67
5/23/15	17.61	1.59	2.26	18.62	28.01	1.50
5/23/15	20.09	2.30	3.30	25.02	46.19	1.85
5/19/15	29.10	1.63	1.92	30.23	47.47	1.57
5/19/15	22.91	1.48	2.04	24.30	33.97	1.40
5/14/15	19.76	1.62	2.32	20.73	32.00	1.54
5/14/15	16.05	1.18	2.24	17.15	18.99	1.11
5/9/15	16.76	1.37	1.83	17.73	23.02	1.30

APPENDIX D. MODEL CODE

```python
import numpy as np
import matplotlib.pyplot as plt
import pandas as pd
import numba
from scipy.stats import genextreme


### Section 1: Generate peak flow series and define model parameters

# Generate synthetic flood series
n = 1000 # Total number of years simulated
loc1 = 250 # Location parameter for the first PDF
scale1 = 75 # Scale parameter for the first PDF
shape1 = -0.2 # Shape parameter for the first PDF
loc2 = 400 # Location parameter for the second PDF
scale2 = 125 # Scale parameter for the second PDF
shape2 = -0.2 # Shape parameter for the second PDF

# Generate flood series as randomly sampled values from PDFs
series1 = genextreme.rvs(shape1, loc1, scale1, n/2) # First PDF
series2 = genextreme.rvs(shape2, loc2, scale2, n/2) # Second PDF
total = np.concatenate((series1, series2)) # Concatenate both series
Qp = {"Q_p":total} # Peak discharge series as a dictionary for import into Pandas

# Define Sediment Scenario
SS = "1" # Number from 1 to 5

# Define Adjustment Method
Method = "A" # A, B, or C

# Define Adjustment Parameters
beta_1 = 0.05 # Beta a (Method B) or Beta c (Method C)
beta_2 = 0.03 # Beta w (Method B) or Beta e (Method C)

# Define Static Parameters
Q_bf_init = genextreme(shape1, loc1, scale1).median() # Initial bankfull discharge
Qt_bf_init = 0.05 # Initial bankfull transport capacity
D = 0.0003 # Grain size (m)
theta = 0.1 #Floodplain angle (in degrees)
Cz_f = 2.1 # Floodplain hydraulic roughness
Slope_floodplain = 0.0004 # Floodplain slope

# Define Hydraulic Geometry Parameters
R = 1.65 # Submerged particle density
```

```
nu = 0.000001 # Kinematic viscosity(m^2/s)
g = 9.81 # Gravity (m/s^2)
D_star = (((R*g)**(1.0/3.0)) / (nu**(2.0/3.0))) * D # Dimensionless grain-size
alpha_EH = 0.05 # Parameter for Li et al. hydraulic geometry relations
alpha_R  = 2.53 # Parameter for Li et al. hydraulic geometry relations
beta = 1220 # Parameter for Li et al. hydraulic geometry relations
m = 0.53 # Parameter for Li et al. hydraulic geometry relations
n_R = 0.19 # Parameter for Li et al. hydraulic geometry relations




### Section 2: Define model functions

# Main model function
def Model(Qp, Q_bf, Qt_bf, B_bf, H_bf, Slope, beta_1, beta_2):

  # Initial model DataFrame
  df = pd.DataFrame(Qp)

  # Iterate through peak discharge values
  for index, row in df.iterrows():

    # Update main channel variables
    df.loc[index, "Q_bf"] = Q_bf # Set bankfull discharge
    df.loc[index, "Qt_bf"] = Qt_bf # Set bankfull transport capacity
    df.loc[index, "B_bf"] = B_bf # Set bankfull width
    df.loc[index, "H_bf"] = H_bf # Set bankfull depth
    df.loc[index, "Slope"] = Slope # Set channel slope
    # Set channel hydraulic roughness
    df.loc[index, "Cz"] = alpha_R * df.loc[index, "Slope"]**-n_R

    # Calculate in-channel discharge
    df.loc[index, "Q_ch"] = Q_ch(df.loc[index, "Q_bf"], df.loc[index, "Q_p"],
                            df.loc[index, "B_bf"], df.loc[index, "H_bf"],
                            df.loc[index, "Slope"], df.loc[index, "Cz"], Cz_f, theta)

    # Calculate in-channel flow depth
    df.loc[index, "H_ch"] = (((1/df.loc[index, "Cz"])**2 * df.loc[index, "Q_ch"]**2) /
                            (df.loc[index, "B_bf"]**2 * g *
                            df.loc[index, "Slope"]))**(1.0/3.0)

    # Check if channel flow depth is greater than bankfull depth
```

```python
if df.loc[index, "H_ch"] > df.loc[index, "H_bf"]:
    df.loc[index, "H_f"] = df.loc[index, "H_ch"] - df.loc[index, "H_bf"]
    df.loc[index, "B_f"] = (2 * (np.tan(np.radians(90 - theta)) * df.loc[index, "H_f"]))
    df.loc[index, "Inundated"] = 1
else:
    df.loc[index, "H_f"] = np.nan
    df.loc[index, "B_f"] = np.nan
    df.loc[index, "Inundated"] = np.nan


# Calculate sediment supply depending on selected scenarios
if SS == "1": # Sediment Supply Scenario 1
    df.loc[index, "Q_s"] = Q_s(df.loc[index, "Q_p"])
elif SS == "2": # Sediment Supply Scenario 2
    df.loc[index, "Q_s"] = Qt_bf_init
elif SS == "3": # Sediment Supply Scenario 3
    Qs = Q_s(df.loc[index, "Q_p"])
    if Qs > Qt_bf_init:
        df.loc[index, "Q_s"] = Qt_bf_init
    else:
        df.loc[index, "Q_s"] = Qs
elif SS == "4": # Sediment Supply Scenario 4
    df.loc[index, "Q_s"] = Q_s(df.loc[index, "Q_p"]) * 0.5
elif SS == "5": # Sediment Supply Scenario 5
    df.loc[index, "Q_s"] = Q_s(df.loc[index, "Q_p"]) * 2


# Calculate channel geometry predictions

# Width prediction
df.loc[index, "B_pred"] = B_bf_calc(df.loc[index, "Q_p"], df.loc[index, "Q_s"])
# Depth prediction
df.loc[index, "H_pred"] = H_bf_calc(df.loc[index, "Q_p"], df.loc[index, "Q_s"])
# Slope prediction
df.loc[index, "Slope_pred"] = Slope_calc(df.loc[index, "Q_p"],
                                df.loc[index, "Q_s"])


# Modify predictions based on chosen adjustment method
if Method == "A":
    B_bf = df.loc[index, "B_bf"] + (beta_1 * (df.loc[index, "B_pred"] -
            df.loc[index, "B_bf"]))
    H_bf = df.loc[index, "H_bf"] + (beta_1 * (df.loc[index, "H_pred"] -
            df.loc[index, "H_bf"]))
    Slope = df.loc[index, "Slope"] + (beta_1 * (df.loc[index, "Slope_pred"] -
            df.loc[index, "Slope"]))
elif Method == "B":
```

```
            if df.loc[index, "B_pred"] > df.loc[index, "B_bf"]:
                B_bf = df.loc[index, "B_bf"] + (beta_2 * (df.loc[index, "B_pred"] -
                        df.loc[index, "B_bf"]))
            else:
                B_bf = df.loc[index, "B_bf"] + (beta_1 * (df.loc[index, "B_pred"] -
                        df.loc[index, "B_bf"]))

            H_bf = df.loc[index, "H_bf"] + (beta_1 * (df.loc[index, "H_pred"] -
                    df.loc[index, "H_bf"]))
            Slope = df.loc[index, "Slope"] + (beta_1 * (df.loc[index, "Slope_pred"] -
                    df.loc[index, "Slope"]))
        elif Method == "C":
            if df.loc[index, "B_pred"] > df.loc[index, "B_bf"]:
                B_bf = df.loc[index, "B_bf"] + (beta_2 * (df.loc[index, "B_pred"] -
                        df.loc[index, "B_bf"]))
            else:
                B_bf = df.loc[index, "B_bf"] + (beta_1 * (df.loc[index, "B_pred"] -
                        df.loc[index, "B_bf"]))

            if df.loc[index, "H_pred"] > df.loc[index, "H_bf"]:
                H_bf = df.loc[index, "H_bf"] + (beta_2 * (df.loc[index, "H_pred"] -
                        df.loc[index, "H_bf"]))
            else:
                H_bf = df.loc[index, "H_bf"] + (beta_1 * (df.loc[index, "H_pred"] -
                        df.loc[index, "H_bf"]))

            if df.loc[index, "Slope_pred"] > df.loc[index, "Slope"]:
                Slope = df.loc[index, "Slope"] + (beta_2 * (df.loc[index, "Slope_pred"] -
                        df.loc[index, "Slope"]))
            else:
                Slope = df.loc[index, "Slope"] + (beta_1 * (df.loc[index, "Slope_pred"] -
                        df.loc[index, "Slope"]))

        # Calculate new bankfull discharge and transport capacity
        Q_bf, Qt_bf = New_capacity(B_bf, H_bf, Slope)

        # Calculate running average statistics for flood frequency and inundation width
        df.loc[index,"FF_100yr"] = FF(df["Inundated"], 100, index)
        df.loc[index,"Bf_100yr"] = Bf_Stats(df["B_f"], 100, index)

    return df # Return model dataframe


# Function to calculate discharge within the channel
def Q_ch(Q_bf, Q_p, B_bf, H_bf, slope, Cz_channel, Cz_floodplain, theta):
```

```
deltas = [100, 10, 1, 0.1, 0.01, 0.001, 0.0001, 0.00001, 0.000001]
# Check if peak discharge is greater than bankfull discharge
if Q_p > Q_bf:
    Q_e = Q_p - Q_bf
    Q_f = 0.0
    H_e = 0.0
    H_f = 0.0

    # Paritition discharge between the channel and floodplain until an equal water
    # surface elevation is reached
    for delta in deltas:
        Q_e, Q_f, H_e, H_f = iterate(Q_e, Q_f, B_bf, H_bf, H_e, H_f, delta, slope, theta,
                                    Cz_channel, Cz_floodplain)
    return Q_e + Q_bf
else:
    return Q_p


# Iterative function used within Q_ch()
@numba.jit(nopython=True)
def iterate(Q_e, Q_f, B_bf, H_bf, H_e, H_f, delta, slope, theta, Cz_channel,
           Cz_floodplain):
    while True:
        Q_e -= delta
        Q_f += delta
        H_e = (((1.0/Cz_channel)**2.0 * Q_e**2.0)/(B_bf**2.0 * g * slope))**(1.0/3.0)
        H_f = (((1.0/Cz_floodplain)**2.0 * (Q_f/2.0)**2.0)/(np.tan(np.radians(90 –
                    theta))**2.0 * g * Slope_floodplain))**(1.0/3.0)
        if Q_e <= 0.0:
            Q_e += delta
            Q_f -= delta
            return Q_e, Q_f, H_e, H_f
        if H_e <= H_f:
            Q_e += delta
            Q_f -= delta
            return Q_e, Q_f, H_e, H_f


# Function to calculate sediment supply in the supply reach at a given discharge
def Q_s(Q_p):
    Qch = Q_ch(Q_bf_init, Q_p, B_bf_supply, H_bf_supply, Slope_supply, Cz_supply,
            Cz_f, theta)
    Hch = (((1/Cz_supply)**2 * Qch**2) / (B_bf_supply**2 * g *
            Slope_supply))**(1.0/3.0)
    tao_star = (Hch * Slope_supply) / (R * D)
    qt = alpha_EH * (Cz_supply)**2 * np.sqrt(R*g*D) * D * tao_star**(5.0/2.0)
```

```python
    Qt = qt * B_bf_supply
    return Qt


# Function to calculate bankfull width using the Li et al. hydraulic geometry relations
def B_bf_calc(Q_bf, Qt_bf):
    return ((D_star**2.5) / (alpha_EH * np.sqrt(R) * alpha_R**2 * beta**2.5 *
            ((R*D_star) / (alpha_EH*alpha_R*beta))**((2.5 * m - 2 * n_R)/(1 + m - n_R)))
             * ((Qt_bf / Q_bf)**(-(2.5 * m - 2 * n_R)/(1 + m - n_R))) * (Qt_bf /
            (np.sqrt(g*D) * D**2)))*D


# Function to calculate bankfull depth using the Li et al. hydraulic geometry relations
def H_bf_calc(Q_bf, Qt_bf):
    return ((alpha_EH * alpha_R * beta**2) / (D_star**2)) * (((R * D_star)/(alpha_EH *
            alpha_R * beta))**((2*m - n_R)/(1+m-n_R))) * ((Qt_bf/Q_bf)**((2*m -
            n_R)/(1+m-n_R))) * (Q_bf/Qt_bf) * D


# Function to calculate slope using the Li et al. hydraulic geometry relations
def Slope_calc(Q_bf, Qt_bf):
    return (((R * D_star)/(alpha_EH * alpha_R * beta))**((1.0)/(1+m-n_R))) *
            ((Qt_bf/Q_bf) **((1.0)/(1+m-n_R)))


# Function to calculate new bankfull discharge and bankfull transport capacity as a
#function of width, depth, and slope
def New_capacity(B_bf, H_bf, S):
    Cz = alpha_R * S**-n_R
    U_bf = Cz * np.sqrt(g * H_bf * S)
    Q_bf = B_bf * H_bf * U_bf
    tao_star_bf = (H_bf * S) / (R * D)
    qt = alpha_EH * Cz**2 * np.sqrt(R*g*D) * D * tao_star_bf**(5.0/2.0)
    Qt_bf = qt * B_bf
    return Q_bf, Qt_bf


# Function to calculate moving window average of flood frequencies
def FF(Inundated, x, index):
    if index < x:
        return np.nan
    FF_x = Inundated[index-x:index].sum(skipna=True) / x
    return FF_x


# Function to calculate moving window average of floodplain inundation widths
def Bf_Stats(B_f, x, index):
    if index < x:
        return np.nan
    Bf_mean = B_f[index-x:index].mean(skipna=True)
```

```
    return Bf_mean
```

Section 3: Initialize and run model

 # Create Supply Channel
B_bf_supply = B_bf_calc(Q_bf_init, Qt_bf_init) *# Define width of supply reach*
H_bf_supply = H_bf_calc(Q_bf_init, Qt_bf_init) *# Define depth of supply reach*
Slope_supply = Slope_calc(Q_bf_init, Qt_bf_init) *# Define slope of supply reach*
 # Define hydraulic roughness of supply reach
Cz_supply = alpha_R * Slope_supply**-n_R

 # Calculate Initial Channel Geometry using spin_up
Qp_spin_up = {"Q_p": Qp["Q_p"][:499]}
spin_up = Model(Qp_spin_up, Q_bf_init, Qt_bf_init, B_bf_supply, H_bf_supply,
Slope_supply, 0.05, 0.05)
Q_bf = float(spin_up.ix[498:498,"Q_bf"])
Qt_bf = float(spin_up.ix[498:498,"Qt_bf"])
B_bf = float(spin_up.ix[498:498,"B_bf"])
H_bf = float(spin_up.ix[498:498,"H_bf"])
Slope = float(spin_up.ix[498:498,"Slope"])

 # Run Model
df = Model(Qp, Q_bf, Qt_bf, B_bf, H_bf, Slope, beta_1, beta_2)

Section 4: Extract summary statistics from model outputs

sr1 = df[:(n / 2)].copy()
sr2 = df[(n / 2):].copy()

 # Years 1 to 100
FFT1 = df["Inundated"][:100].sum(skipna=True) / 100 *# Flood frequency*
I_meanT1 = df.B_f[:100].mean(skipna=True) *# Mean inundation width*
I_stdT1 = df.B_f[:100].std(skipna=True) *# Standard deviation inundation width*
srT1 = sr1[:100].copy()
srT1.loc[:,"FFT1"] = FFT1
srT1.loc[:,"I_meanT1"] = I_meanT1

```
# Years 100 to 500
FF1 = df["Inundated"][100:500].sum(skipna=True) / 400 # Flood frequency
I_mean1 = df.B_f[100:500].mean(skipna=True) # Mean inundation width
I_std1 = df.B_f[100:500].std(skipna=True) # Standard deviation inundation width
sr1_a = sr1[100:500]
sr1_a.loc[:,"FF1"] = FF1
sr1_a.loc[:,"I_mean1"] = I_mean1

# Years 500 to 600
FFT2 = df["Inundated"][500:600].sum(skipna=True) / 100 # Flood frequency
I_meanT2 = df.B_f[500:600].mean(skipna=True) # Mean inundation width
I_stdT2 = df.B_f[500:600].std(skipna=True) # Standard deviation inundation width
srT2 = sr2[:100].copy()
srT2.loc[:,"FFT2"] = FFT2
srT2.loc[:,"I_meanT2"] = I_meanT2

# Years 600 to 1000
FF2 = df["Inundated"][600:].sum(skipna=True) / 400 # Flood frequency
I_mean2 = df.B_f[600:].mean(skipna=True) # Mean inundation width
I_std2 = df.B_f[600:].std(skipna=True) # Standard deviation inundation width
sr2_a = sr2[100:500]
sr2_a.loc[:,"FF2"] = FF2
sr2_a.loc[:,"I_mean2"] = I_mean2




### Section 5: Plot model outputs

# Plot Bankfull Area
fig, host = plt.subplots(figsize=(12, 4))
par = host.twinx()
host.scatter(df.index, df.Q_p, 1, "k")
par.plot(sr1.index, sr1.B_bf *sr1.H_bf , "r", linewidth=2)
par.plot(sr2.index, sr2.B_bf * sr2.H_bf , "b", linewidth=2)
host.grid(True)
host.set_xlim((0, n))
host.set_ylim(1, 10000)
host.set_yscale("log")
par.set_ylim((200, 550))
host.set_xlabel('Modeled Time (Years)', fontsize=18)
host.set_ylabel('Peak Discharge (cms)', fontsize=16)
```

```
label = par.set_ylabel("Bankfull Area (m)", fontsize=16)
label.set_color("blue")
plt.gcf().subplots_adjust(bottom=0.15)
plt.yticks(color="b")
plt.show()

# Plot Bankfull Width
fig, host = plt.subplots(figsize=(12, 4))
par = host.twinx()
host.scatter(df.index, df.Q_p, 1, "k")
par.plot(sr1.index, sr1.B_bf, "r", linewidth=2)
par.plot(sr2.index, sr2.B_bf, "b", linewidth=2)
host.grid(True)
host.set_xlim((0, n))
host.set_ylim(1, 10000)
host.set_yscale("log")
par.set_ylim((40, 140))
host.set_xlabel('Modeled Time (Years)', fontsize=18)
host.set_ylabel('Peak Discharge (cms)', fontsize=16)
label = par.set_ylabel("Bankfull Width (m)", fontsize=16)
label.set_color("blue")
plt.gcf().subplots_adjust(bottom=0.15)
plt.yticks(color="b")
plt.show()

# Plot Bankfull Depth
fig, host = plt.subplots(figsize=(12, 4))
par = host.twinx()
host.scatter(df.index, df.Q_p, 1, "k")
par.plot(sr1.index, sr1.H_bf, "r", linewidth=2)
par.plot(sr2.index, sr2.H_bf, "b", linewidth=2)
host.grid(True)
host.set_xlim((0, n))
host.set_ylim(1, 10000)
host.set_yscale("log")
par.set_ylim((4, 5))
host.set_xlabel('Modeled Time (Years)', fontsize=18)
host.set_ylabel('Peak Discharge (cms)', fontsize=16)
label = par.set_ylabel("Bankfull Depth (m)", fontsize=16)
label.set_color("blue")
plt.gcf().subplots_adjust(bottom=0.15)
plt.yticks(color="b")
plt.show()
```

```
# Plot Slope
fig, host = plt.subplots(figsize=(12, 4))
par = host.twinx()
host.scatter(df.index, df.Q_p, 1, "k")
par.plot(sr1.index, sr1.Slope, "r", linewidth=2)
par.plot(sr2.index, sr2.Slope, "b", linewidth=2)
host.grid(True)
host.set_xlim((0, n))
host.set_ylim(1, 10000)
host.set_yscale("log")
par.set_ylim((0.0001, 0.0004))
host.set_xlabel('Modeled Time (Years)', fontsize=18)
host.set_ylabel('Peak Discharge (cms)', fontsize=16)
label = par.set_ylabel("Channel Slope", fontsize=16)
label.set_color("blue")
plt.gcf().subplots_adjust(bottom=0.15)
plt.yticks(color="b")
plt.show()

# Plot Inundation Widths
fig, host = plt.subplots(figsize=(12, 4))
par = host.twinx()
host.scatter(df.index, df.Q_p, 1, "k")
par.scatter(sr1.index, sr1.B_f, 60, "r")
par.scatter(sr2.index, sr2.B_f, 60, "b")
host.grid(True)
host.set_xlim((0, n))
host.set_ylim(1, 10000)
host.set_yscale("log")
par.set_ylim((0, 3000))
host.set_xlabel('Modeled Time (Years)', fontsize=18)
host.set_ylabel('Peak Discharge (cms)', fontsize=16)
label = par.set_ylabel("Inundation Width (m)", fontsize=16)
label.set_color("blue")
plt.gcf().subplots_adjust(bottom=0.15)
plt.yticks(color="b")
plt.show()

# Plot Flood Frequency Window
fig, host = plt.subplots(figsize=(12, 4))
par = host.twinx()
host.scatter(df.index, df.Q_p, 1, "k")
par.plot(sr1_a.index, sr1_a.FF_100yr, "r", linewidth=2)
par.plot(sr1_a.index, sr1_a.FF1, "r--", linewidth=2)
```

```
par.plot(srT1.index, srT1.FFT1, "y--", linewidth=2)
par.plot(sr2_a.index, sr2_a.FF_100yr, "b", linewidth=2)
par.plot(sr2_a.index, sr2_a.FF2, "b--", linewidth=2)
par.plot(srT2.index, srT2.FFT2, "g--", linewidth=2)
host.grid(True)
host.set_xlim((0, n))
host.set_ylim(1, 10000)
host.set_yscale("log")
par.set_ylim((0.0, 1.0))
host.set_xlabel('Modeled Time (Years)', fontsize=18)
host.set_ylabel('Peak Discharge (cms)', fontsize=16)
label = par.set_ylabel("Flood Frequency", fontsize=16)
label.set_color("blue")
plt.gcf().subplots_adjust(bottom=0.15)
plt.yticks(color="b")
plt.show()

# Plot Mean Inundation Width Window
fig, host = plt.subplots(figsize=(12, 4))
par = host.twinx()
host.scatter(df.index, df.Q_p, 1, "k")
par.plot(sr1_a.index, sr1_a.Bf_100yr, "r", linewidth=2)
par.plot(sr1_a.index, sr1_a.I_mean1, "r--", linewidth=2)
par.plot(srT1.index, srT1.I_meanT1, "y--", linewidth=2)
par.plot(sr2_a.index, sr2_a.Bf_100yr, "b", linewidth=2)
par.plot(sr2_a.index, sr2_a.I_mean2, "b--", linewidth=2)
par.plot(srT2.index, srT2.I_meanT2, "g--", linewidth=2)
host.grid(True)
host.set_xlim((0, n))
host.set_ylim(1, 10000)
host.set_yscale("log")
par.set_ylim((0, 800))
host.set_xlabel('Modeled Time (Years)', fontsize=18)
host.set_ylabel('Peak Discharge (cms)', fontsize=16)
label = par.set_ylabel("Mean Inundation Width", fontsize=16)
label.set_color("blue")
plt.gcf().subplots_adjust(bottom=0.15)
plt.yticks(color="b")
plt.show()
```